Cold Collision Dynamics of NH Radicals

Liesbeth M. C. Janssen

ISBN/EAN 978-94-6108283-1

Cold Collision Dynamics of NH Radicals
L. M. C. Janssen
PhD Thesis Radboud University Nijmegen
Cover design by L. M. C. Janssen and J. Spruit (www.ornaat.nl)
Background image: Boomerang nebula / Credit: NASA, ESA, R. Sahai and J. Trauger (Jet Propulsion Laboratory) and the WFPC2 Science Team
Printed by Gildeprint drukkerijen, Enschede

The work described in this thesis has been financially supported by the Council for Chemical Sciences of the Netherlands Organization for Scientific Research (CW-NWO).

Cold Collision Dynamics of NH Radicals

Een wetenschappelijke proeve op het gebied van de
Natuurwetenschappen, Wiskunde en Informatica

Proefschrift

ter verkrijging van de graad van doctor
aan de Radboud Universiteit Nijmegen
op gezag van de rector magnificus prof. mr. S.C.J.J. Kortmann,
volgens besluit van het College van Decanen
in het openbaar te verdedigen op woensdag 25 april 2012
om 15:30 uur precies

door

Liesbeth Maria Catharina Janssen

geboren op 28 december 1983
te Meijel

Promotor:	Prof. dr. ir. A. van der Avoird
Copromotor:	Dr. ir. G. C. Groenenboom
Manuscriptcommissie:	Prof. dr. D. H. Parker (voorzitter) Prof. dr. J. M. Hutson (Durham University) Prof. dr. R. Moszyński (Warsaw University)

Contents

1 Introduction **5**
1.1 Absolute zero . . . 5
1.2 “The producing of cold” . . . 8
1.3 The NH + NH system . . . 10
1.4 Theoretical methods . . . 13
1.4.1 Electronic structure theory . . . 13
1.4.2 Scattering theory . . . 16

2 Potential energy surfaces **23**
2.1 Introduction . . . 23
2.2 Electronic structure calculations . . . 24
2.2.1 RCCSD(T) potential energy surface . . . 24
2.2.2 Perturbation theory calculations . . . 27
2.2.3 CASPTn calculations . . . 28
2.3 Analytical representation . . . 28
2.3.1 Long-range potential . . . 29
2.3.2 Short-range $S = 2$ potential . . . 30
2.3.3 Short-range $S = 0, 1$ potentials . . . 32
2.4 Results and discussion . . . 32
2.4.1 Long-range potential . . . 33
2.4.2 Short-range potentials . . . 36
2.5 Conclusions . . . 38
Appendix . . . 38

3 Scattering in field-free space **41**
3.1 Introduction . . . 41
3.2 Theory . . . 42
3.2.1 Hamiltonian and channel basis functions . . . 42

3.2.2 S-matrices and cross sections . . . 47
3.2.3 Computational details . . . 48
3.3 Results and discussion . . . 49
3.3.1 Cross sections . . . 49
3.3.2 Contributions from singlet and triplet states . . . 52
3.3.3 Sensitivity to potential and basis-set size . . . 53
3.4 Conclusions . . . 57

4 Scattering in magnetic fields 59
4.1 Introduction . . . 59
4.2 Calculations . . . 60
4.2.1 Theory . . . 60
4.2.2 Computational details . . . 64
4.3 Results and discussion . . . 64
4.3.1 Adiabatic potential energy curves . . . 64
4.3.2 Cross sections . . . 65
4.3.3 Dependence on potential and basis-set size . . . 70
4.4 Conclusions . . . 72

5 Magnetic dipole-dipole coupling 73
5.1 Introduction . . . 73
5.2 Theory . . . 75
5.2.1 Coupled-channels calculations . . . 75
5.2.2 Born approximation . . . 77
5.2.3 Analytical distorted-wave Born approximation . . . 80
5.3 Results and discussion . . . 82
5.3.1 Numerical results . . . 82
5.3.2 Comparison with BA and DWBA . . . 85
5.4 Conclusions . . . 90

6 Quantum reactive scattering 93
6.1 Introduction . . . 93
6.2 Theory . . . 95
6.2.1 Propagation . . . 96
6.2.2 Boundary conditions and S-matrix . . . 100
6.2.3 Computational details . . . 103
6.3 Results and discussion . . . 104
6.3.1 Energy dependence . . . 104
6.3.2 Magnetic-field dependence . . . 105
6.3.3 Scattering in the universal limit . . . 107
6.3.4 Sensitivity to potentials and basis-set size . . . 108
6.4 Concluding remarks . . . 111

Bibliography **113**

Summary **119**

Samenvatting **123**

Dankwoord **127**

Publications **129**

Curriculum Vitae **131**

Chapter 1

Introduction

> *"The producing of cold is a thing very worthy the inquisition, both for the use and the disclosure of causes. For heat and cold are Nature's two hands whereby see chiefly worketh, and heat we have in readiness in respect of the fire, but for cold we must stay till it commeth, or seek it in deep caves or high mountains. And when all is done, we cannot obtain it in any great degree, for furnaces of fire are far hotter than a summer's sun, but vaults or hills are not much colder than a winter's frost."*
>
> Francis Bacon, *Sylva Sylvarum* (1627)

1.1 Absolute zero

The concept of absolute zero, the lowest temperature theoretically possible, has intrigued scientists ever since it was first introduced some 300 years ago. In 1703, the French physicist Guillaume Amontons inferred from his work on air thermometers that there must be a finite minimal temperature at which the pressure of air, regardless of the volume, vanishes. This "degree of cold", he wrote, must be far greater than the "very cold" of freezing water, about -240 degrees on the modern Celsius scale (see Fig. 1.1) [1]. Amontons' result was, however, far from generally accepted. By the start of the 19th century, estimates for a possible zero of temperature ranged from -260 to -6000 °C depending on which substance was used in the experiments [2]. The matter was finally resolved in 1848 when William Thomson, a.k.a. Lord Kelvin, proposed a new temperature scale in which "a unit of heat descending from a body A at temperature T to a body B at temperature $(T-1)$ gives out the same mechanical effect [work], whatever be the number T." This scale, Kelvin argued, is independent of the properties of any particular kind of matter, and is therefore absolute [3]. Kelvin placed the zero of temperature at the point where no further heat could be transferred, a value

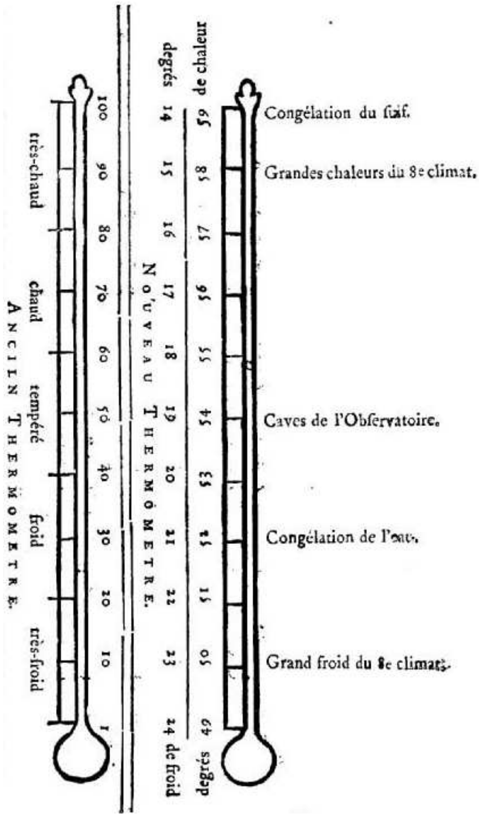

Figure 1.1: Scale of Amontons' air thermometer ("Nouveau Thermometre"), in which the temperature is indicated by the height at which a column of mercury is sustained by air. Amontons argued that the "extreme cold" of his thermometer would be that temperature at which the pressure of air reduces to zero. On the scale he used, the boiling point of water was marked at 73 and the melting point of ice at 51.5, placing the zero at about −240 °C. The figure is taken from Ref. [1].

he calculated to be −273 °C. In 1954, the Kelvin scale obtained its modern definition with absolute zero fixed at −273.15 °C or 0 K [4].

The 19th century also marked the beginning of the experimental quest for absolute zero. Throughout Europe, scientists began developing new methods to cool matter to lower and lower temperatures, ultimately resulting in the liquefaction of all known gases. In 1823, Michael Faraday liquefied chlorine at 239 K by cooling chlorine gas under high pressure [5]. Oxygen required 90 K, as demonstrated independently by Raoul Pictet [6] and Louis-Paul Cailletet [7] in 1877. Nitrogen turned liquid at 77 K [8]. In 1898, the Scottish physicist James Dewar succeeded at liquefying hydrogen at a temperature of 20 K [9]. The last remaining gas, helium, with a boiling point of 4 K, was liquefied in 1908 by Dutch physicist Heike Kamerlingh Onnes [10], a result that would win him the 1913 Nobel Prize in Physics.

The liquefaction of helium proved a true milestone in low-temperature physics. Not only did it allow Kamerlingh Onnes to discover the phenomenon of superconductivity [11], it also led to the discovery of superfluidity three decades later. In 1937, Pyotr Kapitsa, John Allen, and Don Misener found that liquid helium, when cooled to 2.2 K, forms a superfluid state that is characterized by zero viscosity and infinite thermal conductivity [12, 13]. The theoretical explanation for this new state of matter was quickly given by Fritz London, who, in 1938, made the connection between superfluidity and the theory of Bose-Einstein condensates (BECs) [14].

Bose-Einstein condensation, a phenomenon predicted by Satyendra Nath Bose and Albert Einstein in 1925 [15, 16], refers to a certain type of phase transition in systems composed of integer-spin particles. It occurs when an ensemble of identical bosons, confined in an external trapping potential, is cooled to cryogenic temperatures such that the thermal de Broglie wavelength of the particles is much larger than the average interparticle spacing. In this so-called quantum-degenerate regime, a significant fraction of the particles spontaneously ‘condenses’ into the ground state of the trap, collectively forming a macroscopic BEC wave function (see Fig. 1.2). It is this effect that is responsible for the frictionless flow of helium: superfluid helium is partially Bose-Einstein condensed. The formation of a ‘pure’ BEC, however, requires a dilute gas rather than a liquid, and it was not until 1995 that the first gaseous BEC was realized experimentally. Carl Wieman and Eric Cornell succeeded at producing a BEC in a vapour of magnetically trapped rubidium atoms, cooled down to a temperature of 170 nK (Fig. 1.2) [17]. Four months later, Wolfgang Ketterle reported the creation of a BEC of ultracold sodium atoms [18]. In 2001, just six years after their experimental success, Cornell, Wieman, and Ketterle shared the Nobel Prize in Physics.

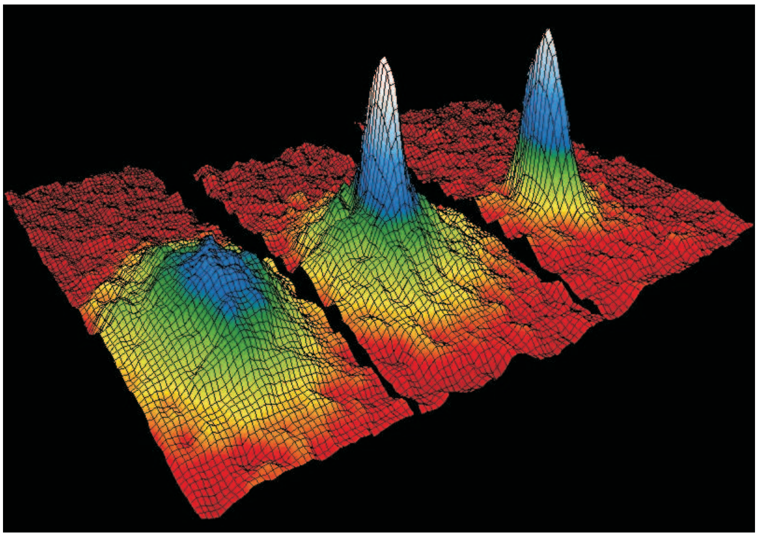

Figure 1.2: BEC formation in a gas of Rb atoms [17]. The three images show (left) the velocity distribution just before the onset of Bose-Einstein condensation, (center) just after the appearance of the condensate, and (right) after further evaporation to leave behind a nearly pure BEC. The figure is taken from the NIST image gallery (http://bec.nist.gov/gallery.html).

The pioneering work in BEC formation prompted a major revolution in physics. Ultracold atoms opened up the possibility to systematically control and manipulate interparticle interactions, allowing novel studies of quantum many-body effects [19]. A key milestone was reached in 2003, when Deborah Jin [20] and Rudolph Grimm [21] independently reported the creation of a new state of matter known as a fermionic condensate, the half-integer-spin equivalent of a BEC. It is now well established that BECs and ultracold fermionic gases are ideal model systems for the study of complex condensed-matter phenomena such as superconductivity [22], Anderson localization [23], and the superfluid-Mott-insulator transition [24]. Moreover, ultracold gases have provided the first experimental evidence for so-called Efimov states [25], elusive few-body quantum states that were first predicted in 1970. Finally, the production and trapping of ultracold atoms has found important applications in high-precision spectroscopy [26], quantum metrology [27, 28], and quantum information processing [29].

At present, there is great interest in the production of ultracold *molecules*. In particular heteronuclear polar molecules, which possess a permanent electric dipole moment, are expected to lead to novel quantum phenomena. The effect of long-range, tunable, anisotropic electric dipole interactions – still mostly unexplored in ultracold gases – may prove very useful in quantum simulations of condensed-matter systems and in quantum computers [30, 31, 32]. Furthermore, the relatively complex internal structure of molecules can facilitate high-precision measurements of, e.g., the electric dipole moment of the electron and the possible time variation of fundamental constants [33, 34, 35]. Another major application of cold molecules lies in the field of chemistry. At temperatures near or below 1 K, molecular collision processes can be strongly influenced by weak electromagnetic perturbations, allowing external field control of chemical reactions [36]. Such cold chemistry may also address fundamental questions in quantum reaction dynamics [37]. To conclude, cold molecular gases offer a realm of possibilities in science, and it is one of today's greatest challenges to produce them at sufficiently high densities and sufficiently low temperatures.

1.2 "The producing of cold"

The cooling of atomic and molecular gases to near-absolute zero generally proceeds in two stages: first-stage cooling brings the system in the "cold" ($T < 1$ K) or "ultracold" ($T < 1$ mK) regime, while second-stage cooling provides full quantum degeneracy. One of the most successful first-stage-cooling methods is Doppler laser cooling, a technique in which atoms are slowed down through their interaction with laser light. The method is usually combined with a magnetic trapping field to confine the particles in space, resulting in a so-called magneto-optical trap. The basic idea is to reduce an atom's kinetic energy by exposing it to small but repetitive photon-momentum kicks. At the same time, the magnetic field drives the particles to the center of the trap, resulting in an increase of phase-space density. This cooling method, first demonstrated in 1987 [38], proved to be crucial in the experimental realization of the first Bose-Einstein condensates, and it was celebrated with the 1997 Nobel Prize in Physics.

While laser cooling is very successful for certain types of atoms, in particular for alkali metals, it is – with the exception of SrF [39] – highly inefficient for molecules. Laser cooling requires a system with a relatively simple level structure and a (nearly) closed absorption-emission cycle. This makes it unsuitable for species with many rovibrational degrees of freedom. Among the various alternative first-stage approaches to produce cold molecular samples we may distinguish two general classes: direct- and indirect-cooling methods. Indirect methods employ a two-step mechanism to assemble cold molecules from atoms that are already close to quantum degeneracy. The first step involves the pairing of two ultracold atoms into a weakly-bound molecular state, either by means of a laser (photoassociation) [40] or a magnetic field (magneto- or Feshbach association) [41]. Next, the weakly bound molecules are transferred to the rovibrational ground state using a series of laser pulses [42, 43]. These methods, which can achieve temperatures as low as 300 nK, have already led to the first experimental demonstration of electric dipolar interactions in ultracold molecular gases [36] and quantum control of cold chemical reactions [44, 45]. The applicability of indirect-cooling techniques is, however, limited to diatomic molecules whose constituent atoms can be efficiently laser-cooled into the ultracold regime. Hence, in practice, photo- and magneto-association are applicable only to (closed-shell) bi-alkali species.

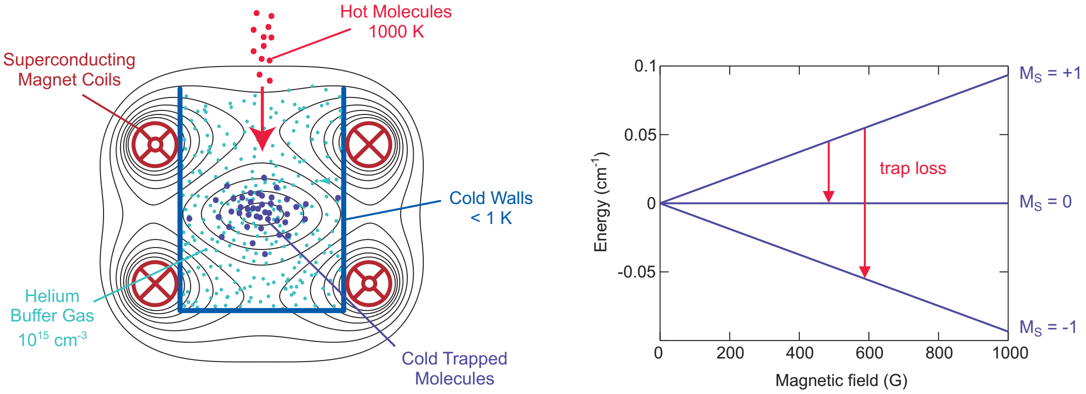

Figure 1.3: Left: principle of buffer-gas cooling. Paramagnetic molecules are cooled through collisions with a cryogenic helium buffer gas and trapped in an external magnetic field. The minimum of the field is at the center of the trap. Right: Zeeman diagram for the triplet ground state of NH. Magnetically trappable triplet-spin molecules are in the low-field-seeking $M_S = 1$ state, with M_S denoting the space-fixed spin projection quantum number. States with $M_S = 0$ or -1 cannot be confined in the trap.

Direct-cooling methods, on the other hand, employ fairly general schemes to cool pre-existing molecules from high to low temperatures, making them suitable for a diverse class of molecules. Such methods may be used for, e.g., high-precision measurements in Π-state molecules [46] or cold controlled chemistry of polyatomic species [37], allowing the full range of cold-molecule applications to be explored. Perhaps the most general method is buffer-gas cooling in a magnetic trap, a technique in which paramagnetic species are cooled through thermalizing collisions with a cryogenic helium buffer gas (see Fig. 1.3) [47]. Application of this method, followed by second-stage cooling (see below), has already enabled BEC formation in a gas of metastable helium – the first BEC of a non-laser-cooled atomic species [48]. Other direct-cooling techniques include Zeeman [49] and Stark [50] deceleration, in which inhomogeneous magnetic and electric fields are used to slow down molecules, kinematic cooling [51], which relies on collisions between crossed molecular beams, and velocity filtering [52]. These methods may be combined with, e.g., a magnetic or electrostatic trap to obtain spatial confinement.

The above-mentioned first-stage-cooling methods are, however, insufficient to reach full quantum degeneracy. BEC formation of trapped molecules can, in principle, be accomplished by a second-stage cooling mechanism known as evaporative cooling, a method that relies on the elastic scattering of particles [53]. Evaporative cooling proceeds by slowly reducing the trap depth, allowing the most energetic particles to leave the sample. Subsequent rethermalization, which is achieved through elastic collisions, yields a new thermal distribution that is characterized by a slightly lower temperature. When repeated many times, this process significantly increases the density of ultracold species, ultimately leading to full quantum degeneracy. An alternative second-stage-cooling approach is sympathetic cooling, a technique in which particles are cooled through elastic (thermalizing) collisions with another quantum-degenerate gas. The success of both of these methods is, however, critically dependent on the ratio between elastic and non-elastic collision rates. Since inelastic and reactive collisions can lead to trap loss and heating of the gas (Fig. 1.3), the total non-elastic cross section should be much smaller than the elastic one, typically by two orders of magnitude [54]. While both procedures have proven successful for atomic gases, they are yet to be demonstrated experimentally for (polar) molecules.

1.3 The NH + NH system

One of the most attractive candidates for cold-molecule experiments is the imidogen radical (NH), a polar, paramagnetic, and chemically reactive species. NH has two stable isotopologues, fermionic ^{14}NH and bosonic ^{15}NH, both of which are of interest for fundamental studies in the quantum-degenerate regime. Furthermore, chemical reactions between cold NH molecules can yield as many as 8 different reaction products (see Fig. 1.4), making it a versatile system for (ultra)cold chemistry applications.

Up to the present, two first-stage-cooling methods have been employed to produce cold NH radicals. Ground-state NH($X\,^3\Sigma^-$) has been cooled and trapped in a magnetic field by means of buffer-gas cooling (see Fig. 1.3), producing a temperature of about 0.5 K [57, 58, 59, 60]. It was recently demonstrated that buffer-gas-cooled NH can also be co-trapped with atomic nitrogen, opening up the possibility to sympathetically cool NH with ultracold N atoms [61]. Moreover, metastable NH($a\,^1\Delta$), which exhibits a linear Stark shift, has been successfully Stark-decelerated and confined in an electrostatic trap [62]. The decelerated molecules may also be converted to the ground state

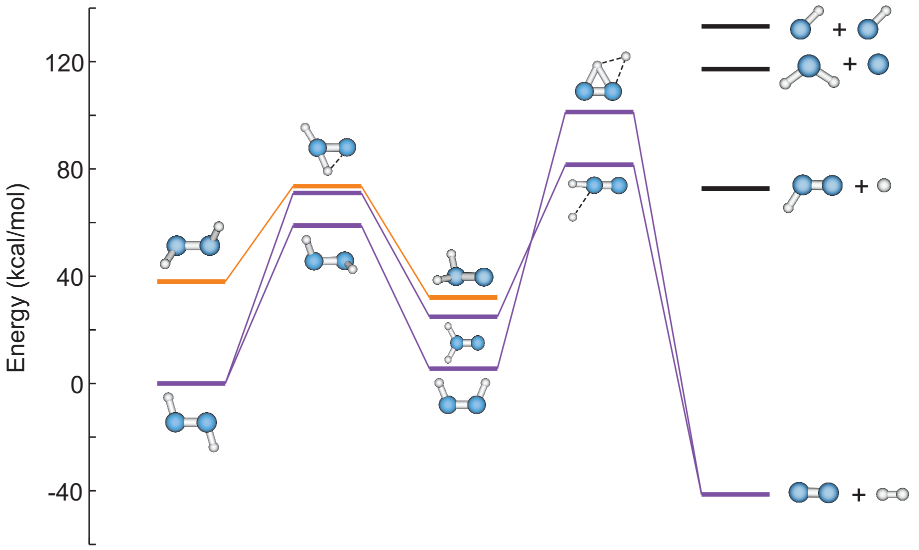

Figure 1.4: Energy diagram of isomers and transition structures of NHNH. Purple lines correspond to singlet spin states and orange lines to triplet states. The configurations NH($^3\Sigma^-$) + NH($^3\Sigma^-$), NH_2($^2A''$) + N(^4S), and HN_2($^2A'$) + H(^2S) exist in multiple spin states. Energies are given in kcal/mol relative to the energy of *trans*-N_2H_2 (1 kcal/mol ≈ 350 cm^{-1} ≈ 503 K). Data are taken from Refs. [55] and [56].

by optical excitation of the $A\,^3\Pi \leftarrow a\,^1\Delta$ transition followed by spontaneous emission (see Fig. 1.5) [63]. A recent experiment showed that the NH($X\,^3\Sigma^-$) radicals thus produced can be trapped in a magnetic field at a temperature of a few millikelvin [64]. This deceleration-pumping scheme also allows reloading of the magnetic trap, providing a means to increase phase-space density.

Full quantum-degeneracy of NH may be achieved either by sympathetic cooling with a quantum-degenerate atomic gas (e.g. with N [61, 65], Li [66], or Mg [67]) or by evaporative cooling. The latter is considered the most attractive route toward experimental BEC formation, as it involves the cooling of only one species rather than two. Nevertheless, it remains to be seen whether the collisional properties of NH + NH are favorable for efficient evaporative cooling. This question may be addressed by high-level quantum calculations. Theoretical knowledge of the NH + NH collision dynamics is, however, not only necessary to assess the feasibility of evaporative cooling, but also to describe the many-body physics of a BEC or fermionic condensate composed of NH radicals. Furthermore, a rigorous theoretical study of the NH–NH system may serve as an important benchmark for other magnetically trapped dipolar molecules, the dynamics of which are still largely unexplored.

The aim of this work is to describe and analyze the NH + NH collision dynamics by means of state-of-the-art quantum-theoretical methods. We consider elastic, inelastic, and reactive collisions both in the presence and absence of a magnetic field, and focus specifically on the prospects for evaporative cooling. The various spin-changing processes that lead to inelastic trap loss are also examined in detail. In particular the

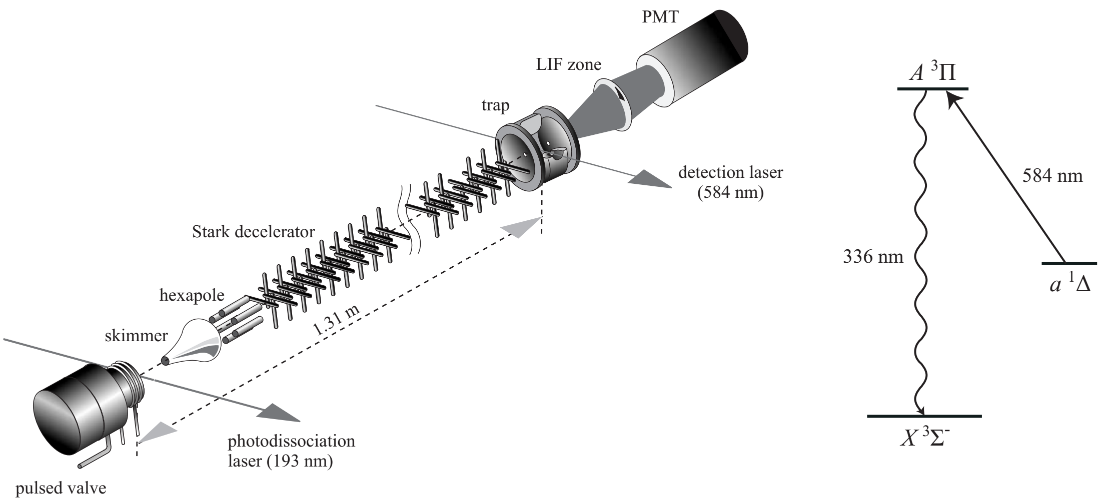

Figure 1.5: Stark deceleration scheme for NH. The NH($a\,^1\Delta$) molecules are created by photodissociation of HN_3 seeded in Kr. The molecular beam passes through a skimmer, hexapole, and Stark decelerator. The decelerated molecules are subsequently loaded into an electrostatic trap. The probing and pumping to the $X^3\Sigma^-$ ground state occurs through 584 nm laser light. The figure is adapted from Ref. [62].

role of intermolecular magnetic dipole-dipole interaction, one of the most important trap-loss mechanisms for paramagnetic species, is extensively studied. Moreover, we provide insight into the chemical reaction dynamics of NH and explore the possibilities for external field control of cold chemical reactions.

As an introduction to the following chapters, we now briefly discuss the possible collision events that can occur in a gas of cold NH radicals. NH($X\,^3\Sigma^-$) has two unpaired electrons in nonbonding π orbitals, giving it a net electronic spin of $S_{\text{NH}} = 1$ and a space-fixed spin projection of $M_{S_{\text{NH}}} = 1, 0,$ or -1. In a magnetic trapping environment, with the minimum of the field in the center of the trap, each triplet molecule is polarized in the low-field-seeking spin-up state, $|S_{\text{NH}} = 1, M_{S_{\text{NH}}} = 1\rangle$ (see Fig. 1.3). A collision complex of two such molecules is in the quintet $|S = 2, M_S = 2\rangle$ state, with S denoting the total electronic spin and M_S the spin projection onto the magnetic-field axis. If the collision proceeds elastically, the monomers exchange only translational energy, leaving the internal quantum states unaffected. That is, both molecules remain trapped. Inelastic collisions, on the other hand, which are governed by weak spin-dependent couplings, can change either the M_S quantum number of the quintet state or the total spin S to produce triplet ($S = 1$) or singlet ($S = 0$) complexes. Both M_S- and S-changing collisions lead to trap loss, as the spin-projection quantum number of at least one of the molecules ($M_{S_{\text{NH}}}$) is changed. Furthermore, the triplet and singlet potentials are chemically reactive, and S-changing collisions may therefore also yield new chemical species (see Figs. 1.4 and 1.6). All of the above-mentioned processes can, in principle, occur at arbitrarily low collision energies.

1.4 Theoretical methods

The calculation of elastic, inelastic, and reactive NH + NH cross sections requires the solution of the time-independent Schrödinger equation for both the electronic and nuclear degrees of freedom. A common approach is to invoke the Born-Oppenheimer (BO) approximation, which assumes that the nuclei are frozen on the time scale of the electronic motion. Solving the complete Schrödinger equation within the BO framework thus proceeds in two steps: first, the electronic part is solved for fixed positions of the nuclei, yielding a set of eigenenergies as a function of the nuclear coordinates. These energies, referred to as potential energy surfaces, represent a multi-dimensional "energy landscape" on which the system evolves (see Fig. 1.6). Next, the nuclear Schrödinger equation is solved using the potential energy surface(s) as input. The latter step provides all possible information on the collision dynamics. In general, the BO approximation is accurate when nonadiabatic couplings between different electronic states are small. This holds, e.g., for potentials that are well separated in energy. In the case of NH + NH, the three interaction potentials become degenerate at long range, but they all correspond to different spin states. Hence, the nonadiabatic couplings are zero and the approximation remains valid.

1.4.1 Electronic structure theory

In this section, we give a brief overview of the different electronic structure methods available for the calculation of potential energy surfaces. Virtually all state-of-the-art *ab initio* methods are based on Hartree-Fock (HF) theory, a mean-field approach in which the electronic wave function is described by a single Slater determinant (see e.g. Ref. [68]). The HF approximation assumes that each electron experiences an average potential from all other electrons, neglecting the electron correlation arising from pairwise Coulombic repulsion. The molecular orbitals produced in a HF calculation are written as linear combinations of atomic orbitals, the expansion coefficients of which are optimized in a variational self-consistent-field procedure. The corresponding HF energy is, by definition, the lowest possible electronic energy for a single-Slater-determinant wave function. An important aspect of HF theory is that it is rigorously size-consistent, i.e., for two non-interacting subsystems A and B, the calculated energy of the supersystem $A \cdots B$ is equal to the sum of the energies of the individual subsystems. This property is of particular importance in supermolecular calculations of long-range interactions. Among the different implementations of HF theory we may distinguish three types: restricted (RHF), unrestricted (UHF), and restricted open-shell HF (ROHF). Restricted methods require the wave function to be an eigenfunction of the total spin and spin-projection operators, while the unrestricted version imposes no such constraints [68]. The UHF wave function may thus contain a mixture of different electronic-spin states.

In order to account for electron correlation, it is necessary to go beyond the single-determinant HF approximation. We start by discussing two widely used *single-reference* correlation methods that take the HF wave function as the reference state. In the

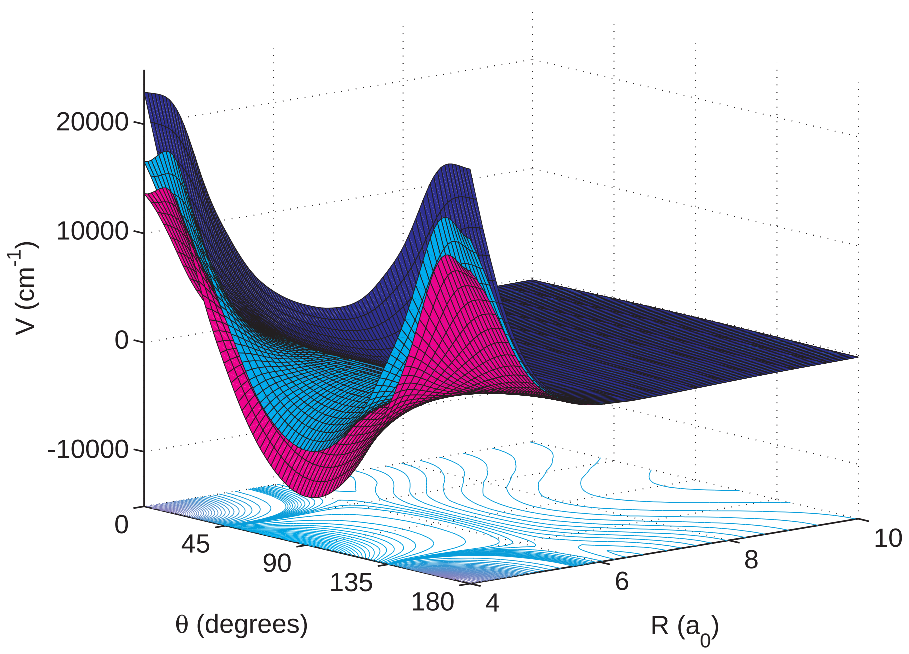

Figure 1.6: Cuts through the quintet (dark blue), triplet (cyan), and singlet (magenta) potential energy surfaces of NH($X\,^3\Sigma^-$) – NH($X\,^3\Sigma^-$). The molecules are treated at rigid rotors, and the geometries are defined in terms of the four Jacobi coordinates R, θ_A, θ_B, and ϕ. The coordinate R is the length of the vector $\boldsymbol{R}$ that connects the two centers of mass, θ_A and θ_B are the polar angles of the monomer axes relative to $\boldsymbol{R}$, and ϕ is the dihedral angle between the planes through the monomer axes and $\boldsymbol{R}$. The cuts shown here correspond to planar geometries with $\phi = 180°$ and $\theta = \theta_A = \theta_B$. Note that the quintet potential is completely repulsive at small R, while the triplet and singlet states are chemically reactive.

single-reference Configuration Interaction (CI) method [68], the total wave function is written as a linear combination of Slater determinants, each of which corresponds to a different orbital occupation. The CI coefficients are obtained in a variational manner. If *all* possible Slater determinants are included in the wave function, i.e. if all electrons can be excited to all unoccupied spin-orbitals, we arrive at the full CI result. This is the *exact* solution to the non-relativistic electronic Schrödinger equation for a given orbital basis. The full CI method is, however, extremely expensive in terms of computational costs, and is therefore only practical for few-electron systems and small basis sets. A more feasible approach is to use truncated CI, a technique in which a limited number of electrons (typically one or two) can be excited from occupied to unoccupied orbitals. The main disadvantage of truncated CI is that it suffers from a fundamental lack of size consistency, making it unreliable at large interparticle separations. This is particularly problematic for studies of cold and ultracold collisions, in which the long-range potential plays an important role.

An alternative – and generally more attractive – single-reference method is Coupled Cluster (CC) theory. The CC model is based on an exponential *ansatz* for the wave function,

$$|\mathrm{CC}\rangle = \exp(\hat{T})|\mathrm{HF}\rangle, \tag{1.1}$$

where $|\mathrm{CC}\rangle$ and $|\mathrm{HF}\rangle$ denote the CC and HF wave functions, respectively, and $\hat{T}$ is the so-called cluster operator. The latter consists of a sum of electron-excitation operators that can be truncated at any given excitation level. Note that such a truncated operator still generates *all* possible Slater determinants (of the correct space and spin symmetries) due to its exponential parametrization [cf. $\exp(\hat{A}) = \sum_{n=0}^{\infty} \hat{A}^n/n!$] [68]. The exponential form of Eq. (1.1) yields, in principle, a fully size-consistent solution, regardless of the level of truncation. In the case that $\hat{T}$ is untruncated, we recover the full CI limit.

By far the most popular version of CC theory is CC with single and double excitations and a perturbative treatment of triples [CCSD(T)]. This technique represents a satisfactory compromise between the relatively cheap CCSD method, in which the cluster operator is truncated at the doubles level, and the expensive but accurate CCSDT method, which includes up to triple excitations in $\hat{T}$ [68]. Although the implementation of CCSD(T) is well established for closed-shell systems, a generalization to open-shell species has proven a rather challenging task. Current state-of-the-art open-shell CCSD(T) methods use a ROHF wave function as the reference state, and employ either a spin-unrestricted CCSD(T) [UCCSD(T)] or (partially) spin-adapted CCSD(T) [RCCSD(T)] scheme to account for electron correlation [69, 70, 71]. Such open-shell models may suffer, however, from a small lack of size consistency, a problem that still requires further study [71]. This issue will also be addressed in the next chapter. Finally, we note that the above-mentioned CC methods apply only to high-spin open-shell systems for which the reference state can be written as a single Slater determinant. A generally accepted CC treatment for low-spin open-shell systems has not been established yet.

Systems that are dominated by more than one electronic configuration, e.g. the singlet and triplet spin states of NH–NH, require *multi-reference* correlation methods. In such cases, the reference wave function is obtained from a Multi-Reference Self-Consistent-Field (MCSCF) calculation, an approach that generalizes HF theory to multi-configuration systems [72, 73, 68]. The most common version of MCSCF theory is the Complete Active Space SCF (CASSCF) method, which takes the HF molecular orbitals as starting orbitals and divides these into three subspaces: inactive, active, and virtual orbitals. The inactive orbitals are permanently doubly occupied, and the remaining electrons occupy the active space. Virtual orbitals are left unoccupied. The CASSCF method generates a linear combination of Slater determinants by allowing electron excitations within the active space. In order to obtain the wave function with the lowest possible energy, the coefficients of the determinants and the molecular orbitals are variationally optimized. In the extreme case that the active space extends over the entire orbital manifold, the CASSCF method yields the full CI result. In practice, however, a CASSCF calculation is usually performed only to produce a *qualitatively* correct wave function with proper multi-configuration character.

Subsequent correlation corrections can be obtained using either Multi-Reference Configuration Interaction (MRCI) [74, 75, 68] or Multi-Reference nth order Perturbation Theory (CASPTn) [76, 68]. The MRCI treatment uses the Slater determinants and orbitals of the CASSCF method, but also allows excitations from active to virtual orbitals. The practical limitations of MRCI are, however, similar to those of the single-reference case: full CI is generally too expensive, while truncated MRCI suffers from a lack of size consistency. An alternative multi-reference approach is CASPTn, which gives an nth order perturbation estimate of the exact energy using the CASSCF state as the zero-order wave function. This method is reliable up to 3th or 4th order, but typically diverges as higher-order terms are included [68]. Although the CASPTn method is not exactly size-consistent, it approaches full size-consistency when the CASSCF reference state is dominated by a single Slater determinant [68]. Specifically, in the case that a system dissociates into two high-spin open-shell fragments, CASPTn calculations can be made rigorously size-consistent.

In Chapter 2 of this thesis, we will describe the calculation of accurate four-dimensional potential energy surfaces for NH + NH at the RCCSD(T) and CASPTn levels of theory. Particular attention is drawn to the long-range interactions, making the potentials suitable for calculations in the ultralow temperature regime.

1.4.2 Scattering theory

Once the potential energy surfaces are known for all relevant geometries, we can proceed to solve the Schrödinger equation for the nuclear coordinates. In this section, we first discuss elastic and inelastic molecular scattering on a single potential. Reactive collisions and multiple surfaces will be briefly addressed at the end of this section, and more explicitly in Chapter 6. Throughout this thesis, we will restrict ourselves to binary collisions and leave three-body processes out of consideration.

Multichannel quantum scattering theory

Consider the scattering of two molecular species, A and B, described by the Hamiltonian

$$\hat{H} = -\frac{\hbar^2}{2\mu R}\frac{\partial^2}{\partial R^2}R + \frac{\hat{l}^2}{2\mu R^2} + V(\boldsymbol{R}, \tau_A, \tau_B) + \hat{H}_A(\tau_A) + \hat{H}_B(\tau_B). \tag{1.2}$$

Here, $\boldsymbol{R} \equiv R\hat{\boldsymbol{R}}$ represents the intermolecular vector between the centers of mass of A and B, τ_A and τ_B collectively label all relevant molecular coordinates, μ is the reduced mass of the complex, $\hat{l}^2$ is the angular momentum operator associated with rotation of $\boldsymbol{R}$, V is the intermolecular potential energy surface, and $\hat{H}_A$ and $\hat{H}_B$ are the Hamiltonians for the isolated molecules. The latter terms may contain, e.g., rotational, vibrational, and spin-dependent contributions. We now seek to find numerical solutions to the time-independent Schrödinger equation by means of coupled-channels theory. This theory represents the most rigorous treatment of time-independent quantum scattering dynamics, and provides, in principle, numerically exact results.

In the coupled-channels formalism [77, 78], the scattering Hamiltonian is written as the sum of the radial kinetic energy operator and the remainder ($\Delta\hat{H}$),

$$\begin{aligned} \hat{H} &= -\frac{\hbar^2}{2\mu R}\frac{\partial^2}{\partial R^2}R + \Delta\hat{H}, \\ \Delta\hat{H} &= \frac{\hat{l}^2}{2\mu R^2} + V(\boldsymbol{R}, \tau_A, \tau_B) + \hat{H}_A(\tau_A) + \hat{H}_B(\tau_B), \end{aligned} \tag{1.3}$$

and the Schrödinger equation is written as

$$\frac{\hbar^2}{2\mu R}\frac{\partial^2}{\partial R^2}R\psi = (\Delta\hat{H} - E)\psi, \tag{1.4}$$

with E denoting the total energy. Each solution $\psi_n = \psi_n(\boldsymbol{R}, \tau_A, \tau_B)$ is expanded as

$$\begin{aligned} \psi_n(\boldsymbol{R}, \tau_A, \tau_B) &= \frac{1}{R}\sum_{n'} \phi_{n'}(\hat{\boldsymbol{R}}, \tau_A, \tau_B) F_{n'n}(R), \\ &\equiv \frac{1}{R}\sum_{n'} |n'\rangle F_{n'n}(R), \end{aligned} \tag{1.5}$$

where the functions $\phi_{n'}(\hat{\boldsymbol{R}}, \tau_A, \tau_B) \equiv |n'\rangle$ are so-called channel basis functions. These provide a basis for the eigenfunctions of the operators $\hat{l}^2$, $\hat{l}_z$, $\hat{H}_A$, and $\hat{H}_B$. Such eigenfunctions, each labeled by a unique set of quantum numbers, will be referred to as scattering channels. The expansion coefficients $F_{n'n}(R)$ appearing in Eq. (1.5) constitute a matrix $\boldsymbol{F}(R)$, the columns of which define the independent solutions ψ_n. These may be transformed into the final wave functions by applying scattering boundary conditions, as shown below. Substituting Eq. (1.5) into the Schrödinger equation of Eq. (1.4), multiplying from the left with the channel basis functions and integrating over all angular and molecular coordinates ($\hat{\boldsymbol{R}}$, τ_A, and τ_B) yields

$$\boldsymbol{F}''(R) = \boldsymbol{W}(R)\boldsymbol{F}(R), \tag{1.6}$$

where the primes denote differentiation with respect to R. The elements of the so-called coupling matrix $\boldsymbol{W}(R)$ are given by

$$W_{n'n}(R) = \frac{2\mu}{\hbar^2}\langle n'|\Delta\hat{H} - E|n\rangle. \tag{1.7}$$

The second-order differential equations of Eq. (1.6) are known as the close-coupling or coupled-channels equations. These can be solved, subject to the appropriate boundary conditions, by a range of numerical techniques, e.g. by log-derivative or renormalized Numerov propagation [79]. We will discuss the former method below, and describe the renormalized Numerov technique in Chapter 6.

Log-derivative propagation

In order to solve Eq. (1.6), the radial coordinate is first discretized into a grid of points R_i $(i = 0, \ldots, m)$. The functions $\boldsymbol{F}(R)$ may subsequently be propagated from R_0 to R_m to yield the complete set of solutions. Such an approach, however, can lead to numerical instabilities when one or more channels are classically inaccessible [80]. These issues can be avoided by employing a so-called embedding-type propagation method [81], an example of which is the log-derivative scheme. In this technique, the propagation is performed using the log-derivative matrix $\boldsymbol{Y}(R)$, which relates the expansion coefficients to their first derivatives [79, 82],

$$\boldsymbol{F}'(R) = \boldsymbol{Y}(R)\boldsymbol{F}(R). \tag{1.8}$$

We start by considering the boundary conditions near the origin. A common strategy is to first diagonalize the coupling matrix $\boldsymbol{W}$ in the point $R = R_0$ to obtain a local channel eigenbasis,

$$\boldsymbol{W}(R_0)\boldsymbol{U}(R_0) = \boldsymbol{U}(R_0)\boldsymbol{\Lambda}(R_0), \tag{1.9}$$

where $\boldsymbol{\Lambda}(R_0)$ is a diagonal matrix of eigenvalues, and the columns of $\boldsymbol{U}(R_0)$ represent the corresponding eigenvectors. Negative eigenvalues are associated with locally open (energetically accessible) channels, with squared wave vectors $(k_q^{(0)})^2 = -\Lambda_{qq} > 0$, and positive eigenvalues correspond to locally closed channels $[(k_q^{(0)})^2 = -\Lambda_{qq} < 0]$. In the present discussion, we consider only non-reactive collisions on a repulsive short-range potential and assume that all channels are closed at small R. For reactive scattering boundary conditions, we refer to Sec. 6.2 and Refs. [78, 83]. Once the coupling matrix at $R = R_0$ is diagonalized, we can transform the matrix $\boldsymbol{F}(R)$ to the local channel eigenfunction basis,

$$\tilde{\boldsymbol{F}}(R) = \boldsymbol{U}^\dagger(R_0)\boldsymbol{F}(R), \tag{1.10}$$

with the dagger representing the Hermitian conjugate, and we may write, for $R \approx R_0$,

$$\tilde{\boldsymbol{F}}''(R) = \boldsymbol{U}^\dagger(R_0)\boldsymbol{W}(R)\boldsymbol{U}(R_0)\tilde{\boldsymbol{F}}(R) \approx \boldsymbol{\Lambda}(R_0)\tilde{\boldsymbol{F}}(R), \tag{1.11}$$

where we have assumed that the coupling matrix is constant near $R = R_0$. The $\tilde{\boldsymbol{F}}(R)$ matrix in Eq. (1.11) can be written in diagonal form, with each diagonal element corresponding to a different local channel eigenfunction. This results in a set of *uncoupled*, one-dimensional second-order differential equations. We now impose boundary conditions on the matrix $\tilde{\boldsymbol{F}}(R)$ by requiring that all functions vanish exponentially at small R,

$$\tilde{F}_{pq}(R) \sim \delta_{pq} e^{k_q^{(0)} R}, \tag{1.12}$$

with $k_q^{(0)} = \sqrt{|\Lambda_{qq}|}$. The log-derivative matrix in the local channel eigenfunction basis is also diagonal at $R = R_0$,

$$\tilde{Y}_{pq}(R_0) = [\boldsymbol{U}^\dagger \boldsymbol{Y}(R_0)\boldsymbol{U}]_{pq} = \delta_{pq} k_q^{(0)}, \tag{1.13}$$

and the boundary conditions for the $\boldsymbol{Y}$ matrix in the original basis are

$$\boldsymbol{Y}(R_0) = \boldsymbol{U}(R_0)\tilde{\boldsymbol{Y}}(R_0)\boldsymbol{U}^\dagger(R_0). \tag{1.14}$$

In order to propagate the log-derivative matrix from R_0 to R_m, we define an embedding-type propagator on each interval $[R_i, R_{i+1}]$ [84],

$$\begin{pmatrix} \boldsymbol{F}_i' \\ \boldsymbol{F}_{i+1}' \end{pmatrix} = \begin{pmatrix} \mathcal{Y}_1^{(i)} & \mathcal{Y}_2^{(i)} \\ \mathcal{Y}_3^{(i)} & \mathcal{Y}_4^{(i)} \end{pmatrix} \begin{pmatrix} -\boldsymbol{F}_i \\ \boldsymbol{F}_{i+1} \end{pmatrix}, \tag{1.15}$$

with $\boldsymbol{F}_i \equiv \boldsymbol{F}(R_i)$. One of the simplest ways to find the propagator is by first diagonalizing the $\boldsymbol{W}$ matrix in the middle of the interval and assuming it to be constant. The propagator for these one-dimensional problems is known analytically, and the result can be transformed back to the original basis. The log-derivative matrix in the point $R = R_i$, defined by

$$\boldsymbol{F}_i' = \boldsymbol{Y}(R_i)\boldsymbol{F}_i, \tag{1.16}$$

may subsequently be propagated to $R = R_{i+1}$ using the relation

$$\boldsymbol{Y}(R_{i+1}) = \mathcal{Y}_4^{(i)} - \mathcal{Y}_3^{(i)} \left[\boldsymbol{Y}(R_i) + \mathcal{Y}_1^{(i)}\right]^{-1} \mathcal{Y}_2^{(i)}. \tag{1.17}$$

This procedure is repeated until the final point $R = R_m$ is reached.

S-matrix boundary conditions

If R_m is so large that the interaction potential $V(R_m)$ can be neglected, we may apply asymptotic boundary conditions to obtain the final wave functions. We first consider the asymptotic solutions of the Schrödinger equation long *before* the collision. In that case, the exact solutions are written as a product of molecular eigenstates and a plane wave,

$$\begin{aligned} \Psi_{q_A,q_B} &\sim |q_A, q_B\rangle e^{i\boldsymbol{k}_q\boldsymbol{R}} && (1.18) \\ &= |q_A, q_B\rangle \frac{2\pi}{R} \sum_{l=0}^{\infty} \sum_{m_l=-l}^{l} R\left[h_l^{(1)}(k_qR) + h_l^{(2)}(k_qR)\right] \\ &\quad \times i^l Y_{l,m_l}(\hat{\boldsymbol{R}}) Y_{l,m_l}^*(\hat{\boldsymbol{k}}_q), && (1.19) \end{aligned}$$

where $|q_A, q_B\rangle \equiv |q_A\rangle|q_B\rangle$ are the eigenfunctions of $\hat{H}_A$ and $\hat{H}_B$, with eigenvalues $\epsilon_A^{(q)}$ and $\epsilon_B^{(q)}$, $\boldsymbol{k}_q$ is the corresponding wave vector, $\boldsymbol{k}_q \equiv k_q\hat{\boldsymbol{k}}_q$, with $k_q^2 = 2\mu(E - \epsilon_A^{(q)} - \epsilon_B^{(q)})/\hbar^2$, $h_l^{(1)}$ and $h_l^{(2)}$ are spherical Hankel functions of the first and second kind, respectively, Y_{l,m_l} is a spherical harmonic, and the superscript * denotes complex conjugation. Note that $Y_{l,m_l}(\hat{\boldsymbol{R}})$ is an eigenfunction of both $\hat{l}^2$ and $\hat{l}_z$, with eigenvalues $\hbar^2 l(l+1)$ and $\hbar m_l$, respectively. The product $|q_A q_B\rangle Y_{l,m_l}(\hat{\boldsymbol{R}}) \equiv |q\rangle$ thus represents a unique scattering channel. The radial functions $Rh_l^{(1)}(k_qR)$ and $Rh_l^{(2)}(k_qR)$, which are associated with a radial flux of $+\hbar/\mu k_q$ and $-\hbar/\mu k_q$, respectively, describe the *outgoing* and *incoming* flux for each channel $|q\rangle$.

Let us now evaluate the wave functions long *after* the collision. It can be shown that, for any initial quantum state $|q_Aq_B\rangle$, the asymptotic scattering solutions must satisfy [77, 78, 85]

$$\begin{aligned}\Psi_{q_A,q_B} \sim \; & \frac{2\pi}{R}\sum_{l,m_l}\sum_{q'_A,q'_B}\sum_{l',m'_l}|q'_Aq'_B\rangle R\Big[h_{l'}^{(2)}(k_{q'}R)\delta_{q'_A,q_A}\delta_{q'_B,q_B}\delta_{l',l}\delta_{m'_l,m_l} \\ & +h_{l'}^{(1)}(k_{q'}R)S_{q'_A,q'_B,l',m'_l;q_A,q_B,l,m_l}\Big]\, i^lY_{l',m'_l}(\hat{\boldsymbol{R}})Y^*_{l,m_l}(\hat{\boldsymbol{k}}_q), \qquad (1.20)\end{aligned}$$

with $\sum_{q'_A,q'_B,l',m'_l}|S_{q'_A,q'_B,l',m'_l;q_A,q_B,l,m_l}|^2 = 1$, and for each scattering channel $|q\rangle$ with angular momentum quantum numbers $l = l_q$ and $m_l = m_{l_q}$ we have

$$\Psi_q \sim \frac{1}{R}\sum_{q'}|q'\rangle R\left[h_{l'_q}^{(2)}(k_{q'}R)\delta_{q',q} + h_{l'_q}^{(1)}(k_{q'}R)S_{q',q}\right]. \qquad (1.21)$$

The so-called S-matrix elements $S_{q'_A,q'_B,l',m'_l;q_A,q_B,l,m_l} = S_{q',q}$ represent the transition amplitudes for going from one channel to another. If the S-matrix is known for sufficiently many initial and final channels, all possible observables of the collision process, e.g. state-to-state cross sections and rate constants, can be readily determined. Total flux conservation requires that the S-matrix be unitary. In the special case that the potential is zero for all R, the S-matrix becomes a unit matrix and Eq. (1.20) reduces to Eq. (1.19).

In order to extract the S-matrix from the log-derivative matrix at $R = R_m$, we first require a transformation to the exact asymptotic channel eigenbasis. The matrix that contains the simultaneous eigenvectors of $\hat{l}^2$, $\hat{l}_z$, $\hat{H}_A$, and $\hat{H}_B$ in the original channel basis [Eq. (1.5)] will be denoted as $\boldsymbol{U}(R_m)$. At $R = R_m$, the matrix $\boldsymbol{F}(R)$ is transformed to the asymptotic eigenbasis as

$$\tilde{\boldsymbol{F}}(R) = \boldsymbol{U}^\dagger(R_m)\boldsymbol{F}(R), \qquad (1.22)$$

with each row and column of $\tilde{\boldsymbol{F}}(R)$ corresponding to a different scattering channel $|q\rangle$. We now apply asymptotic boundary conditions by expressing Eq. (1.21) as

$$\Psi_q \sim \frac{1}{R}\sum_{q'}|q'\rangle\tilde{F}_{q'q}(R), \qquad (1.23)$$

with

$$\tilde{\boldsymbol{F}}(R) = \tilde{\boldsymbol{I}}(R) + \tilde{\boldsymbol{O}}(R)\boldsymbol{S}. \qquad (1.24)$$

Here, $\tilde{\boldsymbol{I}}(R)$ is a diagonal matrix containing flux-normalized *incoming* waves for each channel $|q\rangle$,

$$\tilde{I}_{pq}(R) = \sqrt{\frac{\mu k_q}{\hbar}}Rh_{l_q}^{(2)}(k_qR)\delta_{pq}, \qquad (1.25)$$

and $\tilde{\boldsymbol{O}}(R)$ contains the flux-normalized *outgoing* waves,

$$\tilde{O}_{pq}(R) = \sqrt{\frac{\mu k_q}{\hbar}} R h^{(1)}_{l_q}(k_q R)\delta_{pq}. \tag{1.26}$$

Note that $\tilde{O}_{pq}(R) = \tilde{I}^*_{pq}(R)$. Substitution of Eqs. (1.22) and (1.24) into (1.8) yields

$$\boldsymbol{S} = -[\boldsymbol{Y}(R_m)\boldsymbol{O}(R_m) - \boldsymbol{O}'(R_m)]^{-1}[\boldsymbol{Y}(R_m)\boldsymbol{I}(R_m) - \boldsymbol{I}'(R_m)], \tag{1.27}$$

with $\boldsymbol{I}(R) = \boldsymbol{U}(R_m)\tilde{\boldsymbol{I}}(R)$ and $\boldsymbol{O}(R) = \boldsymbol{U}(R_m)\tilde{\boldsymbol{O}}(R)$. Equation (1.27) thus relates the scattering matrix $\boldsymbol{S}$ to the log-derivative matrix $\boldsymbol{Y}(R_m)$ in the original channel basis.

Cross sections

Once the S-matrix is known, we can proceed to calculate the state-to-state collision cross sections $\sigma_{q_A q_B \to q'_A q'_B}$. The differential cross sections for a given incident direction $\hat{\boldsymbol{k}}_q$ and an asymptotic outgoing direction $\hat{\boldsymbol{R}}$ are calculated as [86]

$$\frac{d\sigma_{q_A q_B \to q'_A q'_B}(\hat{\boldsymbol{k}}_q)}{d\hat{\boldsymbol{R}}} = \frac{1}{k_q^2}\left|f_{q_A q_B \to q'_A q'_B}\right|^2, \tag{1.28}$$

where $f_{q_A q_B \to q'_A q'_B}$ is the so-called scattering amplitude for the $q_A q_B \to q'_A q'_B$ transition,

$$f_{q_A q_B \to q'_A q'_B} = 2\pi \sum_{l,m_l}\sum_{l',m'_l} i^{l-l'} Y_{l',m'_l}(\hat{\boldsymbol{R}}) Y^*_{l,m_l}(\hat{\boldsymbol{k}}_q) T_{q'_A,q'_B,l',m'_l;q_A,q_B,l,m_l}, \tag{1.29}$$

and the T-matrix elements are defined as $T_{q'_A,q'_B,l',m'_l;q_A,q_B,l,m_l} = \delta_{q'_A,q_A}\delta_{q'_B,q_B}\delta_{l',l}\delta_{m'_l,m_l} - S_{q'_A,q'_B,l',m'_l;q_A,q_B,l,m_l}$. The integral state-to-state cross sections can be obtained by integrating Eq. (1.28) over all directions of the outgoing flux and by averaging over all incoming directions,

$$\begin{aligned}\sigma_{q_A q_B \to q'_A q'_B} &= \frac{1}{4\pi}\int d\hat{\boldsymbol{k}}_q \int \frac{d\sigma_{q_A q_B \to q'_A q'_B}(\hat{\boldsymbol{k}}_q)}{d\hat{\boldsymbol{R}}} d\hat{\boldsymbol{R}} \\ &= \frac{\pi}{k_q^2}\sum_{l,m_l}\sum_{l',m'_l} |T_{q'_A,q'_B,l',m'_l;q_A,q_B,l,m_l}|^2. \end{aligned} \tag{1.30}$$

When the colliding molecules A and B are identical, the integral cross sections should be multiplied by a factor of $(1 + \delta_{q_A,q_B})$ [87]. Throughout this thesis, we will apply Eq. (1.30) to the case of two identical NH molecules to extract the scattering cross sections as a function of collision energy and magnetic field strength.

Practical considerations

The S-matrix and cross sections obtained from a quantum coupled-channels calculation are in principle exact, provided that the radial grid and the channel basis set are sufficiently large to ensure convergence. However, the computational cost of a multichannel calculation scales with the *third* power of the number of channels, making it infeasible for systems with many degrees of freedom. Also collision complexes with relatively deep potential wells, for which many rotational or rovibrational states are needed, or open-shell molecules, with various possible spin states, pose a major computational challenge. A common approach to overcome this problem is to employ a channel basis in which the Hamiltonian is block-diagonal, thereby reducing the full-dimensional coupled-channels equations to a set of lower-dimensional ones. For instance, in the absence of an external field, the total angular momentum of a system ($\mathcal{J}$) is rigorously conserved, allowing the scattering calculations to be performed for each $\mathcal{J}$-value separately [77]. Such calculations will be presented in Chapter 3. When an external magnetic field is present, as in the case of magnetically trapped NH molecules, only the projection of $\mathcal{J}$ onto the magnetic-field axis ($\mathcal{M}$) is conserved. Hence, we may solve the coupled-channels equations for each value of $\mathcal{M}$ (see Chapters 4 and 5). The problem can be further simplified by exploiting, e.g., parity conservation and identical-particle symmetry. Despite these considerations, however, a fully converged inelastic scattering calculation is still virtually impossible for open-shell systems such as NH + NH. Nevertheless, as will be discussed in Chapters 3 and 4, even an incompletely converged basis set can provide useful information on the collision dynamics.

For the study of reactive collisions, the scattering problem becomes even more challenging. In general, a complete quantum mechanical description of a polyatomic reaction requires one or more $(3N-6)$-dimensional potential energy surfaces to enter the Schrödinger equation, with N denoting the total number of atoms. The coupled-channels equations must subsequently be solved for all rotational, vibrational, and spin degrees of freedom for both the reactants and products. A particularly difficult task lies in the choice of the coordinate system: the Jacobi coordinates that best describe the reactant arrangement are different from those of the product arrangement(s). Although several methods have been developed to address this problem (see e.g. Ref. [88]), an accurate, full-dimensional quantum treatment of cold NH + NH reactions is still infeasible. An alternative, more practical approach is to use a *single-arrangement* description of the reaction process, thereby treating the reaction as an inelastic scattering problem with reactive scattering boundary conditions. That is, rather than assuming a vanishing wave function as $R \to 0$ [cf. Eq. (1.12)], a part of the flux may also disappear at small R into reactive channels. Although the corresponding cross sections cannot be resolved for the product states, they provide a reasonable estimate for the *total* reactive cross sections of a given reactant state. In Chapter 6 of this thesis, we will present such a single-arrangement method for cold NH + NH reactions, both in the absence and presence of an external magnetic field. Concluding remarks on the NH + NH collision dynamics are also given at the end of Chapter 6.

Chapter 2

Potential energy surfaces

In this chapter, we present four-dimensional *ab initio* potential energy surfaces for the three different spin states of the NH($X\,^3\Sigma^-$) – NH($X\,^3\Sigma^-$) complex. The surface for the quintet state is obtained at the RCCSD(T)/aug-cc-pVTZ level of theory and the energy differences with the singlet and triplet states are calculated at the CASPTn/aug-cc-pVTZ ($n = 2, 3$) level of theory. The *ab initio* potentials are fitted to coupled spherical harmonics in the angular coordinates, and the long range is further expanded as a power series in $1/R$. The RCCSD(T) potential is corrected for a size-consistency error of about $0.5 \times 10^{-6}\ E_h$ prior to fitting. The long-range coefficients obtained from the fit are found to be in good agreement with first and second-order perturbation theory calculations.

2.1 Introduction

As mentioned in the previous chapter, NH is one of the most attractive candidates for (ultra)cold-molecule experiments. A quantum-degenerate gas of magnetically trapped NH molecules may be realized by means of evaporative cooling, a process that relies on strong elastic NH + NH collisions. A recent theoretical study by Kajita [89], in which only the electric dipole-induced dipole and magnetic dipole-dipole interactions were considered, showed that evaporative cooling of NH is likely to be feasible. A more rigorous quantum calculation of elastic and inelastic cross sections, however, requires knowledge of the full NH–NH interaction potentials for all three spin states (see Sec. 1.4). In particular the long-range potential, which governs the dynamics at (ultra)low temperatures, should be described very accurately. For NH–NH the dominant long-range term is the electrostatic dipole-dipole interaction, which scales with the intermolecular distance R as R^{-3}. If, however, the molecules are freely rotating, all multipole-multipole terms average out to zero and the isotropic (R^{-6}) dispersion and induction interactions become important.

Dhont *et al.* [90] have recently constructed four-dimensional *ab initio* potential energy surfaces for NH–NH which, in principle, contain all relevant long range contributions. They employed the partially spin-restricted coupled-cluster method with single and double excitations and a perturbative treatment of triples [RCCSD(T)] [69, 91] to obtain the surface for the NH–NH quintet state. We found, however, that this surface exhibits erroneous behaviour in the long range due to a lack of size consistency in the open-shell RCCSD(T) method. In the present work, we report more accurate *ab initio* calculations that are corrected for this undesirable feature, and which allow an analytical fit of the long-range potential. The fit of the short-range potentials is also improved.

This chapter is organized as follows. In Section 2.2.1, we first address the RCCSD(T) size-consistency problem and present new RCCSD(T) calculations for the long range of the NH–NH potential. Long-range perturbation theory calculations are discussed in Section 2.2.2, and new CASPTn ($n = 2, 3$) calculations for the short range of the singlet and triplet potentials are presented in Section 2.2.3. The fit of the different potentials is described in Section 2.3, followed by a discussion of the results in Section 2.4. Finally, concluding remarks are given in Section 2.5.

2.2 Electronic structure calculations

2.2.1 RCCSD(T) potential energy surface

The coupled-cluster (CC) approach is one of the most accurate *ab initio* methods available for calculating potential energy surfaces. This method requires a single Slater determinant function as the reference state, which in the case of NH–NH implies that only the high-spin quintet state is suitable for coupled-cluster calculations. At large intermolecular distances, however, the energy splittings between the three different spin states become negligible and the long-range CC potential also applies to the singlet and triplet states. In this section, we will show that the previously reported NH–NH RCCSD(T) potential [90] contains a size-consistency error that becomes apparent at large R. We also present new *ab initio* calculations that are corrected for this defect. The coordinates used to describe the NH–NH potential energy surfaces are the four intermolecular Jacobi coordinates (R, θ_A, θ_B, ϕ). The coordinate R is the length of the intermolecular vector $\boldsymbol{R}$ that connects the centers of mass of monomers A and B, θ_A and θ_B are the polar angles of the NH monomer axes relative to $\boldsymbol{R}$, and ϕ is the dihedral angle between the planes through $\boldsymbol{R}$ and the monomer axes (see Fig. 2.1). All interaction potentials are computed using the supermolecule approach with the counterpoise correction method of Boys and Bernardi [92].

Size consistency

It is well established that coupled-cluster theory for closed-shell systems is rigorously size-consistent. For open-shell species, however, where the problem of nonzero spin

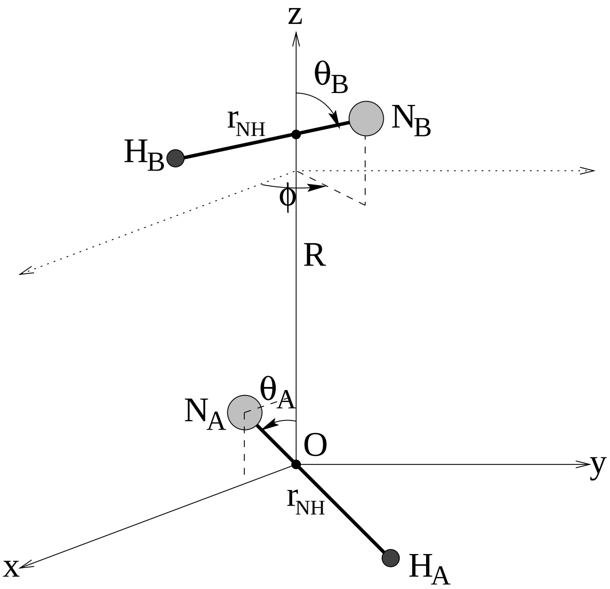

Figure 2.1: Jacobi coordinates used to describe the NH($X\,^3\Sigma^-$) – NH($X\,^3\Sigma^-$) complex. The vector $\boldsymbol{R}$ connects the centers of mass of the monomers, θ_A and θ_B are the polar angles of the NH monomer axes relative to $\boldsymbol{R}$, and ϕ is the dihedral angle between the planes through the monomer axes and $\boldsymbol{R}$. The figure is taken from Ref. [90].

arises, this issue is not straightforward. It was demonstrated in 2006 by Heckert *et al.* [71] that several spin-adapted CCSD schemes applied to the triplet F(^2P) – F(^2P) system exhibit size-consistency errors on the order of 10^{-7} – 10^{-8} hartree (E_h). The reason for this is still unclear, but it has been suggested that the problem lies in the truncation of the cluster operator [71]. Although the errors are very small, the effect becomes apparent when considering interactions at low temperatures, where the total energy of the system may be of a similar order of magnitude (10^{-7} $E_h \approx 0.03$ K). Hence, a lack of size consistency imposes a significant limitation on the accuracy of calculations in the (ultra)cold regime.

When evaluating the NH($^3\Sigma^-$) – NH($^3\Sigma^-$) quintet potential of Ref. [90] in more detail, we indeed found that the interaction energy does not tend to zero at large intermolecular distances. At $R = 30\,000\,a_0$, the size-consistency error is -4.8823×10^{-6} E_h calculated at the RCCSD level of theory with the augmented correlation-consistent polarized valence triple-zeta (aug-cc-pVTZ) basis set [93], and $+0.5129 \times 10^{-6}$ E_h at the RCCSD(T)/aug-cc-pVTZ level of theory. It should be noted that these errors are independent of the relative orientation of the monomers, i.e., the lack of size consistency affects only the isotropic part of the potential. The results for other basis sets are given in Table 2.1. It can be seen that the error is largest at the RCCSD level and increases with the size of the basis set. The inclusion of triple excitations reduces the error by approximately one order of magnitude and, for most basis sets, also changes its sign.

Although the problem has not been solved yet, we found that the RCCSD(T) quintet potential can be easily corrected for the lack of size consistency by simply

Table 2.1: Size-consistency errors (ΔE) for the NH–NH system at the RCCSD and RCCSD(T) levels of theory. The basis sets correspond to the (aug)-cc-pVnZ (n = double, triple, quadruple, quintuple) sets of Dunning [93]. The errors are calculated as the difference between the energy of the separate monomers and the energy of the supersystem NH$\cdots$NH at an intermolecular distance of 30 000 a_0. All values are in 10^{-6} E_h.

Basis set	ΔE RCCSD	ΔE RCCSD(T)
cc-pVDZ	−3.15067	−0.50946
cc-pVTZ	−4.25041	−0.01069
cc-pVQZ	−4.70853	0.36976
cc-pV5Z	−4.92130	0.62672
aug-cc-pVDZ	−4.04159	0.01944
aug-cc-pVTZ	−4.88230	0.51290
aug-cc-pVQZ	−5.01375	0.68981
aug-cc-pV5Z	−5.03493	0.75827

subtracting the error, calculated at 30 000 a_0, from all *ab initio* points. We compared these corrected energies with the results obtained from a spin-unrestricted CCSD(T) [UCCSD(T)] calculation, of which the energies do converge to zero at long range [i.e. UCCSD(T) is size-consistent]. At $R = 30.0$ a_0, the root-mean-square (RMS) difference between the UCCSD(T) and corrected RCCSD(T) data was calculated to be 9.1×10^{-9} E_h (0.08% of the mean absolute value of the potential) for a grid of 126 *ab initio* points. Without the size-consistency correction this difference would be 5.1×10^{-7} E_h (4.4%). Thus, the error subtraction at the RCCSD(T) level leads to significantly better agreement with the size-consistent UCCSD(T) method. Similar results were obtained at an intermolecular distance of 15.0 a_0, where the RMS difference between the corrected RCCSD(T) and UCCSD(T) data is 7.0×10^{-8} E_h (0.07% of the mean absolute energy), as opposed to 5.4×10^{-7} E_h (0.54%) without the correction. At even smaller distances, the size-consistency error becomes increasingly negligible compared to the total interaction energy, and hence the correction will leave the short-range potential essentially unaffected. Based on these findings, we conclude that subtracting the error from all RCCSD(T) points does not significantly alter the accuracy of the potential, but it does give the desired asymptotic behaviour at long range.

Long-range RCCSD(T) calculations

Although the size-consistency correction already constitutes an important refinement to the RCCSD(T) potential of Ref. [90], we chose to improve the long range even further by performing new *ab initio* calculations. This is motivated by our aim to study collisions in the limit of zero temperature, for which it is desirable to have the long range in analytical form. In order to perform an accurate analytical fit, however, we found that the long-range *ab initio* energies should be converged to less than 10^{-10} E_h, while the data presented in Ref. [90] have been converged to only 10^{-8} E_h. We therefore recalculated the points at large R with much tighter convergence thresholds, as low as 10^{-13} E_h, to ensure that the fit will not be affected by numerical noise. The radial grid consisted of 8 points, approximately logarithmically spaced at 8.3, 10.0, 12.0, 14.4, 17.3, 20.8, 25.0, and 30.0 a_0. For the angular grid, we chose an 11-point Gauss-Legendre quadrature grid in (θ_A, θ_B) and an 11-point Gauss-Chebyshev grid in ϕ. These are known to be the most accurate quadratures on their respective domains [94]. Due to the symmetry of the complex, only points with $\theta_A + \theta_B \leq \pi$ and $0 \leq \phi \leq \pi$ were required in the calculations [90]. The monomers were treated as rigid rotors, with the NH bond length fixed to the experimental equilibrium value of 1.0362 Å [95]. The RCCSD(T) energies were computed using the aug-cc-pVTZ basis set, with additional bond functions located at the midpoint of the intermolecular vector $\boldsymbol{R}$ (exponents s, p: 0.9, 0.3, and 0.1; d, f: 0.6 and 0.2; g: 0.3). All calculations were performed with the MOLPRO package [96]. As explained above, the size-consistency error of 0.51290×10^{-6} E_h was subtracted from all RCCSD(T) points to ensure that the long range converges to zero.

2.2.2 Perturbation theory calculations

As an additional test for the accuracy of the RCCSD(T) long-range potential, we computed the long-range coefficients directly from first and second-order perturbation theory with the multipole expansion of the interaction operator (see e.g. Ref. [97]). The first-order (electrostatic) coefficients are expressed in terms of the permanent NH multipole moments, while the second-order (induction and dispersion) coefficients depend also on the static and dynamic polarizabilities of NH. The permanent multipole moments were obtained from finite field calculations at the RCCSD(T)/aug-cc-pVTZ level of theory and from density functional theory (DFT), yielding two different sets of first-order coefficients. All DFT calculations were performed with the PBE0 density functional [98] and the aug-cc-pVQZ basis set. The Kohn-Sham orbitals were obtained from a spin-restricted calculation using the DALTON program [99]. The Fermi-Amaldi asymptotic correction [100] was employed to improve the description of the NH densities. The ionization potentials used for this correction were taken from Ref. [101]. For the static and dynamic NH polarizabilities, we performed spin-restricted time-dependent coupled Kohn-Sham (CKS) calculations [101]. Previous studies have shown that CKS methods yield accurate van der Waals coefficients, comparable to the accuracies obtained with the best *ab initio* methods, for systems such as He_2, Ne_2, H_2O dimer [102], and the open-shell O_2 dimer [103]. The static polarizabilities and dynamic polarizabilities at imaginary frequencies were obtained with a modified version of the SAPT2008 package [104], extended to treat open-shell fragments. Finally, the second-order long-range coefficients were computed from the DFT multipole moments and response functions using the POLCOR program [105].

2.2.3 CASPTn calculations

As mentioned before, the RCCSD(T) quintet potential can also be used to describe the singlet and triplet NH–NH states at long range. In the short range, however, these lower-spin states must be treated with a different *ab initio* method. Dhont *et al.* [90] employed the Complete Active Space with nth-order Perturbation Theory (CASPTn) method ($n = 2, 3$) to calculate the energy differences between the quintet state and the $S = 0$ and 1 states, and added those to the RCCSD(T) quintet surface to obtain the singlet and triplet potentials:

$$V_n^S = V_{CASPTn}^S - V_{CASPTn}^{S=2} + V_{RCCSD(T)}^{S=2}. \tag{2.1}$$

When fitting the CASPTn energy splittings, which decay exponentially as a function of R, we found that the convergence thresholds used in Ref. [90] were not sufficiently stringent to reach the same accuracy as in the long range. Hence, we recalculated the CASPTn energies for all three spin states with much tighter convergence criteria. The active space consisted of the four orbitals that are singly occupied in the quintet state. The g_4 operator [106] was used to obtain size-consistent results, and a level shift of 0.4 was applied to enforce convergence. The interaction energies were computed for $R =$ 4.0, 4.5, 5.0, 5.5, 6.0, 6.5, 7.0, 7.5, 8.0, 8.5, 9.0, 10.0, 12.0, and 14.4 a_0, with the energy threshold set to 10^{-13} E_h for the points at 8.0 – 14.4 a_0, 10^{-12} E_h at 7.0 and 7.5 a_0, 10^{-11} E_h at 6.0 and 6.5 a_0, 10^{-10} E_h at 5.0 and 5.5 a_0, 10^{-9} E_h at 4.5 a_0, and 10^{-8} E_h at 4.0 a_0. For the angular grid we used the same points as for the long-range RCCSD(T) calculations, i.e. an 11-point Gauss-Legendre quadrature in (θ_A, θ_B) and an 11-point Gauss-Chebyshev grid in ϕ. The CASPTn calculations were performed with MOLPRO [96] using the aug-cc-pVTZ basis set supplemented with bond functions. It should be noted that three points at 4.0 a_0 failed to converge due to the strongly repulsive nature of the potential at small R.

2.3 Analytical representation

All three interaction potentials can be represented as follows:

$$\begin{aligned} V(R,\theta_A,\theta_B,\phi) &= \sum_{L_A,L_B,L} \upsilon_{L_A,L_B,L}(R) A_{L_A,L_B,L}(\theta_A,\theta_B,\phi) && (2.2)\\ &= \sum_{L_A,L_B,M} \upsilon_{L_A,L_B,M}(R) A_{L_A,L_B,M}(\theta_A,\theta_B,\phi). && (2.3)\end{aligned}$$

The angular functions are defined as

$$\begin{aligned} & A_{L_A,L_B,L}(\theta_A,\theta_B,\phi) \\ & \quad = \sum_{M=-\min(L_A,L_B)}^{\min(L_A,L_B)} \begin{pmatrix} L_A & L_B & L \\ M & -M & 0 \end{pmatrix} C_{L_A,M}(\theta_A,\phi_A)C_{L_B,-M}(\theta_B,\phi_B), \\ & \quad = \sum_{M=0}^{\min(L_A,L_B)} (-1)^M \begin{pmatrix} L_A & L_B & L \\ M & -M & 0 \end{pmatrix} A_{L_A,L_B,M}(\theta_A,\theta_B,\phi), \end{aligned} \tag{2.4}$$

where it is assumed that L_A+L_B+L is even due to the inversion symmetry of the total system [107]. The functions $C_{L,M}(\theta,\phi)$ are Racah-normalized spherical harmonics of degree L and order M, and $\phi=\phi_A-\phi_B$ is the difference between the azimuthal angles of monomers A and B. The factor in brackets denotes a Wigner three-j symbol. The 'primitive' angular functions $A_{L_A,L_B,M}(\theta_A,\theta_B,\phi)$ are given by

$$A_{L_A,L_B,M}(\theta_A,\theta_B,\phi) = P_{L_A,M}(\cos\theta_A)P_{L_B,M}(\cos\theta_B)\cos M\phi, \tag{2.5}$$

where $P_{L,M}(\cos\theta)$ are Schmidt semi-normalized associated Legendre functions defined in Eqs. (9) and (10) of Ref. [90]. The R-dependent expansion coefficients are related to each other as [90]

$$\upsilon_{L_A,L_B,L}(R) = (2L+1) \sum_{M=0}^{\min(L_A,L_B)} (-1)^M(2-\delta_{M0}) \begin{pmatrix} L_A & L_B & L \\ M & -M & 0 \end{pmatrix} \upsilon_{L_A,L_B,M}(R). \tag{2.6}$$

In the present work, we use an analytical expression for the $\upsilon_{L_A,L_B,L}(R)$ coefficients at long range, as outlined in the following Section. The short-range parts of the different interaction potentials are obtained by interpolating the $\upsilon_{L_A,L_B,L}(R)$ coefficients in R, as described in Sections 2.3.2 and 2.3.3. The short-range and long-range expansions are matched using an R-dependent switching function, the details of which are given in Section 2.3.2.

2.3.1 Long-range potential

For the analytical long-range interaction, we use Eq. (2.2) and further expand the $\upsilon_{L_A,L_B,L}(R)$ coefficients in a power series in $1/R$:

$$\upsilon_{L_A,L_B,L}(R) = \sum_n \frac{-C_{L_A,L_B,L,n}}{R^n}. \tag{2.7}$$

Our choice of an 11-point Gauss-Legendre quadrature in (θ_A, θ_B) and an 11-point Gauss-Chebyshev quadrature in ϕ ensures that the angular $A_{L_A,L_B,L}$ functions, when evaluated on the quadrature grid with the appropriate weights, are mutually orthogonal for all values of L_A and L_B up to 10 inclusive. Thus, we can perform the analytical fit in R [Eq. (2.7)] for each (L_A,L_B,L) term separately. The values of n follow from a consideration of the possible first-order (electrostatic) and second-order (induction/dispersion) contributions (see e.g. Ref. [107] for details). For the electrostatic terms, we have $L_A + L_B = L$ and $n = L_A + L_B + 1$, with $L_A \geq 1$ and $L_B \geq 1$. The minimum value of 1 comes from the fact that the lowest nonvanishing permanent multipole moment of NH is the dipole. In the case of induction and dispersion interactions, L_A and L_B correspond to the order of two coupled multipole moments on monomers A and B, respectively. That is, $L_A = |l_A - l'_A|, \ldots, l_A + l'_A$ and $L_B = |l_B - l'_B|, \ldots, l_B + l'_B$, where l_A, l'_A, l_B, and l'_B denote the orders of the uncoupled monomer multipole moments. L_A and L_B are in turn coupled to all possible L values, and for each (L_A,L_B,L) term we have $n = l_A + l'_A + l_B + l'_B + 2$. Finally, since each monomer is a linear Σ state molecule, it can be shown that $l_A + l'_A + L_A$ and $l_B + l'_B + L_B$ must be even [107].

The $C_{L_A,L_B,L,n}$ fit coefficients of Eq. (2.7) were calculated as follows. For each set of (L_A, L_B, L) values, we first computed the lowest possible values of n in both first and second order. Since our long-range *ab initio* calculations were performed on a grid of eight R points, we could include a maximum of eight R^{-n} functions in the fit. We then fitted the size-consistency corrected RCCSD(T) data to the expansion of Eq. (2.2), and subsequently fitted each $\upsilon_{L_A,L_B,L}$ expansion coefficient in terms of R^{-n} functions [Eq. (2.7)]. Note that the fit of Eq. (2.2) is mathematically equivalent to evaluating the overlap integral between the angular functions and $V(R, \theta_A, \theta_B, \phi)$ by Gauss-Legendre quadrature. The fit was done using a linear least-squares procedure in which the *ab initio* points were weighted with the appropriate quadrature weights and a factor of R^3. The R-dependent factor is chosen because the leading dipole-dipole interaction decays as R^{-3}.

In principle, our long-range expansion is valid for all terms up to $L_A = L_B = 10$, with eight possible values of n for each (L_A, L_B, L) term. However, the inclusion of high powers of $1/R$ may lead to unphysical results even for the low-n coefficients, which are considered the most important. Thus, we must carefully choose which $R^{-n}A_{L_A,L_B,L}(\theta_A, \theta_B, \phi)$ functions to include in the fit. After extensive testing, we found that the best analytical fit is obtained for $n \leq 14$. This result is based on a thorough examination of both the stability of the fit, i.e. how much the $C_{L_A,L_B,L,n}$ coefficients vary when adding more R^{-n} functions, and the RMS error in the data points. The final fit gave a RMS error of 4.6×10^{-8} E_h (0.03%) for a total of 10648 *ab initio* points. The RMS difference between the analytical potential and the size-consistency corrected long-range points of Ref. [90], which served as test points, was 4.8×10^{-7} E_h (0.24%). Note that the latter error is, in part, due to the weaker convergence thresholds used in the calculations of Ref. [90].

2.3.2 Short-range $S = 2$ potential

For the short range of the quintet surface, we used the size-consistency corrected RCCSD(T) data of Dhont *et al.* [90], calculated at R values from 4.0 to 16.0 a_0. The angular grid consisted of 11 points in θ_A and θ_B, ranging from 0° to 180° in steps of 20° with an additional point at 90°. The grid in ϕ ranged from 0° to 180° in steps of 22.5°. The short-range potential was first expanded in terms of $A_{L_A,L_B,M}(\theta_A,\theta_B,\phi)$ functions [Eq. (2.3)] and then transformed to Eq. (2.2). Instead of using the two-step spline-based approach described in Ref. [90], we employed a weighted least squares fitting procedure to determine the $\upsilon_{L_A,L_B,M}(R)$ coefficients for each R. In order to perform the fit, we first calculated optimal quadrature weights for the grid points in (θ_A,θ_B), the details of which are given in the Appendix. We then attempted to fit the RCCSD(T) points by an expansion in terms of $A_{L_A,L_B,M}(\theta_A,\theta_B,\phi)$ functions, weighting each point with the appropriate quadrature weights. High-energy points ($>$ 0.1 E_h), which are not of practical importance in bound-state and scattering calculations, were excluded from the fit. It was found, however, that the least squares problem of Eq. (2.3) is ill-conditioned for $\max(L_A,L_B) \geq 9$ due to both the choice of grid points (the angle ϕ is undefined if θ_A or θ_B equals 0° or 180°) and the omission of points at high energies. We therefore employed a modified fitting scheme to regularize the least squares problem such that all functions up to $L_A = L_B = 10$ and $M = 8$ could be included. This was done by means of a Tikhonov regularization method [108] in which the term $\sum_{L_A,L_B,M}|\alpha(L_A^2+L_B^2)\upsilon_{L_A,L_B,M}(R)|^2$ was added to the residual. The factor of $\alpha(L_A^2+L_B^2)$, with $\alpha = 2\times10^{-4}$, ensures that strong oscillations (associated with large L_A and L_B) are damped out in the fit. The resulting $\upsilon_{L_A,L_B,M}(R)$ fit coefficients were then transformed to $\upsilon_{L_A,L_B,L}(R)$ coefficients using Eq. (2.6). Overall, this fitting procedure gave a RMS error of 9.8×10^{-6} E_h (0.21%) based on 21275 *ab initio* points.

The $\upsilon_{L_A,L_B,L}(R)$ expansion coefficients were interpolated in R using the reproducing kernel Hilbert space (RKHS) method with the reproducing kernel for distancelike variables [109, 110]. The RKHS parameter m, which determines the power with which the interpolated function decays between the grid points, was set to the leading power in $1/R$ for each (L_A,L_B,L) term. For instance, the $\upsilon_{112}(R)$ coefficient containing the electrostatic dipole-dipole interaction was interpolated with $m = 3$, the isotropic $\upsilon_{000}(R)$ term was interpolated with $m = 6$, and so on. In all cases, the RKHS smoothness parameter was set to 2.

Finally, we matched the short-range and long-range expansions of the RCCSD(T) quintet potential using an R-dependent switching function $f(R)$ that changes smoothly from 0 to 1 on the interval $a < R < b$:

$$f(R) = \begin{cases} 0 & \text{if } R \leq a \\ 1 & \text{if } R \geq b \\ \frac{1}{2} + \frac{1}{4}\sin\frac{\pi x}{2}\left(3 - \sin^2\frac{\pi x}{2}\right) & \text{otherwise,} \end{cases} \tag{2.8}$$

with $x = \frac{(R-b)+(R-a)}{b-a}$. The function is such that the first three derivatives at $R = a$ and $R = b$ are zero. We used Eq. (2.8) to switch the potential between $a = 8$ and $b = 12$ a_0. The total $S = 2$ potential energy surface may now be expressed as follows:

$$V(R,\theta_A,\theta_B,\phi) = [1 - f(R)]V_{sr}(R,\theta_A,\theta_B,\phi) + f(R)V_{lr}(R,\theta_A,\theta_B,\phi), \tag{2.9}$$

where V_{sr} refers to the short-range expansion of Eq. (2.2) and V_{lr} to the long-range expansion of Eqs. (2.2) and (2.7).

2.3.3 Short-range $S = 0, 1$ potentials

As already mentioned in Section 2.2, the singlet and triplet potentials were obtained from the quintet RCCSD(T) potential by adding the energy differences at the CASPT2 or CASPT3 level of theory. We fitted these exchange splittings ($V^{S}_{CASPTn} - V^{S=2}_{CASPTn}$) directly in terms of $A_{L_A,L_B,L}(\theta_A, \theta_B, \phi)$ functions, weighting each point with the corresponding Gauss-Legendre and Gauss-Chebyshev quadrature weights. In all cases, the fit error was largest at 4.0 a_0 and rapidly decreased as a function of R. For instance, the RMS errors for the singlet-quintet CASPT2 and CASPT3 splittings were 1.3×10^{-3} E_h (4.6%) and 1.2×10^{-3} E_h (4.7%) at 4.0 a_0, 1.1×10^{-5} E_h (0.10%) and 7.8×10^{-6} E_h (0.09%) at the neighboring grid point of 4.5 a_0, and 2.3×10^{-8} E_h (0.007%) and 1.9×10^{-8} E_h (0.007%) near the van der Waals minimum at 6.5 a_0. For the triplet-quintet CASPT2 and CASPT3 exchange splittings, the RMS errors were 6.9×10^{-4} E_h (3.2%) and 7.9×10^{-3} E_h (4.4%) at 4.0 a_0, 4.3×10^{-6} E_h (0.06%) and 5.1×10^{-6} E_h (0.08%) at 4.5 a_0, and 2.1×10^{-8} E_h (0.01%) and 6.0×10^{-8} E_h (0.03%) at 6.5 a_0. All errors were calculated from 1331 *ab initio* points per R value, with the exception of $R = 4.0$ a_0, where three points failed to converge.

The $\upsilon_{L_A,L_B,L}(R)$ coefficients were interpolated in R using the RKHS method. For all (L_A, L_B, L) terms we set the RKHS parameter m to 14 and the smoothness parameter to 2. The value of $m = 14$ ensures that all coefficients decay as R^{-15} beyond the outermost grid point, thus decaying faster than any of the long-range terms included in the fit of Eq. (2.7). In addition, we found that the interpolation with $m = 14$ gives the smallest RMS error in the *ab initio* points of Ref. [90]. The expanded CASPTn splittings were added to the RCCSD(T) potential of Eq. (2.9) to obtain the final singlet and triplet potential energy surfaces.

2.4 Results and discussion

The main features of the singlet, triplet, and quintet potentials have already been described in Ref. [90], and therefore we only briefly mention them here. Our $S = 2$ potential is characterized by a van der Waals minimum at $R_e = 6.61$ a_0 with a well depth of $D_e = -675$ cm^{-1}. It should be noted that Dhont *et al.* [90] reported a slightly different R_e value of 6.60 a_0. The minimum corresponds to a linear geometry ($\theta_A = \theta_B = \phi = 0°$) in which the two NH dipoles are aligned. Żuchowski *et al.* [101] have recently shown that D_e changes to -693 cm^{-1} if the aug-cc-pVQZ basis is used and the RCCSD(T) calculations are performed without the frozen-core approximation. They also demonstrated from symmetry-adapted perturbation theory (SAPT) calculations that the main contributions to D_e are the electrostatic (-899 cm^{-1}) and dispersion (-432 cm^{-1}) interactions. The total SAPT exchange-repulsion energy at the minimum was found to be 874 cm^{-1} [101].

The $V_2^{S=0}$ ($V_3^{S=0}$) and $V_2^{S=1}$ ($V_3^{S=1}$) surfaces also exhibit a van der Waals minimum at $\theta_A = \theta_B = \phi = 0°$, located at $R_e = 6.50$ (6.51) and 6.54 (6.55) a_0, respectively. These distances are 0.01 – 0.02 a_0 different from the R_e values reported by Dhont *et* *al.* [90]. Furthermore, the singlet and triplet dimers may form the chemically stable N_2H_2 molecule, which is reflected in the strongly attractive nature of these potentials at short intermolecular separations. The most favorable geometries for the $S = 0$ and 1 states at short distances are found near $\theta_A = \theta_B = 90°$.

2.4.1 Long-range potential

Before discussing the analytical fit results, we first address the size-consistency problem occurring at the RCCSD and RCCSD(T) levels of theory. Figure 2.2 shows the isotropic part of the quintet potential, $v_{000}(R)$, between $R = 15$ and 30 a_0. The lack of size consistency is most apparent at the RCCSD level, giving rise to an error of -1.07 cm^{-1} at long range. The inclusion of triple excitations reduces the problem significantly, but in fact overcompensates for the RCCSD error by $+0.11$ cm^{-1}. The uncorrected isotropic RCCSD and RCCSD(T) potentials cross at $R \approx 11$ a_0. After subtracting the size-consistency errors from all *ab initio* points, both the RCCSD and RCCSD(T) potentials smoothly converge to zero at long range. It can also be seen that these corrected data are in very good agreement with the corresponding spin-unrestricted CC results at $R = 15$ and 30 a_0.

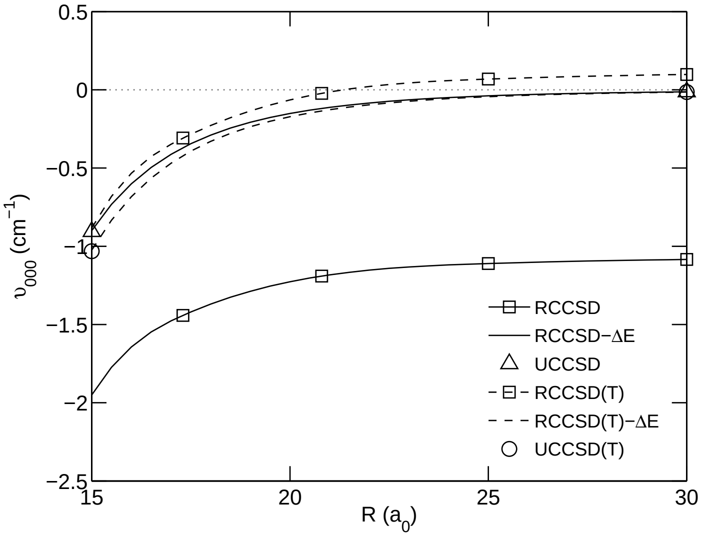

Figure 2.2: Isotropic part of the quintet potential calculated at the CCSD and CCSD(T) levels of theory. The data labeled "RCCSD" and "RCCSD(T)" correspond to the uncorrected spin-restricted data, "RCCSD-ΔE" and "RCCSD(T)-ΔE" to the size-consistency corrected data, and "UCCSD" and "UCCSD(T)" to the spin-unrestricted results.

The main fit results for the (size-consistency corrected) RCCSD(T) long-range potential are presented in Table 2.2. A total number of 588 $C_{L_A,L_B,L,n}$ coefficients was included in the long-range fit ($L_A, L_B \leq 10$ and $n \leq 14$), but here we list only the most important terms. Table 2.2 also shows the results obtained from first and second-order perturbation theory (PT). It can be seen that the fitted electrostatic terms agree very well with the PT coefficients, in particular with the data calculated at the PT–RCCSD(T) level of theory. For the induction and dispersion terms we find some significant discrepancies, but the most important second-order fit coefficients (those with $n = 6$) show satisfactory agreement with PT–DFT. It should be noted that, for the fitted coefficients, no distinction can be made between induction and dispersion contributions. For the isotropic $C_{0,0,0,6}$ term, the PT-DFT calculations give a dispersion coefficient of 39.86 a.u. and an induction term of 6.99 a.u.

Table 2.2: Most important long-range coefficients obtained from the fit and from perturbation theory, and their contributions at 30 a_0. The order of importance is based on the value of n, and for each n only the four largest terms are given. Terms labeled with an asterisk are first-order (electrostatic) interactions. All values are in atomic units. Numbers in parentheses denote powers of 10.

L_A	L_B	L	n	$C^{fit}_{L_A,L_B,L,n}$	$C^{PT-RCCSD(T)}_{L_A,L_B,L,n}$	$C^{PT-DFT}_{L_A,L_B,L,n}$	$V_{L_A,L_B,L,n}(30\ a_0)$
1	1	2	3*	1.9697(+0)	1.9715(+0)	2.0127(+0)	3.8551(-05)
1	2	3	4*	−2.8394(+0)	−2.8597(+0)	−3.0642(+0)	1.2127(-06)
1	3	4	5*	1.6637(+1)	1.6761(+1)	1.7103(+1)	1.7654(-07)
2	2	4	5*	−5.6953(+0)	−5.4312(+0)	−6.1080(+0)	5.5389(-08)
0	0	0	6	4.7270(+1)		4.6852(+1)	2.2986(-07)
1	4	5	6*	−5.4131(+1)	−5.5049(+1)	−5.7422(+1)	1.5274(-08)
0	2	2	6	1.2657(+1)		1.5681(+1)	1.2309(-08)
2	3	5	6*	3.6904(+1)	3.9347(+1)	4.2140(+1)	9.1458(-09)
0	1	1	7	−1.8433(+2)		−8.2153(+1)	9.9596(-09)
1	2	3	7	−3.4979(+2)		1.5651(+1)	5.5331(-09)
0	3	3	7	−1.0784(+2)		−7.9522(+1)	2.4971(-09)
3	3	6	7*	3.1701(+2)	3.3946(+2)	3.4622(+2)	2.0359(-09)
0	0	0	8	9.2546(+2)		1.1077(+3)	5.0003(-09)
0	2	2	8	3.9371(+3)		1.4208(+3)	4.2544(-09)
1	1	2	8	4.5792(+3)		−1.0618(+2)	3.6882(-09)
2	2	4	8	−4.4826(+3)		6.2384(+2)	1.6146(-09)
0	1	1	9	3.0500(+4)		−3.1644(+3)	1.8310(-09)
1	2	3	9	9.9936(+4)		2.2929(+3)	1.7565(-09)
1	2	1	9	−2.3093(+4)		−6.1280(+2)	6.2000(-10)
0	3	3	9	9.0400(+3)		−5.6295(+3)	2.3259(-10)

As an indication of the relative importance of the different $C_{L_A,L_B,L,n}$ coefficients, we explicitly give their contributions to the potential at $R = 30\ a_0$ (see Table 2.2). These contributions, $V_{L_A,L_B,L,n}(R)$, were calculated as follows:

$$V_{L_A,L_B,L,n}(R) = N_{L_A,L_B,L} \frac{|C^{fit}_{L_A,L_B,L,n}|}{R^n}, \tag{2.10}$$

where $N_{L_A,L_B,L} = [4\pi/(2L_A+1)(2L_B+1)(2L+1)]^{1/2}$ is the norm of the angular $A_{L_A,L_B,L}(\theta_A, \theta_B, \phi)$ functions. It is clear that the $n = 3$ dipole-dipole interaction dominates the potential by at least one order of magnitude, followed by the electrostatic dipole-quadrupole term. The main second order term is the isotropic $n = 6$ interaction, which, at 30 a_0, is still larger than the electrostatic $n = 5$ terms. The fact that the fitted $C_{1,1,2,3}$ and $C_{0,0,0,6}$ coefficients give the largest contributions in first and second order, respectively, indicates that the fit is not only numerical, but also physically meaningful. Thus, we may safely extrapolate the potential from 30 a_0 to larger R values.

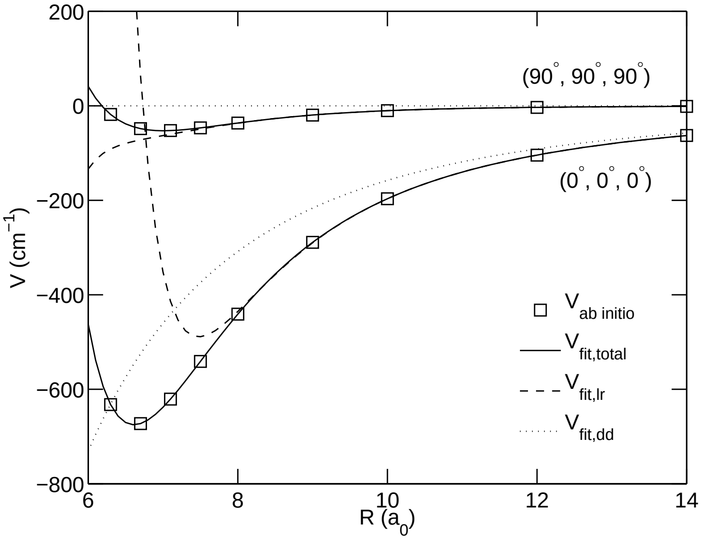

Figure 2.3: R-dependent quintet potential for two selected orientations $(\theta_A, \theta_B, \phi)$. The solid lines correspond to the total fitted potential, the dashed lines to the long-range potential, and the dotted lines to the long-range dipole-dipole interaction.

Figure 2.3 shows the R-dependence of the fitted RCCSD(T) potential for two specific orientations $(\theta_A, \theta_B, \phi)$. For the linear geometry, with $\theta_A = \theta_B = \phi = 0°$, the leading dipole-dipole interaction is maximally attractive, while for $\theta_A = \theta_B = \phi = 90°$ the dipole-dipole term is zero. It can be seen that the $C_{1,1,2,3}$ coefficient dominates the long-range potential beyond $R \approx 12$ a_0. Figure 2.3 also compares the total long-range expansion with the *ab initio* data, illustrating the region of validity of Eq. (2.7). It should be noted that, on the scale of the figure, the short-range expansion of Eq. (2.2) is indistinguishable from the total fitted potential of Eq. (2.9), and thus the short-range expansion is not explicitly shown. The long-range fit is very accurate for intermolecular distances larger than 8 a_0, which suggests that short-range (exchange and charge penetration) effects are only significant for $R \leq 8$ a_0. This also justifies our choice of switching the potential from the short-range to the long-range expansion between 8 and 12 a_0.

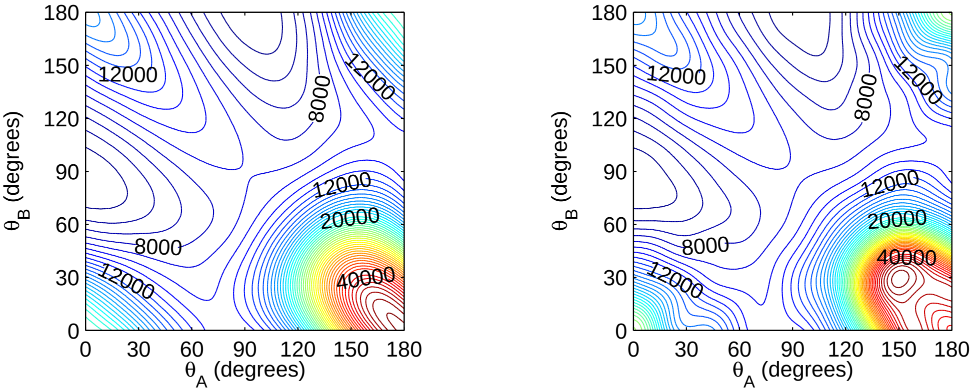

Figure 2.4: Cuts of the quintet potential (in cm^{-1}) for $R = 4.0\ a_0$ and $\phi = 0°$. The left panel shows the fit obtained in this work and the right panel shows the results of Ref. [90].

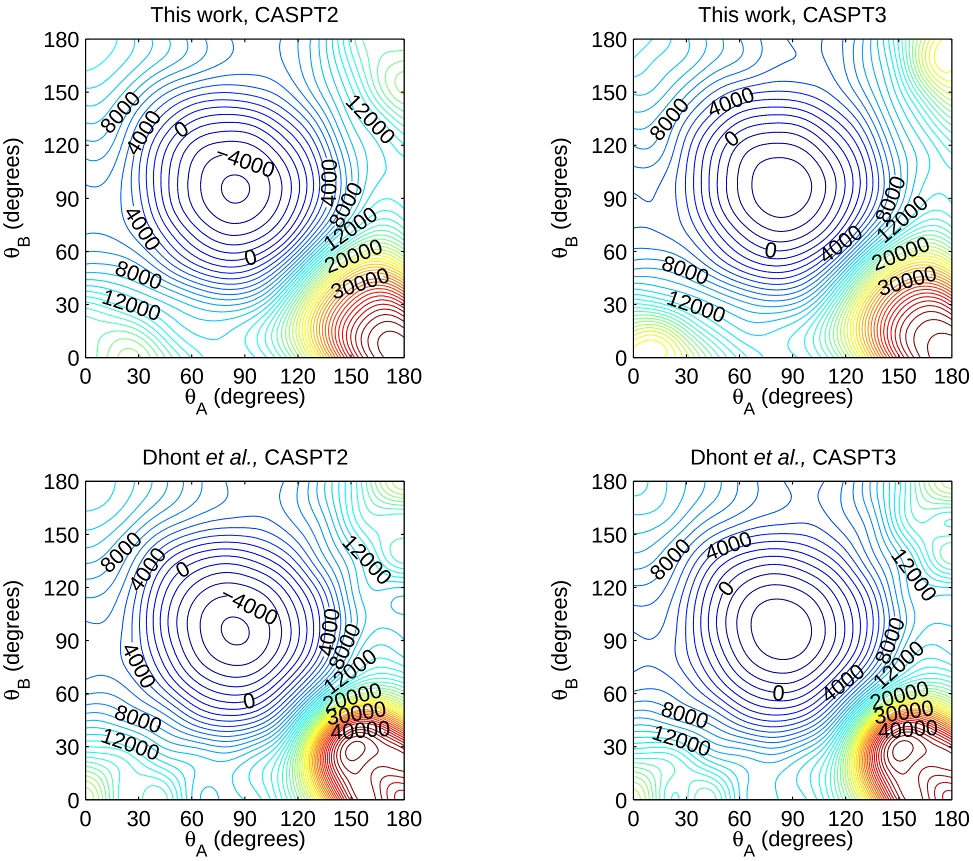

Figure 2.5: Cuts of the triplet potential (in cm^{-1}) for $R = 4.0\ a_0$ and $\phi = 0°$, calculated using Eq. (2.1). The upper panels correspond to the present work and the lower panels to the work of Dhont *et al.* [90].

2.4.2 Short-range potentials

Although the $S = 0$, 1, and 2 potentials obtained in this work are very similar to those reported by Dhont *et al.* [90], there are some notable differences at very short intermolecular distances. The differences are most pronounced at $R = 4.0\ a_0$, where the potentials exhibit the highest anisotropy. Figure 2.4 compares the two fit results for the quintet state as a function of θ_A and θ_B, with $R = 4.0\ a_0$ and $\phi = 0°$. Note that both surfaces were obtained from the same set of *ab initio* data. The fit of Ref. [90] shows more oscillatory behaviour than our present result, in particular near $(\theta_A, \theta_B) = (180°, 150°)$ and $(30°, 0°)$. Furthermore, the potential of Dhont *et al.* has a local maximum around $(150°, 30°)$ that is clearly unphysical in nature. Similar patterns are found for the triplet and singlet states, as can be seen in Figs. 2.5 and 2.6. The $S = 0$ and 1 potentials of Ref. [90] exhibit more pronounced oscillations and local maxima, indicating more unphysical behaviour. We therefore conclude that, in addition to the more accurate long-range potential, the fit of the short-range NH–NH potentials is also improved in the present work.

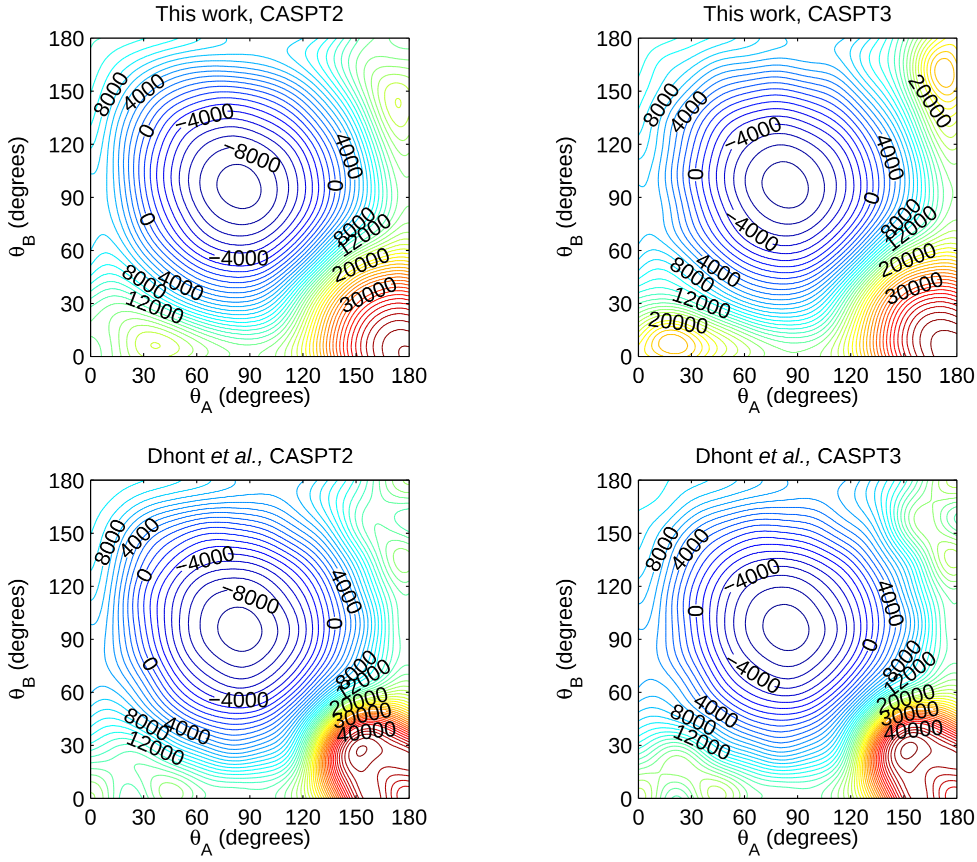

Figure 2.6: Cuts of the singlet potential (in cm^{-1}) for $R = 4.0\ a_0$ and $\phi = 0°$, calculated using Eq. (2.1). The upper panels correspond to the present work and the lower panels to the work of Dhont *et al.* [90].

2.5 Conclusions

We have constructed four-dimensional potential energy surfaces for the singlet, triplet, and quintet states of NH($^3\Sigma^-$) – NH($^3\Sigma^-$) based on high-level *ab initio* calculations. All potentials were fitted in terms of coupled spherical harmonics in the angular coordinates, and the long range was further expanded as a power series in $1/R$. Prior to fitting, the *ab initio* data were corrected for a size-consistency error of 0.5×10^{-6} E_h occurring at the RCCSD(T) level of theory. The fitted long-range coefficients were found to be in good agreement with the results obtained from first and second-order perturbation theory.

Appendix

In this Appendix, we describe how we optimized the quadrature weights w_i for the integration of Legendre polynomials $P_l(x)$ on a given grid of mutually distinct points x_i $(i = 1, \ldots, n)$:

$$\int_{-1}^{1} P_l(x)dx = 2\delta_{l,0} \approx \sum_{i=1}^{n} w_i P_l(x_i). \tag{2.11}$$

We define the optimization as a minimization of the sum of square residuals $|\boldsymbol{r}|$:

$$|\boldsymbol{r}| = |\boldsymbol{A}\boldsymbol{w} - \boldsymbol{b}|, \tag{2.12}$$

where $\boldsymbol{A}$ is an $(l_{max}+1) \times n$ matrix with elements $A_{li} = P_l(x_i)$ $(l = 0, \ldots, l_{max})$, $\boldsymbol{w}$ is a vector of length n containing the quadrature weights w_i, and $\boldsymbol{b}$ is a vector of length $l_{max}+1$ with elements $b_l = 2\delta_{l,0}$. In the case of an n-point Gauss-Legendre quadrature, x_i and w_i are chosen in such a way that the integration is exact, i.e., $|\boldsymbol{r}| = 0$, for all polynomials up to degree $l_{max} = 2n-1$. For arbitrary, mutually distinct points x_i, we may calculate the weights as $\boldsymbol{w} = \boldsymbol{A}^{-1}\boldsymbol{b}$, since $\boldsymbol{A}$ is regular for $l_{max} = n-1$ (see p. 145 of Ref. [94]). This results in a quadrature that is exact up to (at least) degree $n-1$. Instead of using a quadrature that is exact for $l_{max} = n-1$ and most likely unsuitable for higher degree polynomials, we choose a compromise quadrature that is reasonable for $l_{max} > n-1$ at the expense of not being exact for lower degree polynomials. This may be achieved by linear least squares minimization of $|\boldsymbol{r}|$. However, we prefer to use a quadrature that is exact for constant functions ($l = 0$), which requires a minimization of $|\boldsymbol{r}|$ with the constraint that $\sum_{i=1}^{n} w_i = 2$. For this purpose we take

$$\boldsymbol{w} = \boldsymbol{w}_0 + \boldsymbol{w}_\perp, \tag{2.13}$$

with $(\boldsymbol{w}_0)_i = 2/n$ for all $i = 1, \ldots, n$ and $\sum_{i=1}^{n} (\boldsymbol{w}_\perp)_i = 0$. This may be rewritten as $\boldsymbol{w}_0^T \boldsymbol{w}_\perp = 0$, with $\boldsymbol{w}_0^T$ denoting the transpose of $\boldsymbol{w}_0$. We can now expand $\boldsymbol{w}_\perp$ in an orthogonal basis $\{\boldsymbol{q}_i, i = 2, \ldots, n\}$ of vectors $\boldsymbol{q}_i$ that are perpendicular to $\boldsymbol{w}_0$:

$$\boldsymbol{w}_\perp = \sum_{i=2}^{n} \boldsymbol{q}_i c_i = \tilde{\boldsymbol{Q}}\boldsymbol{c}. \tag{2.14}$$

We observe that the first row of the matrix $\boldsymbol{A}$ is proportional to $\boldsymbol{w}_0$, and thus the vectors $\boldsymbol{q}_i$ can be generated by Gram-Schmidt QR-factorization of $\boldsymbol{A}^T$:

$$\boldsymbol{A}^T = \boldsymbol{Q}\boldsymbol{R}. \tag{2.15}$$

Here, $\boldsymbol{Q}$ is an $n \times n$ orthonormal matrix and $\boldsymbol{R}$ is an $n \times (l_{max} + 1)$ upper triangular matrix. The columns $i = 2, \ldots, n$ of $\boldsymbol{Q}$ form the matrix $\tilde{\boldsymbol{Q}}$ of Eq. (2.14). In order to find the expansion coefficients $\boldsymbol{c}$, we now remove the first row of $\boldsymbol{A}$ and the first element of $\boldsymbol{b}$, yielding the $(l_{max} \times n)$ matrix $\tilde{\boldsymbol{A}}$ and the null vector $\tilde{\boldsymbol{b}}$ of length l_{max}, respectively, and define the residual $\tilde{\boldsymbol{r}} = \tilde{\boldsymbol{A}}\boldsymbol{w}$. Substitution of Eq. (2.13) gives

$$|\tilde{\boldsymbol{r}}| = |\tilde{\boldsymbol{A}}\boldsymbol{w}_0 + \tilde{\boldsymbol{A}}\tilde{\boldsymbol{Q}}\boldsymbol{c}|, \tag{2.16}$$

which can be minimized in a standard least squares procedure to obtain the expansion coefficients $\boldsymbol{c}$. Finally, substitution of Eq. (2.14) into (2.13) gives the total optimal quadrature weights. In the present work, we have employed this method to generate optimal weights for the short-range quintet potential with $n = 11$ and $l_{max} = 16$.

Chapter 3

Scattering in field-free space

This chapter focuses on the calculation of elastic and inelastic spin-changing cross sections for cold and ultracold NH($X\,^3\Sigma^-$) + NH($X\,^3\Sigma^-$) collisions. The cross sections are obtained from full quantum scattering calculations on the *ab initio* quintet potential energy surface described in Chapter 2. Although we consider only collisions in zero field, we focus on the cross sections relevant for magnetic trapping experiments. It is shown that evaporative cooling of both fermionic ^{14}NH and bosonic ^{15}NH is likely to be successful for hyperfine states that allow s-wave collisions. The calculated cross sections are very sensitive to the details of the interaction potential, due to the presence of (quasi-)bound state resonances. The remaining inaccuracy of the *ab initio* potential energy surface therefore gives rise to an uncertainty in the numerical cross-section values. However, based on a sampling of the uncertainty range of the *ab initio* calculations, we conclude that the exact potential is likely to be such that the elastic-to-inelastic cross-section ratio is sufficiently large to achieve efficient evaporative cooling. This likelihood is only weakly dependent on the size of the channel basis set used in the scattering calculations.

3.1 Introduction

Knowledge of the elastic and inelastic collision dynamics is crucial to determine the feasibility of evaporative cooling. For NH–NH, we may use the interaction potentials of the previous chapter to calculate the relevant cross sections. As outlined in Sec. 1.4, a rigorous calculation of such scattering processes requires a full quantum coupled-channels method. In the case of NH–NH, however, the strong anisotropy of the interaction potentials and the open-shell nature of the monomers gives rise to a very large number of channels, making the calculation extremely challenging. In a recent study by Tscherbul *et al.* [87] on the iso-electronic $O_2(X\,^3\Sigma_g^-)$ – $O_2(X\,^3\Sigma_g^-)$ system, close-coupling calculations were performed that included up to 2526 channels, yielding cross sections converged to within 10%. These calculations were carried out in a fully decoupled channel basis to study collisions in the presence of an external magnetic field. It was noted, however, that the true O_2–O_2 interaction potential is likely to be more anisotropic than the potential used in their work, thus implying that even more channels would be needed. Other quantum scattering studies on O_2–O_2 include those by Avdeenkov and Bohn [111] and Pérez-Ríos *et al.* [112]. In the work of Avdeenkov and Bohn, field-free collisions were studied using a total angular momentum representation, thereby reducing the total number of channels to 836. The rotational basis-set size used in these calculations was, however, smaller than that used in Ref. [87]. Pérez-Ríos *et al.* also employed a total angular momentum basis, but the O_2 monomers were treated as closed-shell molecules. This allowed them to reduce the number of channels to 300.

To our knowledge, only one theoretical study has been reported for the NH–NH system. Kajita [89] employed the Born approximation, distorted-wave Born approximation, and a classical path method to calculate elastic and inelastic cross sections at energies ranging from 1 μK to 10 K, and found that evaporative cooling of NH is likely to be feasible. It must be noted, however, that only the electric dipole-dipole and magnetic dipole-dipole interactions were considered in these calculations.

The aim of the present work is to obtain cold and ultracold NH + NH collision cross sections from rigorous quantum scattering calculations on an accurate *ab initio* quintet potential energy surface. We include intramolecular spin-spin, spin-rotation, and intermolecular magnetic dipole-dipole coupling in the dynamics. In addition, we seek to address the issue of dealing with very large basis sets in order to converge the scattering results, a problem that is general for open-shell systems with relatively deep potential energy wells. For this purpose, we have employed a total angular momentum representation to perform the scattering calculations, assuming zero field. Collisions in a magnetic field are discussed in the next chapter. It will be shown that, within the uncertainty limits of the interaction potential, even an unconverged basis set can provide meaningful results.

This chapter is organized as follows. In Sec. 3.2, we discuss the scattering Hamiltonian and channel basis-set functions, followed by the details of the cross-section calculations. Results are presented in Sec. 3.3.1. In Secs. 3.3.2 and 3.3.3, we provide a comprehensive discussion on the accuracy of our calculated cross sections. Concluding remarks are given in Sec. 3.4.

3.2 Theory

3.2.1 Hamiltonian and channel basis functions

We consider the case of two colliding NH($^3\Sigma^-$) molecules in the absence of an external field and treat the monomers as rigid rotors. We use a space-fixed coordinate frame to describe the collision complex (see Fig. 2.1). The relevant Jacobi coordinates are the intermolecular vector $\boldsymbol{R}$ that connects the centers of mass of molecules A and B, and the polar angles $\omega_i = (\theta_i, \phi_i)$ of the two monomers ($i = A, B$). We will neglect hyperfine coupling and assume that both monomers are in their nuclear-spin stretched states $|I, M_I = I\rangle$, with $I = I_\mathrm{N} + I_\mathrm{H}$ denoting the maximum total nuclear spin and M_I its laboratory-frame projection. For fermionic ^{14}NH the maximum nuclear spin is $I = 3/2$ and for bosonic ^{15}NH we have $I = 1$.

The scattering Hamiltonian for NH–NH can be written as

$$\begin{aligned}\hat{H} &= -\frac{\hbar^2}{2\mu R}\frac{\partial^2}{\partial R^2}R + \frac{\hat{L}^2}{2\mu R^2} + \sum_{S,M_S} |S, M_S\rangle V_S(\boldsymbol{R}, \omega_A, \omega_B)\langle S, M_S| \\ &\quad + V_\mathrm{magn.dip}(\boldsymbol{R}, \hat{\boldsymbol{S}}_A, \hat{\boldsymbol{S}}_B) + \hat{H}_A + \hat{H}_B, \end{aligned} \tag{3.1}$$

where μ is the reduced mass of the complex, R is the length of the vector $\boldsymbol{R}$, $\hat{L}^2$ is the angular momentum operator associated with rotation of $\boldsymbol{R}$, $V_S(\boldsymbol{R}, \omega_A, \omega_B)$ is the potential energy surface for total spin S, M_S is the space-fixed projection of S, $V_\mathrm{magn.dip}(\boldsymbol{R}, \hat{\boldsymbol{S}}_A, \hat{\boldsymbol{S}}_B)$ is the intermolecular magnetic dipole interaction between the two triplet spins, and $\hat{H}_A$ and $\hat{H}_B$ are the Hamiltonians of the individual monomers. The magnetic dipole term is given by

$$V_\mathrm{magn.dip}(\boldsymbol{R}, \hat{\boldsymbol{S}}_A, \hat{\boldsymbol{S}}_B) = -\sqrt{6}g_S^2\mu_\mathrm{B}^2\frac{\alpha^2}{R^3}\sum_q(-1)^q C_{2,-q}(\Omega)[\hat{\boldsymbol{S}}_A \otimes \hat{\boldsymbol{S}}_B]^{(2)}_q, \tag{3.2}$$

where $g_S \approx 2.0023$ is the electron g-factor, μ_B is the Bohr magneton, α is the fine-structure constant, $C_{2,-q}$ is a Racah-normalized spherical harmonic, $\Omega = (\Theta, \Phi)$ describes the orientation of $\boldsymbol{R}$ in the space-fixed frame, and the factor in square brackets represents the tensorial product of the monomer spin operators $\hat{\boldsymbol{S}}_A$ and $\hat{\boldsymbol{S}}_B$. The monomer operators $\hat{H}_i$ each contain rotation, spin-rotation, and intramolecular spin-spin terms,

$$\hat{H}_i = B_0\hat{N}_i^2 + \gamma\hat{\boldsymbol{N}}_i \cdot \hat{\boldsymbol{S}}_i + \frac{2}{3}\sqrt{6}\lambda_\mathrm{SS}\sum_q(-1)^q C_{2,-q}(\omega_i)[\hat{\boldsymbol{S}}_i \otimes \hat{\boldsymbol{S}}_i]^{(2)}_q, \tag{3.3}$$

with $\hat{\boldsymbol{N}}_i$ denoting the rotational angular momentum operator of monomer i. For brevity, we will denote the intramolecular spin-spin operator as $\hat{V}_\mathrm{SS}^{(i)}$. The numerical values for the rotational, spin-rotation, and spin-spin constants are $B_0 = 16.343275$ cm^{-1}, $\gamma = -0.05486$ cm^{-1}, and $\lambda_\mathrm{SS} = 0.91989$ cm^{-1} for ^{14}NH [113], and, by scaling with the isotope mass (see e.g. p. 239 of Ref. [114]), we obtain $B_0 = 16.270340$ cm^{-1}, $\gamma = -0.05460$ cm^{-1}, and $\lambda_\mathrm{SS} = 0.91989$ cm^{-1} for ^{15}NH.

For the interaction potential $V_S(\boldsymbol{R}, \omega_A, \omega_B)$ we take the $S = 2$ *ab initio* surface described in Chapter 2. This spin state corresponds to the case where both molecules are in their magnetically trapped (spin-stretched) states. Although the potential is based on the Jacobi coordinates for ^{14}NH – ^{14}NH, we use the same surface for the ^{15}NH – ^{15}NH isotope. This approximation is very reasonable since the center of mass of ^{15}NH is shifted by only 0.008 a_0 with respect to that of ^{14}NH. We have verified that, at the equilibrium distance of the complex, this would give a maximum error of 2.2% in the ^{15}NH – ^{15}NH potential, which falls within the uncertainty range of the *ab initio* data. Following Ref. [115], we expand the quintet potential in terms of spherical harmonics $Y_{L,M}$ of degree L and order M,

$$V(\boldsymbol{R},\omega_A,\omega_B) = \sum_{L_A,L_B,L_{AB}} \upsilon_{L_A,L_B,L_{AB}}(R) A_{L_A,L_B,L_{AB}}(\Omega,\omega_A,\omega_B), \tag{3.4}$$

$$\begin{aligned} A_{L_A,L_B,L_{AB}}(\Omega,\omega_A,\omega_B) = & \sum_{M_A,M_B,M_{AB}} \langle L_A M_A L_B M_B | L_{AB} M_{AB}\rangle \\ & \times Y_{L_A,M_A}(\omega_A) Y_{L_B,M_B}(\omega_B) Y^{*}_{L_{AB},M_{AB}}(\Omega), \end{aligned} \tag{3.5}$$

where $\langle L_A M_A L_B M_B | L_{AB} M_{AB}\rangle$ is a Clebsch-Gordan coefficient and the superscript * denotes complex conjugation. The subscript $S = 2$ has been omitted for brevity. It should be noted that the angular functions of Eq. (3.5) differ by a factor of $\zeta = (-1)^{L_A - L_B}(4\pi)^{-3/2}(2L_{AB}+1)[(2L_A+1)(2L_B+1)]^{1/2}$ from the functions used in Eq. (2.2), i.e., the $\upsilon_{L_A,L_B,L_{AB}}(R)$ expansion coefficients of the previous chapter must be divided by ζ to obtain the potential in the form of Eq. (3.4).

In the absence of an external field, both the total angular momentum $\mathcal{J}$ and its space-fixed projection $\mathcal{M}$ are rigorously conserved. We therefore expand the wave function in a total angular momentum basis,

$$\begin{aligned} \Psi^{\mathcal{J},\mathcal{M}}(R,\Omega,\omega_A,\omega_B,\sigma_A,\sigma_B) = \frac{1}{R} & \sum_{N_A,N_B,N,S_A,S_B,S,J,L} \chi^{\mathcal{J},\mathcal{M}}_{N_A,N_B,N,S_A,S_B,S,J,L}(R) \\ & \times \psi^{\mathcal{J},\mathcal{M}}_{N_A,N_B,N,S_A,S_B,S,J,L}(\Omega,\omega_A,\omega_B,\sigma_A,\sigma_B), \end{aligned} \tag{3.6}$$

where σ_A and σ_B refer to the electronic spin coordinates of molecules A and B, respectively. Here N_A and N_B denote the rotational quantum numbers of the two monomers, N is the coupled rotational quantum number of the complex, S_A and S_B are the monomer spin quantum numbers, which are coupled into total spin S, J is the angular momentum quantum number arising from the coupling of N and S, and L denotes the partial-wave angular momentum. The coupled angular momentum basis functions are defined as

$$\begin{aligned} & \psi^{\mathcal{J},\mathcal{M}}_{N_A,N_B,N,S_A,S_B,S,J,L}(\Omega,\omega_A,\omega_B,\sigma_A,\sigma_B) = \\ & \quad \sum_{M_J,M_L} \sum_{M_N,M_S} \sum_{M_{S_A},M_{S_B}} \sum_{M_{N_A},M_{N_B}} Y_{N_A,M_{N_A}}(\omega_A) Y_{N_B,M_{N_B}}(\omega_B) Y_{L,M_L}(\Omega) \\ & \quad \times \tau_{S_A,M_{S_A}}(\sigma_A) \tau_{S_B,M_{S_B}}(\sigma_B) \langle N_A M_{N_A} N_B M_{N_B} | N M_N\rangle \langle S_A M_{S_A} S_B M_{S_B} | S M_S\rangle \\ & \quad \times \langle N M_N S M_S | J M_J\rangle \langle J M_J L M_L | \mathcal{J}\mathcal{M}\rangle, \end{aligned} \tag{3.7}$$

where $\tau_{S_A,M_{S_A}}$ and $\tau_{S_B,M_{S_B}}$ are spinor wave functions. Here the quantum numbers M_{N_i}, M_{S_i}, M_N, M_S, M_J, and M_L denote the projections of N_i, S_i, N, S, J, and L onto the magnetic-field axis. We will restrict the basis such that N_A and N_B range from 0 to $N_{\max}$ and L from 0 to $L_{\max}$. Note that the scattering calculations in this basis may also be performed for a single dimer spin state S. As detailed in Section 3.3.2, we will exploit this feature to investigate the validity of describing all three dimer spin states by the $S = 2$ potential energy surface.

Since target and projectile are identical, we can symmetrize the wave function with respect to the permutation operator $\hat{P}_{AB}$. This yields the following normalized basis functions,

$$\begin{aligned}\phi^{\eta,\mathcal{J},\mathcal{M}}_{N_A,N_B,N,S_A,S_B,S,J,L} = {} & \frac{1}{[2(1+\delta_{N_A N_B}\delta_{S_A S_B})]^{1/2}}\big[\psi^{\mathcal{J},\mathcal{M}}_{N_A,N_B,N,S_A,S_B,S,J,L} \\ & + \eta(-1)^{L+N_A+N_B-N+S_A+S_B-S}\psi^{\mathcal{J},\mathcal{M}}_{N_B,N_A,N,S_B,S_A,S,J,L}\big]. \end{aligned} \tag{3.8}$$

Here $\eta = +1$ corresponds to composite bosons and $\eta = -1$ to composite fermions, assuming that the molecules are in their nuclear-spin stretched states. To obtain a linearly independent basis, the index pair (N_A, N_B) must be restricted such that $N_A \geq N_B$ [115]. Finally, the basis functions of Eq. (3.8) are also eigenfunctions of the inversion operator, with eigenvalues $\epsilon = (-1)^{N_A+N_B+L}$. Thus, the Hamiltonian in the symmetry-adapted basis set consists of four blocks, each block labeled by η and the parity ϵ. It must be noted, however, that the wave function of Eq. (3.8) vanishes for $(\eta = +1, \epsilon = -1)$ and $(\eta = -1, \epsilon = +1)$ if the molecules are in the magnetically trapped ground state with $N_A = N_B = N = 0$ and $S = 2$. We therefore only need to consider the parity case $\epsilon = +1$ for $\eta = +1$ and $\epsilon = -1$ for $\eta = -1$.

The matrix elements of the scattering Hamiltonian in the symmetry-adapted basis [Eq. (3.8)] can be readily obtained from the matrix elements in the 'primitive' basis $\psi^{\mathcal{J},\mathcal{M}}_{N_A,N_B,N,S_A,S_B,S,J,L}$. For the angular functions of the potential we have

$$\begin{aligned}&\langle\psi^{\mathcal{J},\mathcal{M}}_{N_A,N_B,N,S_A,S_B,S,J,L}|A_{L_A,L_B,L_{AB}}|\psi^{\mathcal{J},\mathcal{M}}_{N'_A,N'_B,N',S_A,S_B,S',J',L'}\rangle = \\ &\quad \delta_{SS'}\left(\frac{1}{4\pi}\right)^{3/2}(-1)^{N_A+N_B+N+S+L_{AB}+2J'+\mathcal{J}} \\ &\quad \times [L_{AB}]\sqrt{[L_A][L_B][N_A][N'_A][N_B][N'_B][N][N'][L][L'][J][J']} \\ &\quad \times \begin{pmatrix} N_A & L_A & N'_A \\ 0 & 0 & 0 \end{pmatrix}\begin{pmatrix} N_B & L_B & N'_B \\ 0 & 0 & 0 \end{pmatrix}\begin{pmatrix} L & L_{AB} & L' \\ 0 & 0 & 0 \end{pmatrix} \\ &\quad \times \begin{Bmatrix} J & J' & L_{AB} \\ L' & L & \mathcal{J} \end{Bmatrix}\begin{Bmatrix} N' & N & L_{AB} \\ J & J' & S \end{Bmatrix}\begin{Bmatrix} N_A & N'_A & L_A \\ N_B & N'_B & L_B \\ N & N' & L_{AB} \end{Bmatrix}, \end{aligned} \tag{3.9}$$

with the factors in large round brackets denoting Wigner $3j$ symbols, the factors in curly brackets denoting $6j$ and $9j$ symbols, and $[Q] = (2Q + 1)$. The intermolecular magnetic dipole term is given by

$$\begin{aligned}
&\langle\psi^{\mathcal{J},\mathcal{M}}_{N_A,N_B,N,S_A,S_B,S,J,L}|V_{\text{magn.dip}}|\psi^{\mathcal{J},\mathcal{M}}_{N'_A,N'_B,N',S_A,S_B,S',J',L'}\rangle = \\
&\quad -\delta_{N_A N'_A}\delta_{N_B N'_B}\delta_{NN'}\sqrt{30}g_S^2\mu_{\text{B}}^2\frac{\alpha^2}{R^3}(-1)^{N+S'+J+J'+\mathcal{J}} \\
&\quad \times\sqrt{S_A(S_A+1)S_B(S_B+1)[S_A][S_B][S][S'][J][J'][L][L']} \\
&\quad \times\begin{pmatrix} L & 2 & L' \\ 0 & 0 & 0 \end{pmatrix}\begin{Bmatrix} J & J' & 2 \\ L' & L & \mathcal{J} \end{Bmatrix}\begin{Bmatrix} J' & J & 2 \\ S & S' & N \end{Bmatrix}\begin{Bmatrix} S_A & S_A & 1 \\ S_B & S_B & 1 \\ S & S' & 2 \end{Bmatrix}.
\end{aligned}\tag{3.10}$$

The rotation operators for the two monomers ($i = A, B$) are completely diagonal in the angular basis,

$$\begin{aligned}
&\langle\psi^{\mathcal{J},\mathcal{M}}_{N_A,N_B,N,S_A,S_B,S,J,L}|B_0\hat{N}_i^2|\psi^{\mathcal{J},\mathcal{M}}_{N'_A,N'_B,N',S_A,S_B,S',J',L'}\rangle = \\
&\qquad \delta_{N_A N'_A}\delta_{N_B N'_B}\delta_{NN'}\delta_{SS'}\delta_{JJ'}\delta_{LL'}B_0N_i(N_i+1).
\end{aligned}\tag{3.11}$$

For the spin-rotation coupling terms we find

$$\begin{aligned}
&\langle\psi^{\mathcal{J},\mathcal{M}}_{N_A,N_B,N,S_A,S_B,S,J,L}|\gamma\hat{\boldsymbol{N}}_A\cdot\hat{\boldsymbol{S}}_A|\psi^{\mathcal{J},\mathcal{M}}_{N'_A,N'_B,N',S_A,S_B,S',J',L'}\rangle = \\
&\quad \delta_{N_A N'_A}\delta_{N_B N'_B}\delta_{JJ'}\delta_{LL'}\gamma(-1)^{N_A+N_B+S_A+S_B+S+S'+J} \\
&\quad \times\sqrt{N_A(N_A+1)S_A(S_A+1)[N_A][S_A][N][N'][S][S']} \\
&\quad \times\begin{Bmatrix} N_A & N_A & 1 \\ N & N' & N_B \end{Bmatrix}\begin{Bmatrix} S_A & S_A & 1 \\ S & S' & S_B \end{Bmatrix}\begin{Bmatrix} N & N' & 1 \\ S' & S & J \end{Bmatrix},
\end{aligned}\tag{3.12}$$

$$\begin{aligned}
&\langle\psi^{\mathcal{J},\mathcal{M}}_{N_A,N_B,N,S_A,S_B,S,J,L}|\gamma\hat{\boldsymbol{N}}_B\cdot\hat{\boldsymbol{S}}_B|\psi^{\mathcal{J},\mathcal{M}}_{N'_A,N'_B,N',S_A,S_B,S',J',L'}\rangle = \\
&\quad \delta_{N_A N'_A}\delta_{N_B N'_B}\delta_{JJ'}\delta_{LL'}\gamma(-1)^{N_A+N_B+N+N'+S_A+S_B+J} \\
&\quad \times\sqrt{N_B(N_B+1)S_B(S_B+1)[N_B][S_B][N][N'][S][S']} \\
&\quad \times\begin{Bmatrix} N' & N & 1 \\ N_B & N_B & N_A \end{Bmatrix}\begin{Bmatrix} S' & S & 1 \\ S_B & S_B & S_A \end{Bmatrix}\begin{Bmatrix} N & N' & 1 \\ S' & S & J \end{Bmatrix},
\end{aligned}\tag{3.13}$$

and, finally, for the intramolecular spin-spin operators $\hat{V}_{\text{SS}}^{(i)}$ we have

$$\begin{aligned}
&\langle\psi^{\mathcal{J},\mathcal{M}}_{N_A,N_B,N,S_A,S_B,S,J,L}|\hat{V}_{\text{SS}}^{(A)}|\psi^{\mathcal{J},\mathcal{M}}_{N'_A,N'_B,N',S_A,S_B,S',J',L'}\rangle = \\
&\quad \delta_{N_B N'_B}\delta_{JJ'}\delta_{LL'}\frac{2}{3}\sqrt{30}\lambda_{\text{SS}}(-1)^{N_B+S_A+S_B+S+S'+J}S_A(S_A+1)[S_A] \\
&\quad \times\sqrt{[N_A][N'_A][N][N'][S][S']}\begin{pmatrix} N_A & 2 & N'_A \\ 0 & 0 & 0 \end{pmatrix}\begin{Bmatrix} N'_A & N_A & 2 \\ N & N' & N_B \end{Bmatrix} \\
&\quad \times\begin{Bmatrix} S_A & S_A & 1 \\ 1 & 2 & S_A \end{Bmatrix}\begin{Bmatrix} S_A & S_A & 2 \\ S & S' & S_B \end{Bmatrix}\begin{Bmatrix} N & N' & 2 \\ S' & S & J \end{Bmatrix},
\end{aligned}\tag{3.14}$$

$$\begin{aligned}
&\langle \psi^{\mathcal{J},\mathcal{M}}_{N_A,N_B,N,S_A,S_B,S,J,L} | \hat{V}^{(B)}_{\rm SS} | \psi^{\mathcal{J},\mathcal{M}}_{N'_A,N'_B,N',S_A,S_B,S',J',L'} \rangle = \\
&\quad \delta_{N_A N'_A} \delta_{JJ'} \delta_{LL'} \frac{2}{3} \sqrt{30} \lambda_{\rm SS} (-1)^{N_A+N_B+N'_B+N+N'+S_A+S_B+J} S_B(S_B+1)[S_B] \\
&\quad \times \sqrt{[N_B][N'_B][N][N'][S][S']} \begin{pmatrix} N_B & 2 & N'_B \\ 0 & 0 & 0 \end{pmatrix} \begin{Bmatrix} N' & N & 2 \\ N_B & N'_B & N_A \end{Bmatrix} \\
&\quad \times \begin{Bmatrix} S_B & S_B & 1 \\ 1 & 2 & S_B \end{Bmatrix} \begin{Bmatrix} S' & S & 2 \\ S_B & S_B & S_A \end{Bmatrix} \begin{Bmatrix} N & N' & 2 \\ S' & S & J \end{Bmatrix}.
\end{aligned} \tag{3.15}$$

3.2.2 S-matrices and cross sections

The close-coupling equations are solved for each $\mathcal{J}$ and each symmetry type (η, ϵ) using the hybrid log-derivative method of Alexander and Manolopoulos [80]. This algorithm uses a fixed-step-size log-derivative propagator in the short range and a variable-step-size Airy propagator in the long range. The solutions are then matched to asymptotic boundary conditions to obtain the scattering S-matrices. Since we consider only the field-free case, the results are independent of the total angular momentum projection $\mathcal{M}$.

Although we assume zero magnetic field in our calculations, we are ultimately interested in the elastic and inelastic spin-changing cross sections for magnetically trapped NH. It is therefore necessary to transform the S-matrices to a channel product eigenbasis of the form $|(\bar{N}_A, S_A)J_A, M_{J_A}\rangle |(\bar{N}_B, S_B)J_B, M_{J_B}\rangle |L, M_L\rangle$, where J_i and M_{J_i} arise from the angular momentum coupling of $\bar{N}_i$ and S_i. Here we have used the notation $\bar{N}_i$ instead of N_i, because N_i is strictly not a good quantum number. This is due to the intramolecular spin-spin coupling, which mixes states with N_i and $N_i \pm 2$. However, the mixing is quite weak and $\bar{N}_i$ corresponds almost exactly to N_i. A symmetry-adapted version of the channel eigenbasis is given by

$$\begin{aligned}
\phi^{\eta}_{\bar{N}_A,S_A,J_A,M_{J_A},\bar{N}_B,S_B,J_B,M_{J_B},L,M_L} &= \frac{1}{[2(1+\delta_{\bar{N}_A\bar{N}_B}\delta_{S_AS_B}\delta_{J_AJ_B}\delta_{M_{J_A}M_{J_B}})]^{1/2}} \\
&\quad \times \big[|(\bar{N}_A, S_A)J_A, M_{J_A}\rangle |(\bar{N}_B, S_B)J_B, M_{J_B}\rangle |L, M_L\rangle \\
&\quad \times + \eta(-1)^L |(\bar{N}_B, S_B)J_B, M_{J_B}\rangle |(\bar{N}_A, S_A)J_A, M_{J_A}\rangle |L, M_L\rangle \big].
\end{aligned} \tag{3.16}$$

It should be noted that the total angular momentum $\mathcal{J}$ is not a good quantum number here, but its laboratory-frame projection $\mathcal{M} = M_{J_A} + M_{J_B} + M_L$ is conserved.

The basis transformation from Eq. (3.8) to Eq. (3.16) cannot be performed analytically, because N_i, N, and S are only approximately good quantum numbers. We have therefore developed a numerical scheme in which the channel eigenfunctions of Eq. (3.16) are obtained as the simultaneous eigenvectors of the operators $\{\hat{L}^2, \hat{H}_A + \hat{H}_B, \hat{J}_{z_A} + \hat{J}_{z_B}, \hat{J}^2_{z_A} + \hat{J}^2_{z_B}\}$. Note that these operators all commute with each other and with $\hat{P}_{AB}$. The numerical procedure works as follows. We start by diagonalizing the first operator, e.g. the matrix representation of the $\hat{L}^2$ operator, constructed in the basis of Eq. (3.8). In each degenerate subspace of $\hat{L}^2$, we set up the matrix of the next operator and diagonalize it. This process is repeated for the remaining operators until all eigenvectors are unique. We note that the operator $\hat{J}^2_{z_A}+\hat{J}^2_{z_B}$ is only required to distinguish between states with coincidental degeneracies in $M_{J_A}+M_{J_B}$, e.g. the states $|\phi^{\eta}_{0,1,1,0,0,1,1,0,0,0}\rangle$ with $M_{J_A}=M_{J_B}=0$ and $|\phi^{\eta}_{0,1,1,1,0,1,1,-1,0,0}\rangle$ with $M_{J_A}=1, M_{J_B}=-1$. Any remaining degeneracies arising from $\hat{H}_A+\hat{H}_B$ may be lifted by diagonalizing the operator $\hat{H}^2_A+\hat{H}^2_B$, but such degeneracies occur only for higher energies. In the cold and ultracold regime, these higher-energy channels are closed and the eigenvalues of $\hat{L}^2$, $\hat{H}_A+\hat{H}_B$, $\hat{J}_{z_A}+\hat{J}_{z_B}$, and $\hat{J}^2_{z_A}+\hat{J}^2_{z_B}$ are sufficient to identify all relevant quantum numbers. It must be noted that, since $\hat{J}_{z_A}$ and $\hat{J}_{z_B}$ do not separately commute with $\hat{P}_{AB}$, the matrices of $\hat{J}_{z_A}+\hat{J}_{z_B}$ and $\hat{J}^2_{z_A}+\hat{J}^2_{z_B}$ are not trivially constructed in the basis of Eq. (3.8). We obtained these matrices by first evaluating the $\hat{J}_{z_i}$ and $\hat{J}^2_{z_i}$ operators in a fully decoupled basis of the form $|N_A, M_{N_A}, S_A, M_{S_A}, N_B, M_{N_B}, S_B, M_{S_B}, L, M_L\rangle$. Both $\hat{J}_{z_i}$ and $\hat{J}^2_{z_i}$ are diagonal in this basis, with diagonal elements $M_{J_i}=M_{N_i}+M_{S_i}$ and $M^2_{J_i}$, respectively. We subsequently performed an analytical transformation to the coupled basis of Eq. (3.7) using the appropriate Clebsch-Gordan coefficients. Finally, we used a rectangular transformation matrix for $\hat{J}_{z_A}+\hat{J}_{z_B}$ and $\hat{J}^2_{z_A}+\hat{J}^2_{z_B}$ to account for the symmetry adaptation, i.e. to transform the matrices to the basis of Eq. (3.8).

The evaporative cooling rate for cold magnetically trapped NH molecules, with quantum numbers $\bar{N}_A=\bar{N}_B=0$, $J_A=J_B=1$, and $M_{J_A}=M_{J_B}=1$, is determined by the ratio between elastic and M_J-changing cross sections. The cross-section expression for indistinguishable molecules at total energy E is [87]

$$\sigma^{\eta}_{\gamma_A\gamma_B\to\gamma'_A\gamma'_B}(E)=\frac{\pi(1+\delta_{\gamma_A\gamma_B})}{k^2_{\gamma_A\gamma_B}}\sum_{L,M_L}\sum_{L',M'_L}\left|T^{\eta}_{\gamma_A\gamma_B LM_L;\gamma'_A\gamma'_B L'M'_L}(E)\right|^2, \tag{3.17}$$

where we have introduced the shorthand notation $\gamma_A\gamma_B$ to label the symmetrized monomer states, i.e. $\phi^{\eta}_{\bar{N}_A,S_A,J_A,M_{J_A},\bar{N}_B,S_B,J_B,M_{J_B},L,M_L}\equiv|\gamma_A\gamma_B\rangle|LM_L\rangle$, and $k_{\gamma_A\gamma_B}$ is the length of the wavevector for the initial collision channel $|\gamma_A\gamma_B\rangle$. The T-matrix elements are defined in terms of the transformed S-matrix elements as $T^{\eta}_{\gamma_A\gamma_B LM_L;\gamma'_A\gamma'_B L'M'_L}=\delta_{\gamma_A\gamma'_A}\delta_{\gamma_B\gamma'_B}\delta_{LL'}\delta_{M_LM'_L}-S^{\eta}_{\gamma_A\gamma_B LM_L;\gamma'_A\gamma'_B L'M'_L}$. Finally, we note that the summations over M_L and M'_L in Eq. (3.17) may also be understood as a sum over all possible $\mathcal{M}$ values, since $\mathcal{M}=M_{J_A}+M_{J_B}+M_L=M'_{J_A}+M'_{J_B}+M'_L$.

3.2.3 Computational details

The scattering calculations were performed using a modified version of the MOLSCAT package [116, 117] in which the coupled basis set of Eq. (3.6) was implemented. The radial grid ranged from 4.5 to 500 a_0, with the Airy propagation starting at 15 a_0. The step size for the log-derivative propagator was 0.02 a_0. The basis set included all functions up to $N_A=N_B=5$ and $L=6$. The expansion of the quintet potential was truncated at $L_A=L_B=6$. As mentioned in Section 3.2.1, the chemically reactive singlet and triplet interaction potentials were excluded from the calculations, and were replaced by the non-reactive $S = 2$ surface. Thus, we assumed that all three spin states are described by the same potential energy surface. In order to study the role of the $S = 0$ and 1 states under this assumption, we also performed scattering calculations for the quintet state only.

At each collision energy, the scattering S-matrices were accumulated for all relevant $\mathcal{J}$ values and subsequently transformed to the channel eigenbasis of Eq. (3.16) for all possible $\mathcal{M}$ values. The basis transformation was carried out in Matlab [118]. The total elastic and inelastic cross sections were then obtained using Eq. (3.17).

3.3 Results and discussion

Before we discuss the calculated cross sections and the prospects for evaporative cooling, let us first define the critical elastic-to-inelastic collision ratio needed for efficient second-stage cooling. A Monte Carlo study on cesium atoms indicated that the ratio between elastic and inelastic collision rates should be greater than 150 [54]. Although evaporative cooling of NH might also work with a lower ratio, we will assume that 150 is also the minimum required value for NH + NH collisions.

3.3.1 Cross sections

The elastic and M_J-changing cross sections for magnetically trapped ^{14}NH and ^{15}NH are shown in Fig. 3.1. At low collision energies, the cross sections are dominated by incoming s-waves for bosonic ^{15}NH and by p-waves for fermionic ^{14}NH. The observed energy dependence is consistent with Wigner's threshold law for isoergic processes [119, 120]:

$$\sigma \propto E^{L+L'}, \tag{3.18}$$

where L and L' denote the partial waves in the incoming and outgoing channels, respectively. For elastic ^{15}NH + ^{15}NH collisions, we have $L = L' = 0$ and the cross section is constant as a function of E. For inelastic collisions, the change in M_{J_A} or M_{J_B} must be accompanied by a change in the M_L quantum number, which follows from the conservation of $\mathcal{M}$. Since the parity $(-1)^{N_A+N_B+L}$ is also rigorously conserved, it is easily verified [see Eq. (3.8)] that the dominant inelastic cross section for ^{15}NH ($L = 0$) corresponds to the $L' = 2$ outgoing channel, and consequently behaves as E^2. For fermionic ^{14}NH + ^{14}NH collisions, both the elastic and inelastic channels are dominated by $L = L' = 1$ [see Eq. (3.8)], yielding the observed E^2 behaviour. We also point out that, in the presence of a magnetic field, all inelastic transitions would be exothermic and the corresponding cross section would behave as $E^{L-1/2}$ [119]. This leads to a different elastic-to-inelastic collision ratio than in the field-free case. It will be shown in the next chapter that the ratio for ^{15}NH + ^{15}NH collisions is still very favorable when the magnetic field is explicitly included.

We find that ^{15}NH is more suitable for evaporative cooling than ^{14}NH, in agreement with the findings of Kajita [89]. More specifically, we see in Fig. 3.1 that the elastic-

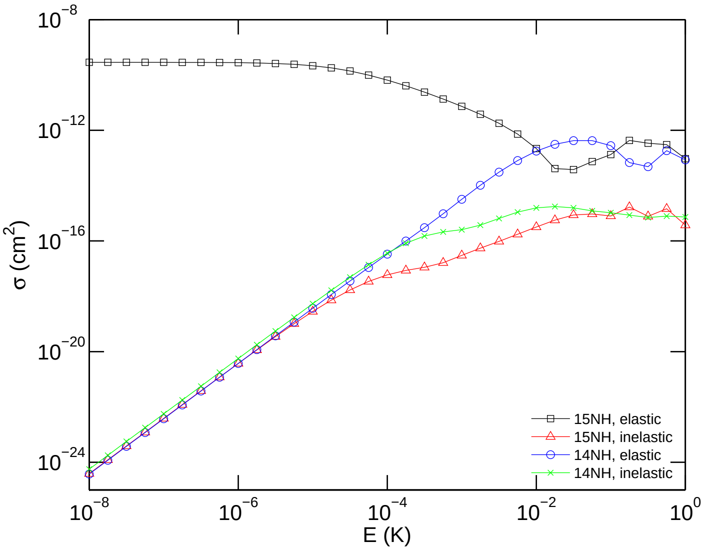

Figure 3.1: Elastic and inelastic M_J-changing cross sections for ^{14}NH + ^{14}NH and ^{15}NH + ^{15}NH collisions, assuming that all molecules are in their magnetically trappable and nuclear-spin stretched state.

to-inelastic ratio for ^{15}NH + ^{15}NH far exceeds the critical value of 150 for all energies below $E \approx 10^{-2}$ K, while for ^{14}NH + ^{14}NH the ratio is orders of magnitude smaller and is close to unity at collision energies below 10^{-4} K. This result is essentially a consequence of the Pauli principle, which forbids s-wave scattering for ^{14}NH + ^{14}NH. We emphasize that our calculations were performed under the assumption that both molecules are in their nuclear-spin stretched states, giving rise to a symmetric nuclear-spin wave function. This leads to the restriction that $\eta = +1$ ($\epsilon = +1$) for ^{15}NH and $\eta = -1$ ($\epsilon = -1$) for ^{14}NH. If, however, the two monomers were in *different* nuclear-spin states, the corresponding wave function may also be antisymmetric under exchange and both values of η would be allowed. In that case, the total cross section is given by a weighted sum over the cross sections σ^{+1} and σ^{-1},

$$\sigma_{\gamma_A\gamma_B\to\gamma'_A\gamma'_B}(E) = W^+\sigma^{+1}_{\gamma_A\gamma_B\to\gamma'_A\gamma'_B}(E) + W^-\sigma^{-1}_{\gamma_A\gamma_B\to\gamma'_A\gamma'_B}(E), \tag{3.19}$$

with W^+ and W^- denoting the relative spin-statistical weights. The weights are $W^+ = 5/12$ and $W^- = 7/12$ for fermionic ^{14}NH and 3/4 and 1/4 for bosonic ^{15}NH. Figure 3.2 shows the results for ^{14}NH – ^{14}NH, assuming a mixture of different nuclear-spin states (neglecting the mixing of M_S due to hyperfine coupling). The inclusion of even-L partial waves ($\eta = +1$) strongly enhances the efficiency of evaporative cooling for ^{14}NH, in particular due to the s-wave elastic contribution. For ^{15}NH – ^{15}NH, the addition of odd-L partial wave contributions ($\eta = -1$) will probably lead to a slightly lower elastic-to-inelastic ratio. This is because the odd-L elastic cross section, which vanishes as E^2, is almost negligible compared to the s-wave elastic cross section in the ultracold limit. The odd-L inelastic contribution, on the other hand, exhibits the same threshold behaviour as the even-L inelastic cross section, and could easily increase the total inelastic loss by a factor of ~ 2. Hence we conclude that, in order to achieve efficient evaporative cooling, bosonic ^{15}NH should be prepared in a single nuclear-spin state, while for ^{14}NH the molecules should be in a mixture of hyperfine states.

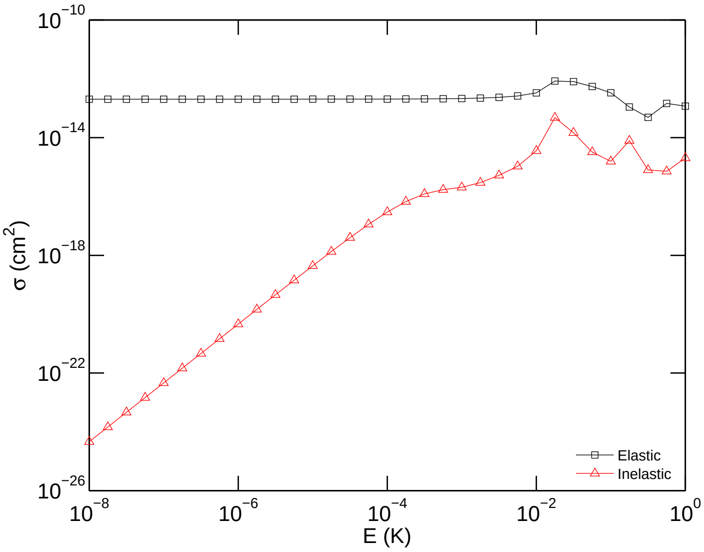

Figure 3.2: Elastic and inelastic M_J-changing cross sections for magnetically trapped ^{14}NH, assuming a statistical mixture of nuclear-spin states.

Aside from symmetry arguments, the difference between ^{15}NH – ^{15}NH and ^{14}NH – ^{14}NH is relatively small. The rotational and spin-rotation constants differ by only 0.45% and the reduced masses of the collision complex are 6.6% different. Since ^{15}NH is more advantageous for evaporative cooling, we will only consider collisions between ^{15}NH molecules in the remainder of this work. Again it will be assumed that the monomers are in identical hyperfine states, so that only the $\eta = +1$ ($\epsilon = +1$) symmetry case needs to be examined.

State-to-state cross sections for magnetically trapped ^{15}NH ($M_{J_A} = 1, M_{J_B} = 1$) are shown in Fig. 3.3. We find that transitions to the states with $|M_{J_A} = 1, M_{J_B} = 0\rangle$, $|M_{J_A} = 1, M_{J_B} = -1\rangle$, and $|M_{J_A} = 0, M_{J_B} = 0\rangle$ are dominant in the ultracold regime. It can also be seen that these cross sections follow an E^2 dependence below $\sim 10^{-4}$ K. The inelastic cross sections for $|M_{J_A} = 0, M_{J_B} = -1\rangle$ and $|M_{J_A} = -1, M_{J_B} = -1\rangle$ exhibit E^4 behaviour at low collision energies. These results are consistent with the threshold laws of Krems and Dalgarno for collisional reorientation of angular momentum in the absence of an external field [120]. Although these laws were derived for collisions of paramagnetic species with structureless targets, they also apply to ^{15}NH + ^{15}NH collisions:

$$\sigma_{J,M_J \to J,M_J \pm \Delta M_J} \propto E^{\Delta M_J} \tag{3.20}$$

if ΔM_J is even and

$$\sigma_{J,M_J \to J,M_J \pm \Delta M_J} \propto E^{\Delta M_J + 1} \tag{3.21}$$

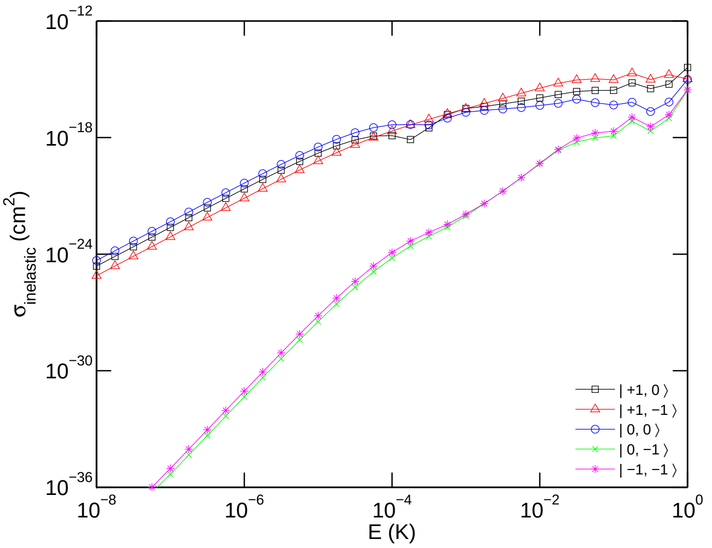

Figure 3.3: State-to-state inelastic cross sections for magnetically trapped ^{15}NH as a function of collision energy. The final states are labeled by $|M_{J_A}, M_{J_B}\rangle$.

if ΔM_J is odd. Here ΔM_J is defined as the change in $M_{J_A} + M_{J_B}$. It also follows from Eq. (3.20) that the elastic cross section ($\Delta M_J = 0$) is constant at low energies, in agreement with Eq. (3.18).

3.3.2 Contributions from singlet and triplet states

Throughout this work, we have assumed that all three spin states of the NH–NH complex are described by a single non-reactive potential energy surface, namely the $S = 2$ surface. The $S = 2$ state corresponds to the case where both monomers are magnetically trapped, and is therefore the most relevant spin state in our present study. It is, however, not *a priori* clear how the $S = 0$ and 1 states can influence the trap loss probability, and how well they can be described by the quintet surface.

We must first point out that, even at infinite separation, S is strictly not a good quantum number due to the intramolecular spin-spin coupling. However, the coupling between different spin states is relatively weak and we may therefore treat S as nearly exact. Specifically, for a collision complex of two rotational ground state molecules in their nuclear-spin stretched states, the initial state with $M_{J_A} = M_{J_B} = 1$ corresponds almost exclusively (99.98%) to the quintet state.

In order to investigate the contributions from the $S = 0$ and 1 states, we have performed scattering calculations with all singlet and triplet functions removed from the basis set. The results are shown in Fig. 3.4 as a function of energy. The cross sections for the full basis set, i.e. with all three spin states included, are also plotted for comparison. It can be seen that exclusion of the $S = 0$ and 1 states has a rather small effect on the cross section, suggesting that most of the trap loss takes place within the quintet state. Thus, the singlet and triplet states play a minor role in the collision dynamics when described by the non-reactive $S = 2$ potential.

If the $S = 0$ and 1 states were described by their true, reactive surfaces, any transition to the singlet or triplet state would be expected to lead to chemical reaction and consequent trap loss. In that case, however, the potentials are no longer degenerate at short range and the probability for hopping from the quintet surface to another state is most probably *decreased* due to the energy gap law. That is, inclusion of the reactive $S = 0$ and 1 surfaces will probably not lead to a larger inelastic cross section for nuclear-spin stretched states, and our assumption of including only the non-reactive $S = 2$ surface is very reasonable. In this respect, we may also view the M_J-changing cross sections presented in Fig. 3.4 as approximate upper bounds. Nevertheless, it must be noted that the relatively deep wells in the reactive potentials will give rise to a large number of bound states, which in turn may cause strong resonances in the cross sections. In order to verify these assumptions, we will perform reactive quantum scattering calculations for NH + NH with all three interaction potentials included (Chapter 6).

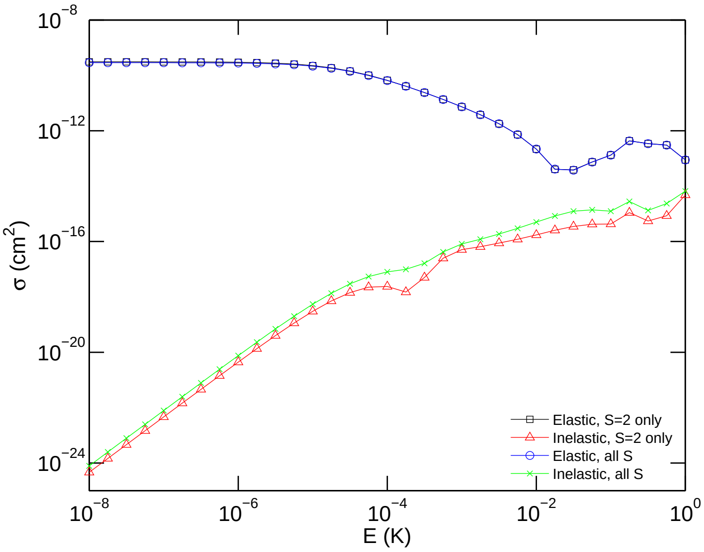

Figure 3.4: Elastic and inelastic M_J-changing cross sections for magnetically trapped ^{15}NH obtained from scattering calculations with only the quintet state included in the basis. The cross sections calculated with all three spin states included (*"all S"*) are shown for comparison.

3.3.3 Sensitivity to potential and basis-set size

In this section we address two interrelated topics, namely the sensitivity to the potential and the dependence on the angular basis-set size. It is well established that low-energy scattering depends strongly on the presence of bound and quasi-bound states near the dissociation threshold. Such states can give rise to scattering resonances that may enhance the collision cross section by several orders of magnitude. The energies of these (quasi-)bound states are highly sensitive to the details of the potential energy surface, and hence they are very difficult to predict from first principles. Even a state-of-the art *ab initio* potential cannot reliably predict whether a particular near-dissociation state lies above or below the threshold. This is particularly true for systems with multiple degrees of freedom and deep potential wells, for which the density of states is relatively high. Thus, in order to assess the accuracy of the cross sections, we must carefully take into account the effect of uncertainties in the potential. In a related manner, we also consider the effect of using different channel basis-set sizes in the scattering calculations. The size of the angular basis set can influence the energies of the (quasi-)bound states, which in turn can lead to a different resonance structure. It will be demonstrated, however, that the use of a reduced basis set leads only to a shift in the resonance positions, and does not significantly alter the general resonance pattern.

We first consider the sensitivity of the calculated cross sections to the potential energy surface. Our potential has been obtained from state-of-the-art *ab initio* calculations, and we estimate that it differs from the exact potential by at most a few percent. For practical reasons, we have studied the potential dependence indirectly by performing scattering calculations as a function of the reduced mass μ. Since scaling the reduced mass by a factor of λ ($\mu_{\text{scaled}} = \lambda\mu$) is almost equivalent to scaling the entire interaction potential by λ [65], this provides a stringent test for the sensitivity to the potential. The true potential does not necessarily differ from our *ab initio* surface by only a constant factor, but scaling by λ ($0.9 \leq \lambda \leq 1.1$) amply samples the range of possibilities within which the exact potential is expected to lie.

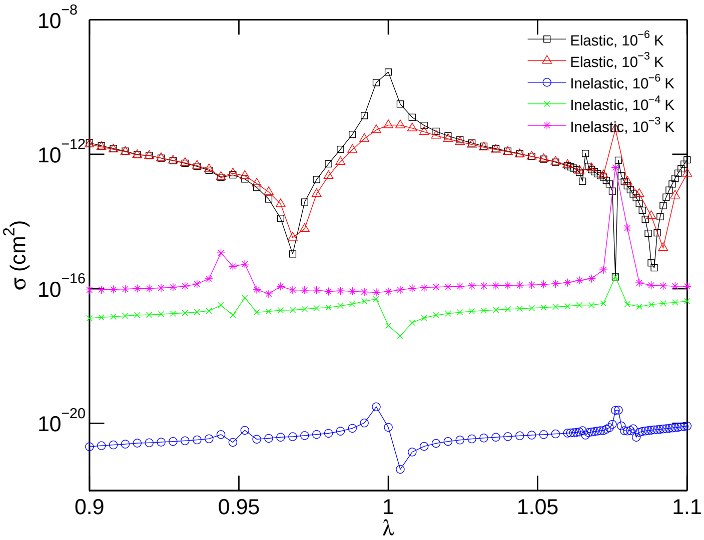

Figure 3.5: Elastic and inelastic M_J-changing cross sections for magnetically trapped ^{15}NH as a function of the scaling parameter λ, calculated at collision energies of 10^{-6} K, 10^{-4} K, and 10^{-3} K. The elastic cross sections for 10^{-4} K are the same as for 10^{-6} K.

Figure 3.5 shows the cross sections as a function of λ at collision energies of 10^{-6} K,

10^{-4} K, and 10^{-3} K. It can be seen that both the elastic and inelastic cross sections change by several orders of magnitude as a function of λ, but they vary about a certain background value. For instance, the elastic cross sections fluctuate around $\sim 10^{-12}$ cm^2 for all three collision energies. The background values for the inelastic cross sections increase with E^2 in the ultracold regime, consistent with the results of Fig. 3.1 and the threshold laws discussed in Sec. 3.3.1. The deviations from the background values are due to scattering resonances, which arise from NH–NH states that change from bound to quasi-bound at the $|M_{J_A} = 1, M_{J_B} = 1\rangle$ threshold. Such resonance features are to be expected as a function of λ, since a scaling of the potential, or in fact any modification of the potential energy surface, will cause a shift in the bound-state energies. For 10^{-6} K, 10^{-4} K, and 10^{-3} K, the resonances are located around the same values of λ, and hence the λ-dependent resonance structure would not be averaged out in a thermal (Maxwell-Boltzmann) distribution at temperatures below 1 mK. That is, thermally averaged rate constants are likely to show a similar sensitivity to the potential as the calculated cross sections.

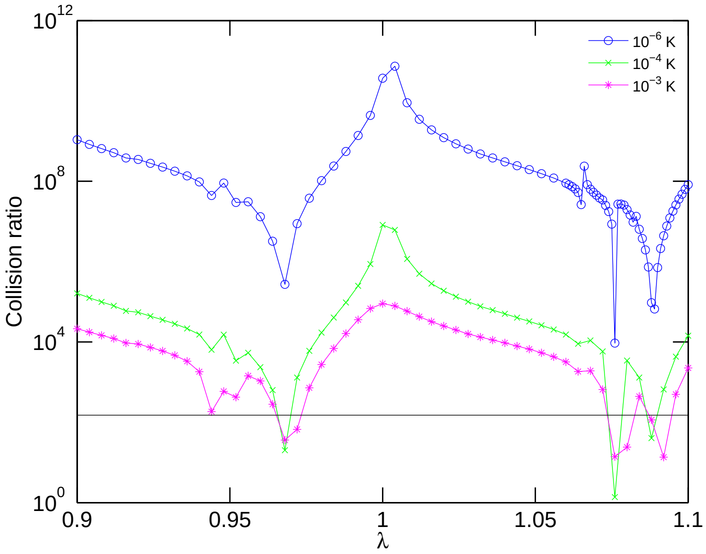

Figure 3.6: Elastic-to-inelastic cross-section ratios for magnetically trapped ^{15}NH as a function of the scaling parameter λ, calculated at collision energies of 10^{-6} K, 10^{-4} K, and 10^{-3} K. The horizontal black line indicates the critical value of 150 that is required for efficient evaporative cooling.

Let us now consider the elastic-to-inelastic cross-section ratios as a function of λ. These are shown in Fig. 3.6 for $E = 10^{-6}$ K, 10^{-4} K, and 10^{-3} K. For clarity, we have also indicated the critical ratio of 150 that is required for efficient evaporative cooling. As can be seen, the calculated ratios exceed 150 for almost all values of λ and all energies considered, except when λ is close to resonance. This demonstrates that evaporative cooling of NH is feasible at energies below 1 mK for most of the λ-values considered. Although we cannot predict which value of λ corresponds most closely to the exact potential, we do expect that the sampled range of λ is indicative of the range within which the exact potential lies, and hence we conclude that the *probability* for successful evaporative cooling is relatively large. That is, the true potential is very likely to be such that the elastic-to-inelastic ratio exceeds 150.

The λ-scaling approach is also used to investigate the influence of the angular basis-set size on the scattering results. First we point out that the strong anisotropy of the potential and the large reduced mass of NH–NH require relatively high values of the basis-set parameters $N_{\max}$ and $L_{\max}$. In addition, the triplet spins on the monomers increase the channel basis-set size by a factor of 9, making it highly challenging to achieve full basis-set convergence. Figure 3.7 shows the cross sections as a function of λ for different values of $N_{\max}$ and $L_{\max}$ at a collision energy of 10^{-6} K. The maximum number of channels in these calculations ranged from 937 for $N_{\max} = 4$ and $L_{\max} = 6$ ($\mathcal{J} = 4$) up to 2382 for $N_{\max} = 6$ and $L_{\max} = 6$ ($\mathcal{J} = 5$). It can be seen that the cross sections all vary by several orders of magnitude as a function of λ, and for a given value of λ the four basis sets can yield very different numerical results. However, the different cross sections vary about the same background values and the resonant features have similar widths for all four basis sets. Thus, a change in $N_{\max}$ or $L_{\max}$ may cause a shift in the positions of the resonances, but the overall pattern is virtually unaffected. The estimated probability for successful evaporative cooling, i.e. the probability that the exact potential is such that the elastic-to-inelastic cross-section ratio exceeds 150, is therefore similar for all four basis sets. This can also be understood by considering that a change in the basis set only shifts the bound-state energy levels, similar to the effect of scaling the potential.

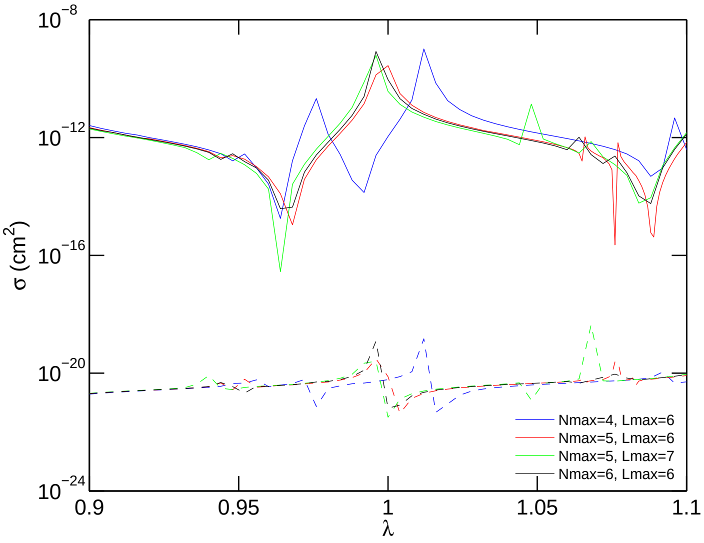

Figure 3.7: Elastic and inelastic M_J-changing cross sections for magnetically trapped ^{15}NH as a function of λ, calculated for different basis sets at a collision energy of 10^{-6} K. Solid lines correspond to elastic cross sections and dashed lines to inelastic cross sections. Different colors represent different basis sets.

The results of Fig. 3.7 demonstrate that the cross sections are almost, but not fully converged with respect to N_{max} and L_{max}. Using a larger basis set is infeasible at present given the available computer power. Moreover, taking into account the uncertainty in the potential, even a fully converged basis set would not give really reliable numerical values due to the presence of (quasi-)bound state resonances. Since the exact form of the potential, and thus the precise locations of the resonances, are still unknown, the calculated cross sections are subject to an inherent degree of uncertainty that cannot be reduced by the use of a fully converged basis set. In this sense, full basis-set convergence will not necessarily yield a more accurate prediction of the true cross sections. On the other hand, the *probability* for successful evaporative cooling can be reliably predicted using an incompletely converged basis set, and hence we conclude that, even if full basis-set convergence could be achieved, this would not significantly alter our main qualitative results. We emphasize, however, that it is crucial to test the sensitivity to the potential in order to assess the accuracy of the calculated cross sections. As a final point, we note that the uncertainty limits of the potential could, in principle, be greatly reduced by measuring the cross sections experimentally.

3.4 Conclusions

We have carried out elastic and inelastic quantum scattering calculations on a state-of-the-art *ab initio* potential to study field-free NH + NH collisions at low and ultralow temperatures. The results indicate that, when the molecules are prepared in their nuclear-spin stretched states, bosonic ^{15}NH is more suitable for evaporative cooling than fermionic ^{14}NH. This is a direct consequence of the Pauli principle, which forbids s-wave scattering for two identical fermions. The ^{14}NH isotope might also be successfully cooled, however, when the monomers are in a mixture of different nuclear spin states.

We have assumed that all three spin states of the NH–NH complex are described by the non-reactive quintet surface. This approximation is shown to be reasonable, although a full reactive scattering calculation would be required to investigate the precise role of the chemically active singlet and triplet states.

The collision cross sections are sensitive to the details of the interaction potential, because of the presence of quasi-bound states that cause scattering resonances. Since the exact potential is unknown, this gives rise to a degree of uncertainty in the numerical cross sections. However, a sampling of the range of possibilities indicates that the exact potential is likely to be such that the elastic-to-inelastic cross-section ratio is favorable for evaporative cooling. This result is only weakly dependent on the size of the channel basis set. In particular, the effect of using a reduced basis set is very similar to a scaling of the potential within its uncertainty. Thus, even without obtaining full basis-set convergence, we can provide valuable insight into the feasibility of evaporative cooling. This also offers hope for the theoretical treatment of other open-shell bimolecular systems for which full convergence is difficult to achieve.

Chapter 4

Scattering in magnetic fields

This chapter is dedicated to NH + NH collisions in an external magnetic field. We present elastic and spin-changing inelastic scattering cross sections for magnetically trapped NH, calculated as a function of energy and magnetic field strength. We specifically investigate the influence of the intramolecular spin-spin, spin-rotation, and intermolecular magnetic dipole coupling on the collision dynamics. It is shown that ^{15}NH is a suitable candidate for evaporative cooling experiments. The dominant trap-loss mechanism in the ultracold regime originates from the intermolecular dipolar coupling term. At higher energies and fields, intramolecular spin-spin coupling becomes increasingly important. Our qualitative results and conclusions are fairly independent of the exact form of the potential and of the size of the channel basis set.

4.1 Introduction

As shown in Chapter 3, and also in earlier work by Kajita [89], the NH radical is a very promising candidate for molecular evaporative cooling, particularly the bosonic ^{15}NH isotopologue. Fermionic ^{14}NH may also be cooled into the μK regime by applying an electric field [89] or by preparing the molecules in different hyperfine states (see Chapter 3). It must be noted, however, that the results of Kajita were obtained from approximate analytical methods in which only the electric dipole-dipole and magnetic dipole-dipole interactions were included. The work described in Chapter 3 involved rigorous quantum scattering calculations on a full four-dimensional potential energy surface, but focused only on NH + NH collisions in zero field.

In this chapter, we consider collisions between ^{15}NH molecules in the presence of an external magnetic field. We present full quantum scattering calculations on an accurate *ab initio* quintet potential to investigate the collision dynamics at low and ultralow temperatures. Intramolecular spin-spin coupling, spin-rotation, and intermolecular magnetic dipolar coupling are explicitly included in the calculations. We will identify the dominant trap-loss mechanisms and provide a detailed discussion of the dynamics.

4.2 Calculations

4.2.1 Theory

We consider elastic and inelastic collisions between two identical NH($X\,^3\Sigma^-$) molecules in the presence of a magnetic field. Since bosonic ^{15}NH is more suitable for evaporative cooling that fermionic ^{14}NH, we will focus only on the ^{15}NH isotopologue. We treat the colliding molecules as rigid rotors. The coordinate system is defined in a space-fixed frame, with $\boldsymbol{R} \equiv (R, \Omega)$ and $\Omega = (\Phi, \Theta)$ denoting the intermolecular vector between the centers of mass of the molecules. The coordinates $\omega_A = (\theta_A, \phi_A)$ and $\omega_B = (\theta_B, \phi_B)$ are the polar angles of monomers A and B, respectively (see Fig. 2.1). We neglect hyperfine structure and assume that both molecules are in their nuclear-spin stretched states $|I, M_I = I\rangle$, with $I = I_\mathrm{N} + I_\mathrm{H} = 1$ denoting the maximum total nuclear spin and M_I its laboratory-frame projection. The scattering Hamiltonian is then given by

$$\begin{aligned}\hat{H} &= -\frac{\hbar^2}{2\mu R}\frac{\partial^2}{\partial R^2}R + \frac{\hat{L}^2}{2\mu R^2} + \sum_{S,M_S} |S, M_S\rangle V_S(\boldsymbol{R}, \omega_A, \omega_B)\langle S, M_S| \\ &\quad + V_\mathrm{magn.dip}(\boldsymbol{R}, \hat{\boldsymbol{S}}_A, \hat{\boldsymbol{S}}_B) + \hat{H}_A + \hat{H}_B, \qquad (4.1)\end{aligned}$$

where μ is the reduced mass of the complex, $\hat{L}^2$ is the angular momentum operator associated with end-over-end rotation of the vector $\boldsymbol{R}$, $V_S(\boldsymbol{R}, \omega_A, \omega_B)$ is the potential energy surface for total spin S, M_S is the projection of S onto the magnetic-field axis, $V_\mathrm{magn.dip}(\boldsymbol{R}, \hat{\boldsymbol{S}}_A, \hat{\boldsymbol{S}}_B)$ is the intermolecular magnetic dipole interaction, and $\hat{H}_A$ and $\hat{H}_B$ are the Hamiltonians of the two monomers. The intermolecular magnetic dipole term is given by

$$V_\mathrm{magn.dip}(\boldsymbol{R}, \hat{\boldsymbol{S}}_A, \hat{\boldsymbol{S}}_B) = -\sqrt{6} g_S^2 \mu_\mathrm{B}^2 \frac{\alpha^2}{R^3} \sum_q (-1)^q C_{2,-q}(\Omega) [\hat{\boldsymbol{S}}_A \otimes \hat{\boldsymbol{S}}_B]^{(2)}_q \qquad (4.2)$$

where $g_S \approx 2.0023$ is the electron g-factor, μ_B is the Bohr magneton, α is the fine-structure constant, and the factor in square brackets is the tensor product of the monomer spin operators $\hat{\boldsymbol{S}}_A$ and $\hat{\boldsymbol{S}}_B$. The monomer operators $\hat{H}_i$ ($i = A, B$) each contain a rotation, spin-rotation, intramolecular spin-spin, and Zeeman term,

$$\hat{H}_i = B_0 \hat{N}_i^2 + \gamma \hat{\boldsymbol{N}}_i \cdot \hat{\boldsymbol{S}}_i + \frac{2}{3}\sqrt{6}\lambda_\mathrm{SS} \sum_q (-1)^q C_{2,-q}(\omega_i) [\hat{\boldsymbol{S}}_i \otimes \hat{\boldsymbol{S}}_i]^{(2)}_q + g_S \mu_\mathrm{B} \boldsymbol{B} \cdot \hat{\boldsymbol{S}}_i, \quad (4.3)$$

where $\hat{\boldsymbol{N}}_i$ is the operator for the rotational angular momentum of monomer i and $\boldsymbol{B}$ is the magnetic field vector. For brevity, the intramolecular term will be denoted as $\hat{V}_\mathrm{SS}^{(i)}$. The numerical values for the rotational, spin-rotation, and spin-spin constants of

^{15}NH can be obtained from those of ^{14}NH [113] using isotope scaling (see e.g. p. 239 of Ref. [114]): $B_0 = 16.270\,340$ cm^{-1}, $\gamma = -0.054\,60$ cm^{-1}, and $\lambda_{\text{SS}} = 0.919\,89$ cm^{-1}.

In analogy to Chapter 3, we will assume that all three spin states of the complex are described by the non-reactive quintet surface, i.e. $V_S(\boldsymbol{R}, \omega_A, \omega_B) \equiv V_2(\boldsymbol{R}, \omega_A, \omega_B)$. It will be shown in Chapter 6 that this assumption is reasonable for non-reactive NH + NH scattering. The data for the $S = 2$ surface are taken from Chapter 2. The potential is expanded in coupled spherical harmonics $Y_{L,M}$ [115],

$$
\begin{aligned}
V(\boldsymbol{R}, \omega_A, \omega_B) &= \sum_{L_A, L_B, L_{AB}} \upsilon_{L_A, L_B, L_{AB}}(R) A_{L_A, L_B, L_{AB}}(\Omega, \omega_A, \omega_B), &(4.4)\\
A_{L_A, L_B, L_{AB}}(\Omega, \omega_A, \omega_B) &= \sum_{M_A, M_B, M_{AB}} \langle L_A M_A L_B M_B | L_{AB} M_{AB} \rangle \\
&\quad \times Y_{L_A, M_A}(\omega_A) Y_{L_B, M_B}(\omega_B) Y^*_{L_{AB}, M_{AB}}(\Omega), &(4.5)
\end{aligned}
$$

where $\langle L_A M_A L_B M_B | L_{AB} M_{AB} \rangle$ is a Clebsch-Gordan coefficient and the superscript * denotes complex conjugation. The subscript $S = 2$ has been omitted for brevity. As noted previously, the $\upsilon_{L_A, L_B, L_{AB}}(R)$ expansion coefficients of Chapter 2 must be divided by a factor of $(-1)^{L_A - L_B}(4\pi)^{-3/2}(2L_{AB}+1)[(2L_A+1)(2L_B+1)]^{1/2}$ to obtain the potential in the form of Eq. (4.4).

We expand the wave function in a space-fixed uncoupled basis introduced in Ref. [86]. The angular functions are written as products of the eigenfunctions of $\hat{N}_i^2$, $\hat{N}_{i_z}$, $\hat{S}_i^2$, $\hat{S}_{i_z}$, $\hat{L}^2$, and $\hat{L}_z$,

$$
|N_A M_{N_A}\rangle |S_A M_{S_A}\rangle |N_B M_{N_B}\rangle |S_B M_{S_B}\rangle |L M_L\rangle \equiv |\gamma_A \gamma_B\rangle |L M_L\rangle, \tag{4.6}
$$

with N_A and N_B ranging from 0 to $N_{\max}$ and $L = 0, \ldots, L_{\max}$. The matrix elements of the scattering Hamiltonian [Eq. (4.1)] in the basis of Eq. (4.6) have all been given by Krems and Dalgarno [86], but we list them here for the sake of clarity. For the angular functions of the potential [Eq. (4.5)] we find

$$
\begin{aligned}
&\langle \gamma_A \gamma_B L M_L | A_{L_A, L_B, L_{AB}} | \gamma'_A \gamma'_B L' M'_L \rangle = \\
&\quad \delta_{M_{S_A} M'_{S_A}} \delta_{M_{S_B} M'_{S_B}} \left(\frac{1}{4\pi}\right)^{3/2} [L_{AB}] \sqrt{[L_A][L_B][N_A][N'_A][N_B][N'_B][L][L']} \\
&\quad \times \sum_{M_A, M_B, M_{AB}} (-1)^{M_{N_A} + M_{N_B} + M_L - L_A + L_B} \begin{pmatrix} N_A & L_A & N'_A \\ -M_{N_A} & M_A & M'_{N_A} \end{pmatrix} \\
&\quad \times \begin{pmatrix} N_B & L_B & N'_B \\ -M_{N_B} & M_B & M'_{N_B} \end{pmatrix} \begin{pmatrix} L & L_{AB} & L' \\ -M_L & M_{AB} & M'_L \end{pmatrix} \begin{pmatrix} L_A & L_B & L_{AB} \\ M_A & M_B & M_{AB} \end{pmatrix} \\
&\quad \times \begin{pmatrix} N_A & L_A & N'_A \\ 0 & 0 & 0 \end{pmatrix} \begin{pmatrix} N_B & L_B & N'_B \\ 0 & 0 & 0 \end{pmatrix} \begin{pmatrix} L & L_{AB} & L' \\ 0 & 0 & 0 \end{pmatrix},
\end{aligned} \tag{4.7}
$$

with the factors in large parentheses denoting Wigner $3j$ symbols and $[Q] = (2Q+1)$. We point out that our angular functions differ by a factor of $(-1)^{L_A - L_B}(4\pi)^{3/2}(2L_{AB}+$

$1)^{-1/2}$ from the functions used in Ref. [86]. The intermolecular magnetic dipole-dipole term gives (see also Eq. (A2) of Ref. [121])

$$\begin{aligned}
&\langle \gamma_A\gamma_B L M_L | V_{\text{magn.dip}} | \gamma'_A\gamma'_B L' M'_L \rangle = \\
&\quad -\delta_{N_A N'_A}\delta_{N_B N'_B}\delta_{N_{M_A} N'_{M_A}}\delta_{N_{M_B} M_{N'_B}} \sqrt{30}\frac{\alpha^2}{R^3}(-1)^{S_A+S_B-M_{S_A}-M_{S_B}+M_L} \\
&\quad \times \sqrt{S_A(S_A+1)S_B(S_B+1)[S_A][S_B][L][L']} \begin{pmatrix} L & 2 & L' \\ 0 & 0 & 0 \end{pmatrix}, \\
&\quad \times \sum_{m_A,m_B} \begin{pmatrix} L & 2 & L' \\ -M_L & -(m_A+m_B) & M'_L \end{pmatrix} \begin{pmatrix} 1 & 1 & 2 \\ m_A & m_B & -(m_A+m_B) \end{pmatrix} \\
&\quad \times \begin{pmatrix} S_A & 1 & S_A \\ -M_{S_A} & m_A & M'_{S_A} \end{pmatrix} \begin{pmatrix} S_B & 1 & S_B \\ -M_{S_B} & m_B & M'_{S_B} \end{pmatrix}.
\end{aligned} \tag{4.8}$$

Note that the sums over m_A and m_B collapse for any individual matrix element due to the selection rules imposed by the last two $3j$ symbols. The rotational and Zeeman terms are completely diagonal in the decoupled basis,

$$\langle \gamma_A\gamma_B L M_L | B_0 \hat{N}_i^2 | \gamma'_A\gamma'_B L' M'_L \rangle = \delta_{\gamma_A\gamma'_A}\delta_{\gamma_B\gamma'_B}\delta_{LL'}\delta_{M_L M'_L} B_0 N_i(N_i+1), \tag{4.9}$$

$$\langle \gamma_A\gamma_B L M_L | g_S\mu_B \boldsymbol{B}\cdot\hat{\boldsymbol{S}}_i | \gamma'_A\gamma'_B L' M'_L \rangle = \delta_{\gamma_A\gamma'_A}\delta_{\gamma_B\gamma'_B}\delta_{LL'}\delta_{M_L M'_L} g_S\mu_B B_z M_{S_i}, \tag{4.10}$$

with B_z representing the z-component of the magnetic field. For monomer A, the matrix elements of the intramolecular spin-rotation operator are given by

$$\begin{aligned}
&\langle \gamma_A\gamma_B L M_L | \gamma \hat{\boldsymbol{N}}_A\cdot\hat{\boldsymbol{S}}_A | \gamma'_A\gamma'_B L' M'_L \rangle = \\
&\quad \delta_{N_A N'_A}\delta_{N_B N'_B}\delta_{M_{N_B} M'_{N_B}}\delta_{M_{S_B} M'_{S_B}}\delta_{LL'}\delta_{M_L M'_L}\gamma \\
&\quad \times \Big\{ \delta_{M_{N_A} M'_{N_A}}\delta_{M_{S_A} M'_{S_A}} M_{N_A} M_{S_A} \\
&\quad + \frac{1}{2}\delta_{M_{N_A} M'_{N_A}+1}\delta_{M_{S_A} M'_{S_A}-1}\sqrt{[N_A(N_A+1) - M'_{N_A}(M'_{N_A}+1)]} \\
&\quad \times \sqrt{[S_A(S_A+1) - M'_{S_A}(M'_{S_A}-1)]} \\
&\quad + \frac{1}{2}\delta_{M_{N_A} M'_{N_A}-1}\delta_{M_{S_A} M'_{S_A}+1}\sqrt{[N_A(N_A+1) - M'_{N_A}(M'_{N_A}-1)]} \\
&\quad \times \sqrt{[S_A(S_A+1) - M'_{S_A}(M'_{S_A}+1)]} \Big\},
\end{aligned} \tag{4.11}$$

and for the intramolecular spin-spin term $\hat{V}_{\text{SS}}^{(A)i}$ we obtain

$$\begin{aligned}
&\langle \gamma_A\gamma_B L M_L | \hat{V}_{\text{SS}}^{(A)i} | \gamma'_A\gamma'_B L' M'_L \rangle = \\
&\quad \delta_{N_B N'_B}\delta_{M_{N_B} M'_{N_B}}\delta_{M_{S_B} M'_{S_B}}\delta_{LL'}\delta_{M_L M'_L}\frac{2}{3}\lambda_{\text{SS}}(-1)^{M_{N_A}+S_A-M_{S_A}} \\
&\quad \times \sqrt{[N_A][N'_A][S_A]S_A(2S_A-1)(S_A+1)(S_A+3)} \begin{pmatrix} N_A & 2 & N'_A \\ 0 & 0 & 0 \end{pmatrix} \\
&\quad \times \sum_{m_A}(-1)^{m_A} \begin{pmatrix} N_A & 2 & N'_A \\ -M_{N_A} & -m_A & M'_{N_A} \end{pmatrix} \begin{pmatrix} S_A & 2 & S_A \\ -M_{S_A} & m_A & M'_{S_A} \end{pmatrix},
\end{aligned} \tag{4.12}$$

where again the sum over m_A collapses for given values of M_{N_A}, M'_{N_A}, M_{S_A}, and M'_{S_A}. The matrix elements of the intramolecular operators for monomer B can be found by interchanging the A and B indices in Eqs. (4.11) and (4.12).

Since the monomers are identical, we can exploit the permutation symmetry of the system to minimize the computational cost. Following Ref. [87], we employ a normalized, symmetrized basis of the form

$$|\phi^{\eta}_{\gamma_A\gamma_B LM_L}\rangle = \frac{1}{[2(1+\delta_{\gamma_A\gamma_B})]^{1/2}}\left[|\gamma_A\gamma_B\rangle|LM_L\rangle + \eta(-1)^L|\gamma_B\gamma_A\rangle|LM_L\rangle\right], \tag{4.13}$$

with $\eta = \pm 1$ defining the symmetry of the wave function with respect to molecular interchange. It is sufficient to restrict the basis to a well-ordered set of molecular states, i.e. $\gamma_A \geq \gamma_B$. Finally, we note that the parity, $\epsilon = (-1)^{N_A+N_B+L}$, and the total angular momentum projection quantum number, $\mathcal{M} = M_{N_A} + M_{S_A} + M_{N_B} + M_{S_B} + M_L$, are also conserved during collision. Thus, the scattering calculations may be performed for a single value of $\mathcal{M}$, η, and ϵ. Here we consider only collisions between bosonic ^{15}NH molecules in their spin-stretched and rotational ground state ($N_A = N_B = 0$), for which we have $\eta = +1$ and $\epsilon = +1$. Note that the first excited rotational state has an energy of ≈ 32 cm^{-1} (46 K), and is therefore inaccessible at the energies considered in this work.

We solve the coupled equations using the hybrid log-derivative method of Alexander and Manolopoulos [80], which uses a fixed-step-size log-derivative propagator in the short range and a variable-step-size Airy propagator at long range. Matching to asymptotic boundary conditions yields the scattering S-matrices, from which the cross sections can be readily obtained. We note that, due to the intramolecular spin-rotation and spin-spin couplings, the basis functions of Eq. (4.13) are not exact eigenfunctions of the asymptotic Hamiltonian $\hat{H}_A + \hat{H}_B$, while the S-matrices must be constructed in terms of these eigenfunctions. As detailed in Refs. [86] and [87], an additional basis transformation of the log-derivative matrix is therefore required before matching to the asymptotic boundary conditions. We will denote the symmetrized channel eigenfunctions as $|\phi^{\eta}_{\bar{\gamma}_A\bar{\gamma}_B LM_L}\rangle$, with $|\bar{\gamma}_A\bar{\gamma}_B\rangle \equiv |(\bar{N}_A, S_A)J_A, M_{J_A}\rangle|(\bar{N}_B, S_B)J_B, M_{J_B}\rangle$ defining the molecular eigenstates. Here $\bar{N}_i$ is used instead of N_i, because N_i is strictly not an exact quantum number due to the intramolecular spin-spin coupling. However, the intramolecular coupling is relatively weak and N_i, M_{N_i}, and M_{S_i} may be treated as approximately good quantum numbers. Specifically, for the ^{15}NH rotational ground state, the magnetically trapped $|J_i = 1, M_{J_i} = 1\rangle$ component contains 99.992% of $|N_i = 0, M_{N_i} = 0, S_i = 1, M_{S_i} = 1\rangle$ for all fields considered in this work.

The cross sections at total energy E are calculated using the expression [87]

$$\sigma^{\eta}_{\bar{\gamma}_A\bar{\gamma}_B\to\bar{\gamma}'_A\bar{\gamma}'_B}(E) = \frac{\pi(1+\delta_{\bar{\gamma}_A\bar{\gamma}_B})}{k^2_{\bar{\gamma}_A\bar{\gamma}_B}} \sum_{L,M_L}\sum_{L',M'_L}\left|T^{\eta}_{\bar{\gamma}_A\bar{\gamma}_B LM_L;\bar{\gamma}'_A\bar{\gamma}'_B L'M'_L}(E)\right|^2, \tag{4.14}$$

where $k_{\bar{\gamma}_A\bar{\gamma}_B}$ is the wavenumber for the incident channel, $k^2_{\bar{\gamma}_A\bar{\gamma}_B} = 2\mu(E - \epsilon_{\bar{\gamma}_A} - \epsilon_{\bar{\gamma}_B})/\hbar^2$, $\epsilon_{\bar{\gamma}_A} + \epsilon_{\bar{\gamma}_B}$ is the corresponding channel energy, and the T-matrix elements are defined as $T^{\eta}_{\bar{\gamma}_A\bar{\gamma}_B LM_L;\bar{\gamma}'_A\bar{\gamma}'_B L'M'_L} = \delta_{\bar{\gamma}_A\bar{\gamma}'_A}\delta_{\bar{\gamma}_B\bar{\gamma}'_B}\delta_{LL'}\delta_{M_L M'_L} - S^{\eta}_{\bar{\gamma}_A\bar{\gamma}_B LM_L;\bar{\gamma}'_A\bar{\gamma}'_B L'M'_L}$.

4.2.2 Computational details

We performed the scattering calculations for different magnetic field strengths using the MOLSCAT package [116, 117], extended to handle the basis set of Eq. (4.13). The log-derivative propagation was carried out on a radial grid ranging from 4.5 to 15 a_0 in steps of 0.02 a_0. The Airy propagation ranged from 15 to 50 000 a_0. We included basis functions up to $N_{\max} = 2$ and $L_{\max} = 6$, yielding a maximum number of 1038 channels for a single calculation ($\mathcal{M} = 0$). The expansion of the quintet potential energy surface was truncated at $L_A = L_B = 6$. As mentioned in Section 4.2.1, the chemically reactive singlet and triplet potentials were not included in the calculations.

4.3 Results and discussion

4.3.1 Adiabatic potential energy curves

Before discussing the cross sections, we first consider the adiabatic potential curves. These are obtained by diagonalizing the interaction matrix at fixed R over a grid of R-values and subsequently connecting the corresponding eigenvalues. Asymptotically, these adiabatic curves correlate to the molecular eigenstates $\bar{\gamma}_A$ and $\bar{\gamma}_B$. Figure 4.1 shows the long range of the lowest adiabats for $\mathcal{M} = 2$ and $L_{\max} = 4$ at a magnetic field of 0.1 G. We present only the curves with exchange symmetry $\eta = +1$ and parity $\epsilon = +1$, for which s-wave scattering in the incident spin-stretched channel is allowed. The asymptotic energy splittings between the different molecular states originate from the Zeeman term $g_S \mu_{\mathrm{B}} B(M_{S_A} + M_{S_B})$. For $\mathcal{M} = 2$ and $L_{\max} = 4$, the magnetically trapped state with $|M_{J_A} = M_{J_B} = 1\rangle$ has partial-wave contributions of $L = 0$, 2, and 4, as can be seen in Fig. 4.1. The adiabats correlating with $|M_{J_A} = 1, M_{J_B} = 0\rangle$, $|M_{J_A} = 1, M_{J_B} = -1\rangle$, and $|M_{J_A} = 0, M_{J_B} = 0\rangle$ have $L = 2$ and 4 centrifugal barriers, and the adiabats for $|M_{J_A} = 0, M_{J_B} = -1\rangle$ and $|M_{J_A} = -1, M_{J_B} = -1\rangle$ contain only the $L = 4$ partial wave. For the $|M_{J_A} = 1, M_{J_B} = -1\rangle$ and $|M_{J_A} = 0, M_{J_B} = 0\rangle$ states, which have identical Zeeman shifts, the degeneracy is further lifted by the intramolecular spin-spin coupling.

It can be seen that several curve crossings occur in the region between $R \approx 1500$ and 4500 a_0. If we neglect the small energy shifts due to the intramolecular coupling, the crossing points R_c are simply given by

$$g_S \mu_{\mathrm{B}} B \Delta M_S = \frac{\hbar^2 \left[L_f(L_f+1) - L_i(L_i+1)\right]}{2\mu R_c^2}, \tag{4.15}$$

where L_i and L_f denote the values of L for the adiabats correlating to the incoming and outgoing channels, respectively, and $\Delta M_S = M_{S_A}^{(i)} + M_{S_B}^{(i)} - M_{S_A}^{(f)} - M_{S_B}^{(f)}$. The corresponding energies at which the crossings occur are given by $E_c = \hbar^2 L_i(L_i+1)/(2\mu R_c^2)$, defined relative to the threshold of the incident channel. We find that several of these crossings are narrowly avoided due to the presence of the intermolecular magnetic

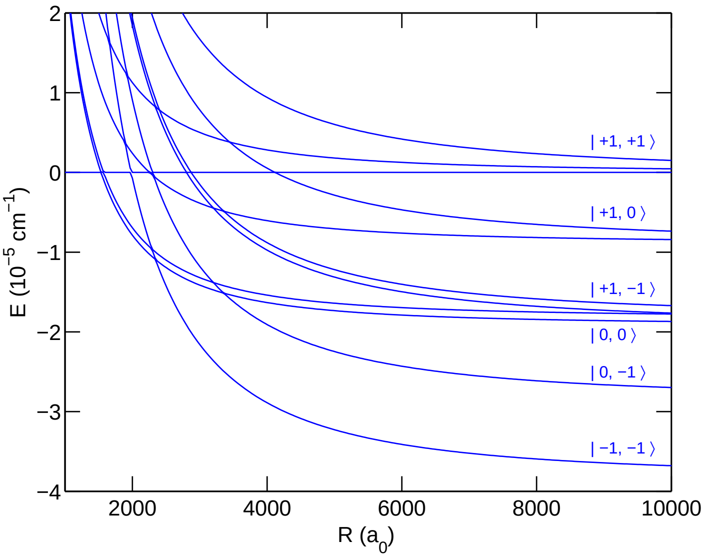

Figure 4.1: Lowest adiabatic potential curves for ^{15}NH – ^{15}NH, calculated for $L_{\max} = 4$ and $\mathcal{M} = 2$ at a magnetic field of 0.1 G. The adiabats are plotted as a function of R in units of the Bohr radius a_0. The molecular eigenstates are labeled by $|M_{J_A}, M_{J_B}\rangle$ and refer to the well-ordered states $|(N_A = 0)J_A = 1, M_{J_A}\rangle|(N_B = 0)J_B = 1, M_{J_B}\rangle$.

dipole interaction. Inspection of Eq. (4.8) shows that e.g. the s-wave incident channel with $|M_{S_A} = 1, M_{S_B} = 1, L = 0\rangle$ is directly coupled with $|M_{S_A} = 1, M_{S_B} = 0, L = 2\rangle$ and $|M_{S_A} = 0, M_{S_B} = 0, L = 2\rangle$ via the magnetic dipole term, giving rise to the corresponding avoided crossings. We note, however, that $V_{\text{magn.dip}}$ contains a second-rank tensor in Ω and can therefore directly couple channels only if $|L_i - L_f| \leq 2$. The spin operators $\hat{S}_A$ and $\hat{S}_B$ contained in $V_{\text{magn.dip}}$ are first-rank tensors and, consequently, M_{S_A} and M_{S_B} may each differ at most by 1. Thus, not all crossings are avoided. To take proper account of these avoided crossings and account correctly for the magnetic dipole coupling in the ultracold regime, it is essential that the radial grid used in the calculations extends beyond the outermost R_c value. The influence of the avoided crossings on the collision cross sections will be discussed in detail in the following section.

4.3.2 Cross sections

Figure 4.2 shows the total elastic and M_J-changing inelastic cross sections for two magnetically trapped ^{15}NH molecules ($M_{J_A} = M_{J_B} = 1$) as a function of collision energy. The cross sections as a function of magnetic field are given in Fig. 4.3. We find that the elastic cross sections are significantly larger than the inelastic ones over a wide range of energies and magnetic fields, suggesting that evaporative cooling of ^{15}NH is likely to be successful. It can also be seen that, in the ultracold regime, the total inelastic cross section decreases dramatically if the magnetic field strength is reduced.

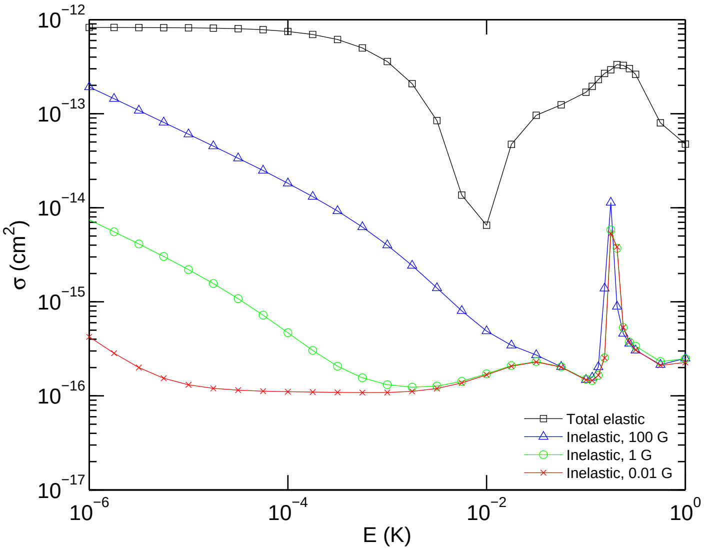

Figure 4.2: Elastic and inelastic M_J-changing cross sections for magnetically trapped ^{15}NH as a function of collision energy for various magnetic fields. The elastic cross sections are the same for all three magnetic field strengths.

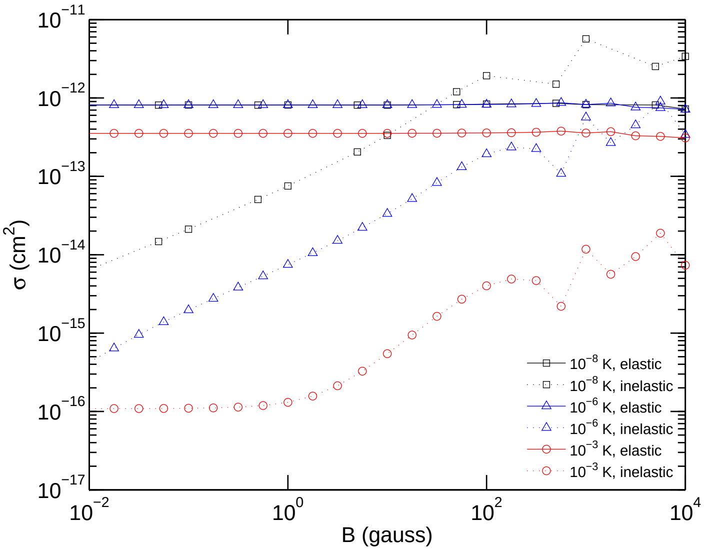

Figure 4.3: Elastic and inelastic M_J-changing cross sections for magnetically trapped ^{15}NH as a function of magnetic field for various collision energies.

Thus, once the cooling process has started in the millikelvin regime at relatively high magnetic field, and continues towards lower energies as the magnetic trap depth is decreased, the ratio between elastic and M_J-changing cross sections will remain very favorable for evaporative cooling to take place.

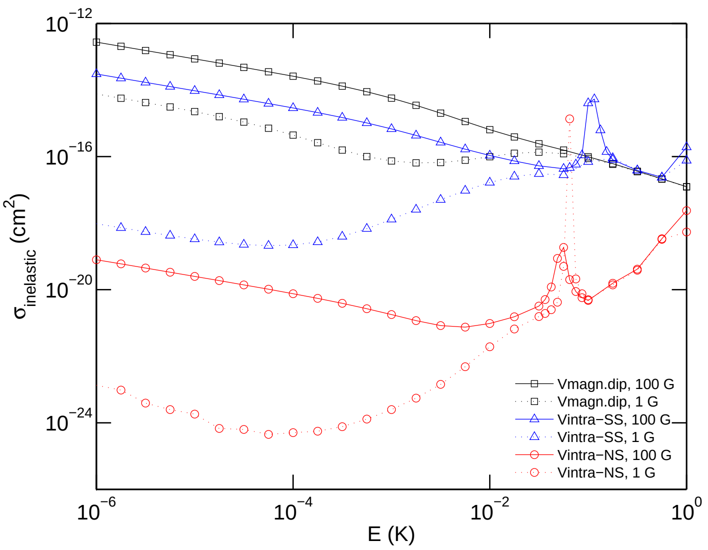

Figure 4.4: Inelastic M_J-changing cross sections for $\mathcal{M} = 2$ as a function of collision energy at 1 G and 100 G. The different curves correspond to calculations with either the intermolecular magnetic dipolar coupling ("$V_{\text{magn.dip}}$"), the intramolecular spin-spin coupling ("$V_{\text{intra-SS}}$"), or the intramolecular spin-rotation coupling ("$V_{\text{intra-NS}}$") included in $\hat{H}$.

In order to identify the main trap-loss mechanism, we have also performed scattering calculations where two of the three spin-dependent coupling terms are set to zero. The results for $\mathcal{M} = 2$ are shown in Figs. 4.4 and 4.5. We have verified that the $\mathcal{M} = 2$ cross sections, in which s-wave collisions in the incident channel are allowed, are dominant at the energies and fields considered in this work. It can be seen that the intermolecular spin-spin interaction ($V_{\text{magn.dip}}$) gives the largest contribution to the inelastic cross section over a broad range of energies and field strengths, most notably in the ultracold regime. This is also the case for cold and ultracold N + NH collisions [61, 65]. At higher collision energies and fields, however, the *intramolecular* coupling terms become increasingly important. In particular the intramolecular spin-spin term causes significant trap loss above $E \approx 10^{-2}$ K and $B \approx 100$ G. Spin-rotation coupling, which vanishes for pure $N_A = N_B = 0$ states, has only a very small effect on the total cross section. This is consistent with previous work on the He–NH($^3\Sigma^-$) system [57, 86, 122].

The importance of the *intermolecular* magnetic dipole interaction is most easily understood by considering the adiabatic potential curves. As discussed in Section 4.3.1, the avoided crossings between the s-wave incoming channel $|M_{J_A} = 1, M_{J_B} = 1, L = 0\rangle$ and the $|M_{S_A} = 1, M_{S_B} = 0, L = 2\rangle$ and $|M_{S_A} = 0, M_{S_B} = 0, L = 2\rangle$ outgoing channels all occur at very long range for small to moderate field strengths. Consequently, the spin-flip induced by $V_{\text{magn.dip}}$ can take place without having to overcome the d-wave barrier in the outgoing channels, and hence this process dominates the inelastic cross section in the ultracold regime. We also emphasize that, if the avoided-crossing points

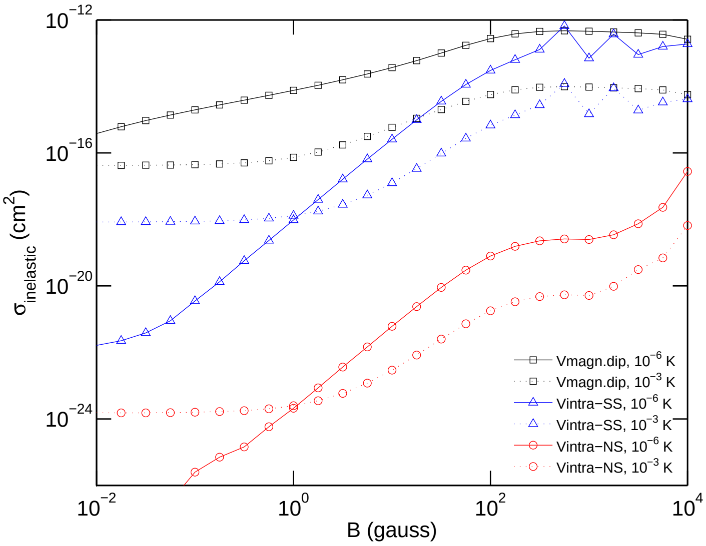

Figure 4.5: Inelastic M_J-changing cross sections for $\mathcal{M} = 2$ as a function of magnetic field at 10^{-6} K and 10^{-3} K. The different curves are obtained from scattering calculations with either the intermolecular magnetic dipolar coupling ("$V_{\text{magn.dip}}$"), the intramolecular spin-spin coupling ("$V_{\text{intra−SS}}$"), or the intramolecular spin-rotation coupling ("$V_{\text{intra−NS}}$") switched on.

R_c fall outside the scattering propagation region, i.e. if the radial grid is chosen too small, the inelastic cross sections are similar to the case where the intermolecular magnetic dipole term is switched off completely. This confirms that the spin-flip due to $V_{\text{magn.dip}}$ indeed takes place at long range, or more specifically, at $R \approx R_c$.

Kajita [89] has shown that, in the Born approximation, the inelastic cross section $\sigma_{i \to f}$ for ^{15}NH $(L_i = 0, L_f = 2)$ caused by the magnetic dipole interaction should be proportional to $B^{1/2}$ and $E^{-1/2}$ if the kinetic energy release is relatively large $(k_i \ll k_f)$. This is consistent with our results obtained from full quantum scattering calculations in the ultracold regime. As the collision energy increases, however, the assumption of $k_i \ll k_f$ breaks down and the cross sections deviate from the $B^{1/2}$ behaviour. We find numerically that this is the case for energies above $\sim 10^{-6}$ K at nearly all the field strengths considered in this work (see Fig. 4.3). In the next chapter, we will give a general analytical expression for the inelastic cross section due to $V_{\text{magn.dip}}$ based on the (distorted-wave) Born approximation, and show that the numerical and analytical results are in excellent agreement over a wide range of energies and fields.

At collision energies above about 10 mK or high magnetic fields, there is sufficient energy to overcome the d-wave centrifugal barrier in the outgoing channels and, as a consequence, short-range effects become important. In particular the *intramolecular* spin-spin coupling term, which requires strong anisotropy of the potential in order to induce Zeeman relaxation [86, 57], enhances the inelastic cross section significantly at energies above $\sim$ 10 mK. For the intramolecular contributions, we find that the inelastic cross section behaves as $B^{5/2}$ at moderate field strengths and flattens off to a constant value at very small B. Its kinetic energy dependence is proportional to $E^{-1/2}$ in the ultracold regime and, for small magnetic fields, also shows a region of E^2 behaviour. This result is consistent with the work of Volpi and Bohn, who applied the distorted-wave Born approximation to calculate inelastic spin-changing collisions induced at short range [123]:

$$\sigma_{i\to f} \propto E^{L_i-1/2}\left(E + g_S\mu_\mathrm{B}B\Delta M_S\right)^{L_f+1/2}. \tag{4.16}$$

Thus, for an s-wave incoming channel ($L_i = 0$) and d-wave outgoing channel ($L_f = 2$), there is a region of E^2 dependence when the Zeeman shift for the outgoing channel is small compared to the collision energy. At very small fields, the magnetic-field dependence is negligible and the cross section becomes constant as a function of B.

We also point out that, in contrast to the *intermolecular* spin-spin coupling term, the *intramolecular* spin-spin interaction contains second-rank tensors in $\hat{S}_A$ and $\hat{S}_B$ and therefore directly couples channels where M_{S_A} and M_{S_B} each differ by 0, 1, *or* 2. Thus, transitions from $M_{S_i} = 1$ to $M_{S_i} = -1$ also become allowed in first order. This is illustrated in Fig. 4.6, where the state-to-state inelastic cross sections for $\mathcal{M} = 2$ are plotted as a function of energy. In the ultracold region, which is dominated by $V_\mathrm{magn.dip}$, only the $|M_{S_A} = 1, M_{S_B} = 1\rangle \to |M_{S_A} = 1, M_{S_B} = 0\rangle$ and $|M_{S_A} = 1, M_{S_B} = 1\rangle \to |M_{S_A} = 0, M_{S_B} = 0\rangle$ transitions contribute to the inelastic cross section. At higher energies, where the intramolecular spin-spin term plays a significant role, transitions from $|M_{S_A} = 1, M_{S_B} = 1, L = 0\rangle$ to the $|M_{S_A} = 1, M_{S_A} = -1, L = 2\rangle$, $|M_{S_A} = 0, M_{S_A} = -1, L = 4\rangle$, and $|M_{S_A} = -1, M_{S_A} = -1, L = 4\rangle$ channels become increasingly important. Note that the latter two have g-wave barriers in the exit channel, and hence they are strongly suppressed in the low-energy regime.

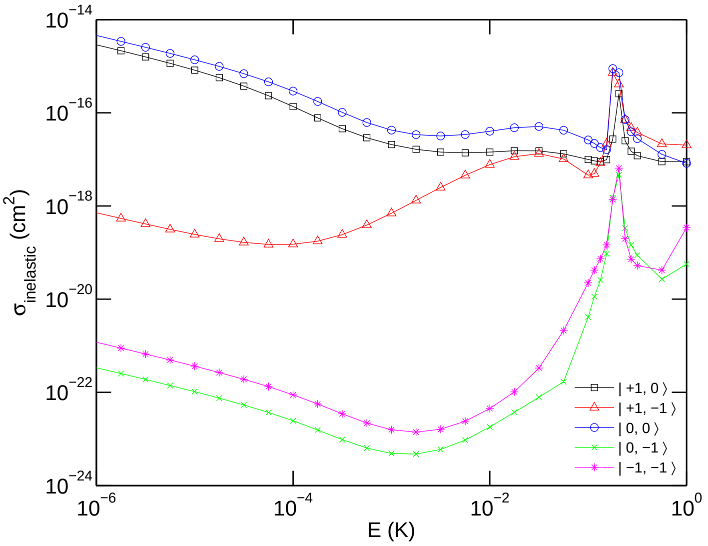

Figure 4.6: State-to-state inelastic cross sections ($\mathcal{M} = 2$) for magnetically trapped ^{15}NH as a function of energy at 1 G. The final states are labeled by $|M_{J_A}, M_{J_B}\rangle$.

In summary, we have established that the dominant trap-loss mechanism for NH in the ultracold regime is the *intermolecular* spin-spin coupling term, which induces Zeeman relaxation at *long range*. When the kinetic energy in the outgoing channel becomes large, the spin-change is also caused by the interplay of the potential anisotropy and the *intramolecular* spin-spin interaction, which acts at *short range*.

4.3.3 Dependence on potential and basis-set size

As a final part of our discussion, we consider the sensitivity to the potential and the dependence on the size of the channel basis set. Previous theoretical work on field-free collisions (Chapter 3) has shown that the NH + NH cross sections at low collision energies are very sensitive to the details of the potential energy surface, which is due to the presence of quasi-bound state resonances. Since the *exact* form of the interaction potential, and thus the precise locations of the quasi-bound states, are still unknown, the calculated cross sections are subject to an inherent degree of uncertainty. The work of the previous chapter showed, however, that the qualitative results and conclusions are reasonably independent of the details of the potential. Furthermore, it was demonstrated that the effect of using an unconverged channel basis set is very similar to a scaling of the potential within its uncertainty. That is, full basis-set convergence is not strictly required in order to obtain qualitatively meaningful results.

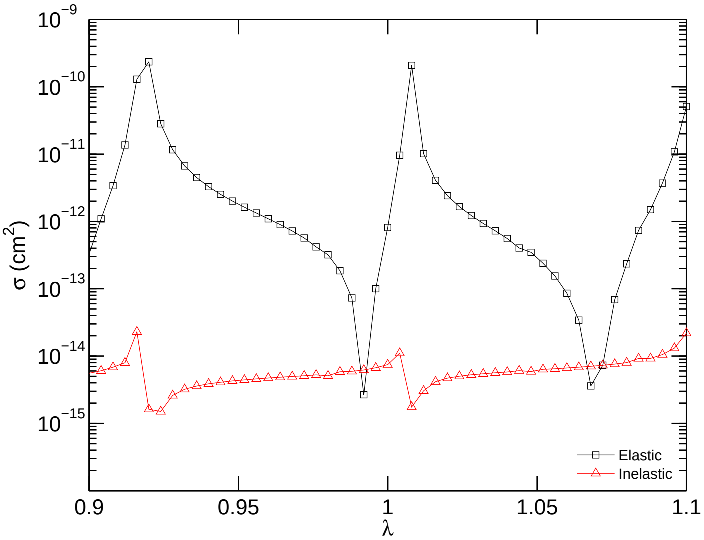

Figure 4.7: Elastic and inelastic M_J-changing cross sections ($\mathcal{M} = 2$) for magnetically trapped ^{15}NH as a function of the scaling factor λ, calculated at a collision energy of 10^{-6} K and a magnetic field strength of 1 G.

Our present work is based on a similar approach. Following Ref. [65] and the work described in Chapter 3, we have studied the potential dependence indirectly by evaluating the sensitivity to the reduced mass. The reduced mass was scaled by a factor of λ ($0.9 \leq \lambda \leq 1.1$), which is essentially equivalent to a scaling of the entire potential by λ [65]. Figure 4.7 shows the $\mathcal{M} = 2$ cross sections for different scaling factors at a collision energy of 10^{-6} K and a field strength of 1 G. We find that the cross sections exhibit resonance structures at certain λ values, indicating a high sensitivity to the potential. However, the ratio between elastic and inelastic cross sections is much less sensitive to the reduced mass, and the prospects for evaporative cooling remain very positive over almost the entire range of λ. The contributions from the different spin-changing mechanisms, as described in the previous section, are also very similar for different reduced masses. Our qualitative results and conclusions are thus reasonably independent of the precise form of the potential.

We use the same scaling method to investigate the dependence on basis-set size. Figure 4.8 shows the $\mathcal{M} = 2$ cross sections as a function of λ for different values of $N_{\max}$ and $L_{\max}$ at $E = 10^{-6}$ K and $B = 1$ G. The total number of channels in these calculations ranged from 901 for $N_{\max} = 2, L_{\max} = 6$ up to 2621 for $N_{\max} = 3, L_{\max} = 6$. It can be seen that the positions of the resonances shift when the basis size is increased, but the general pattern remains essentially the same. This is consistent with other work on NH (see Refs. [65, 66] and Chapter 3). We thus conclude that, within the uncertainty limits of λ, our qualitative results are not very sensitive to the size of the angular basis set.

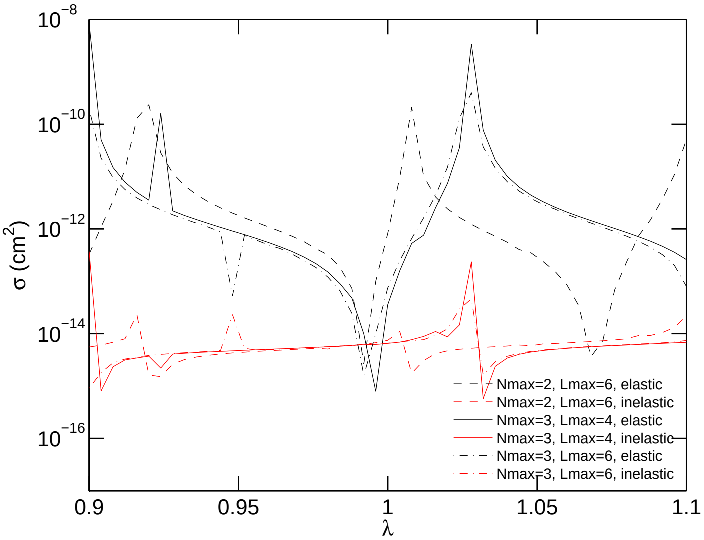

Figure 4.8: Elastic and inelastic M_J-changing cross sections ($\mathcal{M} = 2$) as a function of the scaling factor λ, calculated for different basis sets at a collision energy of 10^{-6} K and a magnetic field strength of 1 G.

Figure 4.8 also demonstrates that the cross sections are not yet converged with respect to $N_{\max}$ and $L_{\max}$. In fact, field-free NH–NH calculations suggest that the basis set should extend to at least $N_{\max} = 6$ and $L_{\max} = 7$ to achieve full convergence (Chapter 3), which would amount to a maximum of 25 598 channels for $\mathcal{M} = 0$ in the present decoupled basis set. Such calculations are highly infeasible with the currently available computer power. However, taking into account the uncertainty in the potential and the pronounced resonance structure, even a fully converged basis set would not give really reliable numerical values. Nonetheless, it must be emphasized that unconverged basis sets can give qualitatively reliable results. As already discussed in (Chapter 3) and Ref. [66], full basis-set convergence is therefore not strictly necessary within the uncertainty limits of the potential.

4.4 Conclusions

We have carried out full quantum scattering calculations to study cold and ultracold ^{15}NH – ^{15}NH collisions in magnetic fields. The elastic and spin-changing cross sections for magnetically trapped NH are found to be very favorable for efficient evaporative cooling. We have identified the *intermolecular* spin-spin coupling term as the main trap-loss mechanism at low energies and small magnetic fields, while the *intramolecular* spin-spin term becomes increasingly important at higher energies and fields. The effect of spin-rotation coupling is almost negligible.

Finally, we have demonstrated that the numerical values of the cross sections are very sensitive to the details of the potential, but the *qualitative* results and conclusions are almost independent of the exact form of the surface. The size of the angular basis set, which is almost impossible to converge for systems such as NH–NH, does not significantly alter the results within the uncertainty limits of the potential. This inherent uncertainty in the calculated cross sections, however, clearly highlights the need for reliable experimental data.

Chapter 5

Magnetic dipole-dipole coupling

The aim of this chapter is to provide a detailed analysis of the role of the magnetic dipole-dipole interaction in cold and ultracold collisions. We focus on collisions between magnetically trapped NH molecules, but the theory is general for any two paramagnetic species for which the electronic spin and its space-fixed projection are (approximately) good quantum numbers. It is shown that dipolar spin relaxation is directly associated with magnetic-dipole induced avoided crossings that occur between different adiabatic potential curves. For a given collision energy and magnetic field strength, the cross-section contributions from different scattering channels depend strongly on whether or not the corresponding avoided crossings are energetically accessible. We find that the crossings become lower in energy as the magnetic field decreases, so that higher partial-wave scattering becomes important *below* a certain magnetic field strength. In addition, we derive analytical cross-section expressions for dipolar spin relaxation based on the Born approximation and distorted-wave Born approximation. The validity regions of these analytical expressions are determined by comparison with the NH + NH cross sections obtained from full coupled-channels calculations. We find that the Born approximation is accurate over a wide range of energies and field strengths, but breaks down at high energies and high magnetic fields. The analytical distorted-wave Born approximation gives more accurate results in the case of s-wave scattering, but shows some significant discrepancies for the higher partial-wave channels. We thus conclude that the Born approximation gives generally more meaningful results than the distorted-wave Born approximation at the collision energies and fields considered in this work.

5.1 Introduction

As described earlier, successful evaporative cooling of atoms or molecules to (near) quantum degeneracy requires a relatively large elastic cross section. Inelastic collisions, in which the internal quantum state of at least one of the collision partners is changed, can induce heating of the gas and trap loss. A detailed understanding of the interparticle interactions that govern these inelastic processes is thus crucial for assessing the feasibility of second-stage cooling. One of the most important inelastic loss mechanisms for trapped paramagnetic species is dipolar spin relaxation, which arises from the magnetic dipole-dipole interaction between the magnetic moments of the particles. For many spin-polarized atomic gases such as hydrogen [53], lithium [124], nitrogen [125], and chromium [126], but also for atom–molecule and molecule–molecule systems such as Li + NH [66], N + NH [61, 65], and NH + NH (see Chapters 3 and 4), the interparticle dipolar spin-spin interaction is indeed the dominant source of trap loss.

In this chapter, we provide a comprehensive study on the role of the magnetic dipolar interaction in cold and ultracold collisions. Specifically, we consider collisions between magnetically trapped bosonic ^{15}NH($X\,^3\Sigma^-$) molecules, but the theory should be general for any (ultra)cold paramagnetic species. We assume that the molecules are in their vibrational and rotational ground states, as is the case experimentally [58]. For NH + NH, there are three spin-changing mechanisms that can induce trap loss: the intramolecular spin-spin and spin-rotation couplings, and the intermolecular magnetic dipolar coupling term [86]. The previous chapter has shown that the intermolecular magnetic dipole interaction is the main spin-relaxation mechanism for NH–NH at low collision energies and small to moderate magnetic field strengths. It was also demonstrated that the dipolar spin-spin coupling term induces certain avoided crossings between different adiabatic potential curves, which in turn give rise to spin-changing transitions. That is, the spin-flip due to the intermolecular magnetic dipolar interaction can be qualitatively understood in terms of the avoided curve crossings. In the present work, we discuss the influence of these crossings on the cross section in much greater detail. We also provide analytical expressions for the dipolar spin-relaxation cross section based on the Born approximation (BA) and distorted-wave Born approximation (DWBA). We compare the analytical results with the cross sections obtained from rigorous close-coupling calculations, and show that the results are in excellent agreement over a wide range of collision energies and magnetic field strengths.

This chapter is organized as follows. In Sec. 5.2.1, we briefly describe the details of the coupled-channels calculations. The derivations of the BA and DWBA cross sections are given in Secs. 5.2.2 and 5.2.3, respectively, and the results are discussed in Sec. 5.3. The numerical results are presented in Sec. 5.3.1, with a particular emphasis on the role of the avoided curve crossings, and the validity of the analytical BA and DWBA cross sections is detailed in Sec. 5.3.2. Finally, concluding remarks are given in Sec. 5.4.

5.2 Theory

Throughout this work, we will focus on collisions between two bosonic ^{15}NH($X\,^3\Sigma^-$) molecules in their magnetically trappable, low-field seeking states $|S_A = 1, M_{S_A} = 1\rangle$ $|S_B = 1, M_{S_B} = 1\rangle$. Here S_i ($i = A, B$) denotes the total electronic spin of the monomers and M_{S_i} is the spin projection onto the magnetic field axis. A collision complex of two such molecules is in the high-spin quintet $|S = 2, M_S = 2\rangle$ state, with S denoting the total spin and M_S its space-fixed projection. Collisions that change either the M_S quantum number of the quintet state or the total spin S to yield singlet ($S = 0$) or triplet ($S = 1$) complexes will lead to immediate trap loss.

5.2.1 Coupled-channels calculations

In order to obtain numerical values for the collision cross sections of NH + NH, we have performed rigorous coupled-channels calculations as a function of energy and magnetic field. The details of these calculations are given in Chapter 4 and we provide only a brief description here. The NH–NH scattering Hamiltonian is written as

$$\hat{H} = -\frac{\hbar^2}{2\mu R}\frac{\partial^2}{\partial R^2}R + \frac{\hat{L}^2}{2\mu R^2} + V(\boldsymbol{R}, \omega_A, \omega_B) + V_{\text{magn.dip}}(\boldsymbol{R}, \hat{\boldsymbol{S}}_A, \hat{\boldsymbol{S}}_B) + \hat{H}_A + \hat{H}_B, \quad (5.1)$$

where μ is the reduced mass of the complex, $\boldsymbol{R}$ is the intermolecular vector that connects the centers of mass of the monomers, $R = |\boldsymbol{R}|$, $\hat{L}^2$ is the angular momentum operator associated with rotation of $\boldsymbol{R}$, $V(\boldsymbol{R}, \omega_A, \omega_B)$ is the potential energy surface for the quintet ($S = 2$) state of NH–NH, ω_A and ω_B describe the orientation of monomers A and B, $V_{\text{magn.dip}}(\boldsymbol{R}, \hat{\boldsymbol{S}}_A, \hat{\boldsymbol{S}}_B)$ is the intermolecular magnetic dipolar interaction between the two spins, and $\hat{H}_A$ and $\hat{H}_B$ are the Hamiltonians of the individual monomers. The magnetic dipole-dipole term is given by

$$V_{\text{magn.dip}}(\boldsymbol{R}, \hat{\boldsymbol{S}}_A, \hat{\boldsymbol{S}}_B) = -\sqrt{6}g_S^2\mu_{\text{B}}^2\frac{\alpha^2}{R^3}\sum_q(-1)^q C_{2,-q}(\Omega_R)[\hat{\boldsymbol{S}}_A \otimes \hat{\boldsymbol{S}}_B]^{(2)}_q, \quad (5.2)$$

where $g_S \approx 2.0023$ is the electron g-factor, μ_{B} is the Bohr magneton, α is the fine-structure constant, $C_{2,-q}$ is a Racah-normalized spherical harmonic, $\Omega_R = (\Theta_R, \Phi_R)$ describes the orientation of $\boldsymbol{R}$, and the factor in square brackets is the tensor product of the monomer spin operators $\hat{\boldsymbol{S}}_A$ and $\hat{\boldsymbol{S}}_B$. The monomer operators $\hat{H}_i$ correspond to the asymptotic molecular states and account for the monomer rotation, intramolecular spin-spin coupling, spin-rotation coupling, and Zeeman interaction. Hyperfine coupling is neglected.

The scattering calculations were carried out in a symmetry-adapted basis set that accounts for the identical-particle symmetry of the system,

$$|\phi^{\eta,\epsilon}_{\gamma_A\gamma_B L M_L}\rangle = \frac{1}{[2(1+\delta_{\gamma_A\gamma_B})]^{1/2}}\left[|\gamma_A\gamma_B\rangle + \eta(-1)^L|\gamma_B\gamma_A\rangle\right]|LM_L\rangle. \quad (5.3)$$

Here η defines the symmetry of the wave function with respect to molecular interchange, which is +1 for the bosonic ^{15}NH – ^{15}NH complex, $\epsilon = (-1)^{N_A+N_B+L}$ is the parity symmetry, which must be +1 for identical bosons in the same quantum state, and $|\gamma_A, \gamma_B\rangle$ denotes the molecular rotation and spin functions in the space-fixed frame [86],

$$|\gamma_A \gamma_B\rangle \equiv |N_A M_{N_A}\rangle |S_A M_{S_A}\rangle |N_B M_{N_B}\rangle |S_B M_{S_B}\rangle. \tag{5.4}$$

The basis set was truncated at $N_A = N_B = 2$ and $L = 6$. Although this basis set is not fully converged, we have verified that the calculated cross sections are very similar to those obtained with $N_A = N_B = 3$ in the region where the intermolecular dipole-dipole coupling is dominant, i.e. at ultralow energies and small to moderate field strengths. Increasing the rotational basis set does yield a larger cross-section contribution from the *intramolecular* spin-spin coupling, but this term becomes important only at energies above ∼1 mK and fields above ∼100 G. For a more general discussion on the issue of basis-set convergence, the reader is referred to Secs. 3.3.3 and 4.3.3.

Let us now consider the identical-particle symmetry of the complex. Even though hyperfine coupling is neglected, the symmetry of the nuclear-spin wave function should be taken into account when evaluating the exchange symmetry of the total wave function. We have assumed that both monomers are in their nuclear-spin stretched states ($I = M_I = 1$), so that the nuclear-spin function is symmetric under exchange. Thus, we have $\eta = +1$ and $\epsilon = +1$. We also point out that, due to parity conservation, collisions between rotational ground-state molecules can only occur for *even* values of L. Furthermore, the conservation of the total angular momentum projection $\mathcal{M} = M_{N_A} + M_{N_B} + M_{S_A} + M_{S_B} + M_L$ requires that any change in M_{S_A} or M_{S_B} must be accompanied by a change in M_L. It therefore follows that, in the ultracold regime, the s-wave spin-inelastic collision channel for magnetically trapped, rotational ground-state NH is dominated by the $L = 2$ outgoing partial wave.

We performed the scattering calculations for each value of $\mathcal{M}$ and accumulated the resulting scattering S-matrices to extract the cross sections. The calculations were carried out using a modified version of the MOLSCAT package [116, 117]. The propagation was performed using the hybrid log-derivative method of Alexander and Manolopoulos [80]. Prior to matching to asymptotic boundary conditions, an additional transformation was required to obtain the exact channel eigenfunctions [86]. This is because the intramolecular spin-spin coupling mixes states with N_i and $N_i \pm 2$, which makes N_i, M_{N_i}, and M_{S_i} only approximately good quantum numbers. The *exact* molecular eigenstates will be denoted as

$$|\bar{\gamma}_A \bar{\gamma}_B\rangle \equiv |(\bar{N}_A, S_A) J_A, M_{J_A}\rangle |(\bar{N}_B, S_B) J_B, M_{J_B}\rangle. \tag{5.5}$$

We emphasize that the intramolecular coupling is relatively weak and N_i, M_{N_i}, and M_{S_i} may be treated as almost exact. Specifically, for the rotational ground state of ^{15}NH, the magnetically trapped component with $J_i = M_{J_i} = 1$ contains 99.992% of $|N_i = 0, M_{N_i} = 0, S_i = 1, M_{S_i} = 1\rangle$.

5.2.2 Born approximation

In this section, we derive an analytical expression for the inelastic spin-changing cross section due to $V_{\text{magn.dip}}$ based on the first-order Born approximation. This approximation assumes that the interaction between projectile and target is so weak that the initial and final states can be described by undistorted plane waves. We note that the BA has been previously used in the study of cold collisions in e.g. Refs. [127, 128, 89, 129]. The aim of the present work is to give a cross-section expression in closed form, and we therefore outline the complete derivation for the sake of clarity. The derived expression is general for any two paramagnetic species for which the electronic spin and its space-fixed projection are (approximately) good quantum numbers, e.g. for Hund's case (b) molecules and S-state atoms, but we will apply it only to the case of NH($^3\Sigma^-$) + NH($^3\Sigma^-$).

We start with the exact expression for the differential cross section (see e.g. Eq. XIX.19 of Ref. [130]),

$$\frac{d\sigma_{a\to b}(\Omega_a)}{d\Omega_b} = \frac{2\pi}{\hbar v_a}\left|\left\langle \boldsymbol{k}_b, \bar{\gamma}_A^{(b)}, \bar{\gamma}_B^{(b)}\right| V_{\text{int}} \left|\boldsymbol{k}_a^{(+)}, \bar{\gamma}_A^{(a)}, \bar{\gamma}_B^{(a)}\right\rangle\right|^2 \rho_b(E), \tag{5.6}$$

where a and b label the initial and final states, respectively, $\Omega_a = (\theta_{k_a}, \phi_{k_a})$ and $\Omega_b = (\theta_{k_b}, \phi_{k_b})$ describe the directions of the incoming and outgoing collision fluxes, $\boldsymbol{k}_a^{(+)}$ is the exact incident wave function with wavenumber k_a, $\boldsymbol{k}_b$ is a plane wave with wavenumber k_b, $\bar{\gamma}_A^{(i)}$ and $\bar{\gamma}_B^{(i)}$ denote the internal quantum numbers of the monomers for the initial and final states ($i = a, b$), V_{int} is the interaction between the scattering particles, for which we take $V_{\text{int}} = V_{\text{magn.dip}}$, $v_a = \hbar k_a/\mu$ is the velocity of the incident beam, and $\rho_b(E) = \mu k_b/[\hbar^2(2\pi)^3]$ is the density of final states at energy $E = \frac{1}{2}\mu v_a^2$. The first-order Born approximation amounts to approximating the incident wave function as a plane wave, i.e. $|\boldsymbol{k}_a^{(+)}\rangle \approx |\boldsymbol{k}_a\rangle$. The plane waves are normalized to unit density and are mutually orthogonal,

$$|\boldsymbol{k}\rangle = e^{i\boldsymbol{k}\cdot\boldsymbol{R}}, \tag{5.7}$$

$$\langle\boldsymbol{k}|\boldsymbol{k}'\rangle = (2\pi)^3\delta(\boldsymbol{k}-\boldsymbol{k}'). \tag{5.8}$$

Here $\delta(\boldsymbol{k}-\boldsymbol{k}')$ represents the three-dimensional Dirac delta function.

In the case of NH + NH, the asymptotic states $\bar{\gamma}_A^{(i)}$ and $\bar{\gamma}_B^{(i)}$ should be described as in Eq. (5.5). However, since we focus on collisions between rotational ground-state molecules, we may treat M_{S_A} and M_{S_B} as almost exact quantum numbers. Furthermore, taking into account that $V_{\text{magn.dip}}$ acts only on the vector $\boldsymbol{R}$ and the electron-spin coordinates, we can omit the molecular rotational quantum numbers and write

$$\begin{aligned} \left|\bar{\gamma}_A^{(i)}\right\rangle &\approx \left|S_A M_{S_A}^{(i)}\right\rangle, \\ \left|\bar{\gamma}_B^{(i)}\right\rangle &\approx \left|S_B M_{S_B}^{(i)}\right\rangle. \end{aligned} \tag{5.9}$$

The energies of the initial and final molecular states are now determined only by their Zeeman shifts. If we define the Zeeman levels relative to the initial state, the wavenumbers are $k_a = \sqrt{2\mu E}/\hbar$ and $k_b = \sqrt{2\mu(E + g_S\mu_\mathrm{B}\Delta M_S B)}/\hbar$, where ΔM_S is the total spin-change, $\Delta M_S = M_{S_A}^{(a)} + M_{S_B}^{(a)} - M_{S_A}^{(b)} - M_{S_B}^{(b)}$, the term $g_S\mu_\mathrm{B}\Delta M_S B$ is the corresponding change in Zeeman energy, and B is the magnetic field strength. In the remainder of this chapter, we will use B exclusively to indicate the magnetic field strength, while the subscript B is used to label the quantum numbers of monomer B.

The plane waves can be expanded in terms of partial waves as

$$e^{i\boldsymbol{k}\cdot\boldsymbol{R}} = 4\pi \sum_{L=0}^{\infty} \sum_{M=-L}^{L} i^L j_L(kR) Y_{L,M}(\Theta_R, \Phi_R) Y_{L,M}^*(\theta_k, \phi_k), \tag{5.10}$$

where $j_L(kR)$ is a spherical Bessel function of the first kind, the $Y_{L,M}$ functions are spherical harmonics, and the superscript * denotes complex conjugation. If we now substitute Eq. (5.2) for the particle interaction and use Eq. (5.9) to describe the molecular asymptotic states, we obtain

$$\begin{aligned}\big\langle \boldsymbol{k}_b, \bar{\gamma}_A^{(b)}, \bar{\gamma}_B^{(b)} \big| V_{\mathrm{magn.dip}} \big| \boldsymbol{k}_a, \bar{\gamma}_A^{(a)}, \bar{\gamma}_B^{(a)} \big\rangle &= -4\pi\sqrt{6} g_S^2 \mu_\mathrm{B}^2 \alpha^2 \sum_{L_a}\sum_{L_b} i^{L_a - L_b} \\ &\times \sum_{M_b} Y_{L_b,M_b}(\Omega_b) \sum_{M_a} Y_{L_a,M_a}^*(\Omega_a) \sum_q (-1)^q \int_R j_{L_b}(k_b R) \frac{1}{R^3} j_{L_a}(k_a R) R^2 dR \\ &\times \int_{\Omega_R} Y_{L_b,M_b}^*(\Omega_R) C_{2,-q}(\Omega_R) Y_{L_a,M_a}(\Omega_R) d\Omega_R \\ &\times \big\langle S_A M_{S_A}^{(b)}, S_B M_{S_B}^{(b)} \big| [\hat{\boldsymbol{S}}_A \otimes \hat{\boldsymbol{S}}_B]_q^{(2)} \big| S_A M_{S_A}^{(a)}, S_B M_{S_B}^{(a)} \big\rangle, \end{aligned} \tag{5.11}$$

where the last factor represents an integral over the spin coordinates. The integral over R can be performed analytically and gives, for $k_a \leq k_b$ (see also Ref. [128]),

$$\begin{aligned}\int j_{L_b}(k_b R) \frac{1}{R} j_{L_a}(k_a R) dR &= \frac{\pi}{8} \left(\frac{k_a}{k_b}\right)^{L_a} \\ &\times \frac{\Gamma\left(\frac{L_a+L_b}{2}\right)}{\Gamma\left(\frac{L_b-L_a+3}{2}\right)\Gamma\left(L_a+\frac{3}{2}\right)} \\ &\times {}_2F_1\left(\frac{L_a-L_b-1}{2}, \frac{L_a+L_b}{2}, L_a+\frac{3}{2}, \frac{k_a^2}{k_b^2}\right), \end{aligned} \tag{5.12}$$

where Γ is the Gamma function and ${}_2F_1$ is Gauss' hypergeometric function. The integral over Ω_R gives

$$\begin{aligned}&\int_{\Omega_R} Y_{L_b,M_b}^*(\Omega_R) C_{2,-q}(\Omega_R) Y_{L_a,M_a}(\Omega_R) d\Omega_R = \\ &\qquad \sqrt{(2L_a+1)(2L_b+1)}(-1)^{M_b} \begin{pmatrix} L_b & 2 & L_a \\ 0 & 0 & 0 \end{pmatrix} \begin{pmatrix} L_b & 2 & L_a \\ -M_b & -q & M_a \end{pmatrix}, \end{aligned} \tag{5.13}$$

with the terms in large round brackets denoting Wigner $3j$ symbols. The last $3j$ symbol readily implies that $q = M_a - M_b$. Finally, for the spin-dependent term we find

$$\begin{aligned}
&\langle S_A M_{S_A}^{(b)}, S_B M_{S_B}^{(b)} | [\hat{\boldsymbol{S}}_A \otimes \hat{\boldsymbol{S}}_B]_q^{(2)} | S_A M_{S_A}^{(a)}, S_B M_{S_B}^{(a)} \rangle = \\
&\quad \sqrt{5}(-1)^{q+S_A+S_B-M_{S_A}^{(b)}-M_{S_B}^{(b)}} [S_A(S_A+1)(2S_A+1)S_B(S_B+1)(2S_B+1)]^{1/2} \\
&\quad \times \sum_{m_A,m_B} \begin{pmatrix} 1 & 1 & 2 \\ m_A & m_B & -q \end{pmatrix} \begin{pmatrix} S_A & 1 & S_A \\ -M_{S_A}^{(b)} & m_A & M_{S_A}^{(a)} \end{pmatrix} \begin{pmatrix} S_B & 1 & S_B \\ -M_{S_B}^{(b)} & m_B & M_{S_B}^{(a)} \end{pmatrix} \qquad (5.14)
\end{aligned}$$

Note that the sums over m_A and m_B collapse for given values of $M_{S_A}^{(i)}$ and $M_{S_B}^{(i)}$, since the last two $3j$ symbols require that $m_A = M_{S_A}^{(b)} - M_{S_A}^{(a)}$ and $m_B = M_{S_B}^{(b)} - M_{S_B}^{(a)}$. Furthermore, we have $m_A + m_B = q$ so that $M_b - M_a = M_{S_A}^{(a)} + M_{S_B}^{(a)} - M_{S_A}^{(b)} - M_{S_B}^{(b)} = \Delta M_S$. The sums over M_a, M_b and q in Eq. (5.11) therefore reduce to a single sum for any individual matrix element. The differential cross section is now readily calculated by substituting Eqs. (5.11) – (5.14) into Eq. (5.6).

The integral cross section is obtained by integrating $d\sigma_{a\to b}/d\Omega_b$ over all orientations of the outgoing wave and averaging over all directions of the incoming collision flux,

$$\sigma_{a\to b}(E) = \frac{1}{4\pi} \int_{\Omega_a} d\Omega_a \int_{\Omega_b} \frac{d\sigma_{a\to b}(\Omega_a)}{d\Omega_b} d\Omega_b. \qquad (5.15)$$

Using the orthogonality relation $\int Y_{L,M}^*(\Omega) Y_{L',M'}(\Omega) d\Omega = \delta_{L,L'}\delta_{M,M'}$, we find the following expression for the BA cross section for $|S_A M_{S_A}^{(a)}, S_B M_{S_B}^{(a)}\rangle \to |S_A M_{S_A}^{(b)}, S_B M_{S_B}^{(b)}\rangle$ transitions induced by $V_{\text{magn.dip}}$:

$$\begin{aligned}
\sigma_{a\to b}^{\text{BA}}(E) = {} & \frac{15\pi^3}{2\hbar^4} \mu^2 g_S^4 \mu_{\text{B}}^4 \alpha^4 \sum_{L_a} \sum_{L_b} (2L_a+1)(2L_b+1) \left(\frac{k_a}{k_b}\right)^{2L_a-1} \\
& \times S_A(S_A+1)(2S_A+1)S_B(S_B+1)(2S_B+1) \\
& \times \left[\frac{\Gamma\left(\frac{L_a+L_b}{2}\right)}{\Gamma\left(\frac{L_b-L_a+3}{2}\right)\Gamma\left(L_a+\frac{3}{2}\right)} \right]^2 \\
& \times \left[{}_2F_1\left(\frac{L_a-L_b-1}{2}, \frac{L_a+L_b}{2}, L_a+\frac{3}{2}, \frac{k_a^2}{k_b^2} \right) \right]^2 \\
& \times \sum_{M_a} \begin{pmatrix} L_b & 2 & L_a \\ -(M_a+\Delta M_S) & \Delta M_S & M_a \end{pmatrix}^2 \\
& \times \left[\begin{pmatrix} L_b & 2 & L_a \\ 0 & 0 & 0 \end{pmatrix} \begin{pmatrix} 1 & 1 & 2 \\ \Delta M_{S_A} & \Delta M_{S_B} & \Delta M_S \end{pmatrix} \right]^2 \\
& \times \left[\begin{pmatrix} S_A & 1 & S_A \\ -M_{S_A}^{(b)} & \Delta M_{S_A} & M_{S_A}^{(a)} \end{pmatrix} \begin{pmatrix} S_B & 1 & S_B \\ -M_{S_B}^{(b)} & \Delta M_{S_B} & M_{S_B}^{(a)} \end{pmatrix} \right]^2, \qquad (5.16)
\end{aligned}$$

with $\Delta M_{S_A} = M_{S_A}^{(b)} - M_{S_A}^{(a)}$ and $\Delta M_{S_B} = M_{S_B}^{(b)} - M_{S_B}^{(a)}$. The cross section for a specific incoming partial wave L_a and a certain outgoing wave L_b is obtained by simply omitting the sums over L_a and L_b. We also point out that in the limit of $k_a \ll k_b$, which holds for ultracold exothermic collisions, the hypergeometric function ${}_2F_1$ becomes 1 (see e.g. Eq. 15.1.1 of Ref. [131]) and the energy dependence of the cross section is $\sigma_{a\to b} \sim k_a^{2L_a-1} \sim E^{L_a-1/2}$. The cross-section behaviour as a function of B is then, for $B \gg E/(g_S\mu_{\rm B}\Delta M_S)$, $\sigma_{a\to b} \sim k_b^{1-2L_a} \sim B^{1/2-L_a}$. Note that this B-dependence is different from the threshold law derived by Volpi and Bohn [123]. They considered the case of spin-changing transitions induced *inside* the centrifugal barrier of the exit channel, and found that the cross section behaves as $\sigma_{a\to b} \sim B^{L_b+1/2}$. In our case, however, the spin-flip takes place at long range, *outside* the centrifugal barrier, and hence we find a different result. The long-range mechanism for dipolar spin relaxation will be addressed in detail in Sec. 5.3.1.

Equation (5.16) is valid for any paramagnetic species that can be represented as in Eq. (5.9). We note that, in the case of identical particles, the cross section must be multiplied by a factor of 2 if both monomers are in the same initial state, i.e. if $M_{S_A}^{(a)} = M_{S_B}^{(a)}$ (see e.g. Appendix B of Ref. [87]). This also applies to collisions between two magnetically trapped NH molecules, for which $M_{S_A}^{(a)} = M_{S_B}^{(a)} = 1$.

5.2.3 Analytical distorted-wave Born approximation

As will be shown in Sec. 5.3, the first-order BA is very accurate at low collision energies, but starts to deviate from the coupled-channels result at high energies and strong magnetic fields. One of the causes for this discrepancy is the phase shift in the incoming scattering channel. In order to quantify this effect, we have developed an analytical distorted-wave Born approximation in which the phase shift in the incident plane wave is explicitly included.

Our starting point for the analytical DWBA is again Eq. (5.6), but now we approximate the incoming wave function $|\boldsymbol{k}_a^{(+)}\rangle$ as an elastically distorted wave $|\boldsymbol{k}'_a\rangle$,

$$|\boldsymbol{k}'_a\rangle = 4\pi \sum_{L_a}\sum_{M_a} i^{L_a}\frac{1}{2}\big[h_{L_a}^{(2)}(k_aR) + S_{aa}^{(M_a)}h_{L_a}^{(1)}(k_aR)\big]Y_{L_a,M_a}(\Theta_R,\Phi_R)Y^*_{L_a,M_a}(\theta_{k_a},\phi_{k_a}), \tag{5.17}$$

where $h_{L_a}^{(1)}$ and $h_{L_a}^{(2)}$ are spherical Hankel functions of the first and second kind, respectively, and $S_{aa}^{(M_a)}$ is the elastic S-matrix element that contains the phase shift for the incident scattering channel $|S_AM_{S_A}^{(a)}, S_BM_{S_B}^{(a)}, L_a, M_a\rangle$. The $S_{aa}^{(M_a)}$ matrix elements for NH–NH are taken from the full coupled-channels calculations described in Sec. 5.2.1. The Hankel functions are defined in terms of regular and irregular spherical Bessel functions as

$$\begin{aligned} h_L^{(1)}(z) &= j_L(z) + iy_L(z), \\ h_L^{(2)}(z) &= j_L(z) - iy_L(z), \end{aligned} \tag{5.18}$$

where $y_L(z)$ is a spherical Bessel function of the second kind. We note that the wave function of Eq. (5.17) is unphysically divergent at the origin for nonzero phase shifts

($S_{aa}^{(M_a)} \neq 1$), but matches the (exact) coupled-channels wave function at sufficiently large R. Hence, the approximation of $|\boldsymbol{k}_a^{(+)}\rangle \approx |\boldsymbol{k}'_a\rangle$ constitutes an improvement over the first-order BA if the coupling occurs at long range.

The radial part of Eq. (5.17) may also be written in terms of the transmission matrix element $T_{aa}^{(M_a)} = 1 - S_{aa}^{(M_a)}$,

$$\begin{aligned}\frac{1}{2}\left[h_{L_a}^{(2)}(k_aR) + S_{aa}h_{L_a}^{(1)}(k_aR)\right] &= \frac{1}{2}\left[h_{L_a}^{(2)}(k_aR) + h_{L_a}^{(1)}(k_aR) - T_{aa}^{(M_a)}h_{L_a}^{(1)}(k_aR)\right] \\ &= j_{L_a}(k_aR) - \frac{1}{2}T_{aa}^{(M_a)}h_{L_a}^{(1)}(k_aR). \qquad (5.19)\end{aligned}$$

Substitution of Eqs. (5.17) and (5.19) into (5.11) for the matrix element over $V_{\text{magn.dip}}$ gives a radial integral of the form

$$\int j_{L_b}(k_bR)\frac{1}{R}j_{L_a}(k_aR)dR - \frac{1}{2}T_{aa}^{(M_a)}\int j_{L_b}(k_bR)\frac{1}{R}h_{L_a}^{(1)}(k_aR)dR. \qquad (5.20)$$

Note that the first integral is identical to that of Eq. (5.12). Using Eq. (5.18), we may write the second integral of Eq. (5.20) as

$$\begin{aligned}&\int j_{L_b}(k_bR)\frac{1}{R}h_{L_a}^{(1)}(k_aR)dR = \\ &\qquad \int j_{L_b}(k_bR)\frac{1}{R}j_{L_a}(k_aR)dR + i\int j_{L_b}(k_bR)\frac{1}{R}y_{L_a}(k_aR)dR. \qquad (5.21)\end{aligned}$$

Again we observe that the first integral on the right-hand side is given by Eq. (5.12). The second integral on the right-hand side is convergent only for $L_b > L_a + 1$ and gives, for $k_a < k_b$ and integer L_a and L_b,

$$\begin{aligned}\int j_{L_b}(k_bR)\frac{1}{R}y_{L_a}(k_aR)dR = &\frac{-1}{8}\left(\frac{k_b}{k_a}\right)^{L_a+1} \\ &\times\frac{\Gamma\left(L_a+\frac{1}{2}\right)\Gamma\left(\frac{L_b-L_a-1}{2}\right)}{\Gamma\left(\frac{L_a+L_b+4}{2}\right)} \\ &\times {}_2F_1\left(\frac{-L_a-L_b-2}{2}, \frac{L_b-L_a-1}{2}, \frac{1}{2}-L_a, \frac{k_a^2}{k_b^2}\right). \qquad (5.22)\end{aligned}$$

We can now replace the radial integral in Eq. (5.11) by the expression of Eq. (5.20) to obtain the matrix element over $V_{\text{magn.dip}}$ in our distorted-wave Born approximation. Substitution into Eq. (5.6) gives the differential DWBA cross section, and Eq. (5.15) subsequently yields the integral cross section. The final expression for the DWBA spin-inelastic cross section due to $V_{\mathrm{magn.dip}}$ is

$$
\begin{aligned}
\sigma^{\mathrm{DWBA}}_{a\to b}(E) = {} & \frac{15\pi}{2\hbar^4}\mu^2 g_S^4 \mu_{\mathrm{B}}^4 \alpha^4 \sum_{L_a}\sum_{L_b}(2L_a+1)(2L_b+1)\frac{k_b}{k_a} \\
& \times S_A(S_A+1)(2S_A+1)S_B(S_B+1)(2S_B+1) \\
& \times \sum_{M_a}\Bigg|\left(1-\frac{1}{2}T_{aa}^{(M_a)}\right)\pi\left(\frac{k_a}{k_b}\right)^{L_a}\frac{\Gamma\left(\frac{L_a+L_b}{2}\right)}{\Gamma\left(\frac{L_b-L_a+3}{2}\right)\Gamma\left(L_a+\frac{3}{2}\right)} \\
& \times {}_2F_1\left(\frac{L_a-L_b-1}{2},\frac{L_a+L_b}{2},L_a+\frac{3}{2},\frac{k_a^2}{k_b^2}\right)+i\frac{1}{2}T_{aa}^{(M_a)}\left(\frac{k_b}{k_a}\right)^{L_a+1} \\
& \times \frac{\Gamma\left(L_a+\frac{1}{2}\right)\Gamma\left(\frac{L_b-L_a-1}{2}\right)}{\Gamma\left(\frac{L_a+L_b+4}{2}\right)}{}_2F_1\left(\frac{-L_a-L_b-2}{2},\frac{L_b-L_a-1}{2},\frac{1}{2}-L_a,\frac{k_a^2}{k_b^2}\right)\Bigg|^2 \\
& \times \begin{pmatrix} L_b & 2 & L_a \\ -(M_a+\Delta M_S) & \Delta M_S & M_a \end{pmatrix}^2 \\
& \times \left[\begin{pmatrix} L_b & 2 & L_a \\ 0 & 0 & 0 \end{pmatrix}\begin{pmatrix} 1 & 1 & 2 \\ \Delta M_{S_A} & \Delta M_{S_B} & \Delta M_S \end{pmatrix}\right]^2 \\
& \times \left[\begin{pmatrix} S_A & 1 & S_A \\ -M_{S_A}^{(b)} & \Delta M_{S_A} & M_{S_A}^{(a)} \end{pmatrix}\begin{pmatrix} S_B & 1 & S_B \\ -M_{S_B}^{(b)} & \Delta M_{S_B} & M_{S_B}^{(a)} \end{pmatrix}\right]^2 .
\end{aligned}
\tag{5.23}
$$

The BA result of Eq. (5.16) is recovered in the limit of $T_{aa}^{(M_a)} \to 0$. We emphasize that, in contrast to the BA, the sums over L_a and L_b in our DWBA expression should be restricted such that $L_b > L_a + 1$ [see Eq. (5.22)]. We also note again that, for indistinguishable particles such as NH + NH, the cross section must be multiplied by 2 if the monomers are in the same initial state.

5.3 Results and discussion

5.3.1 Numerical results

We first discuss the numerical results for NH–NH obtained from the close-coupling calculations. The work of Chapter 4 has shown that the intermolecular magnetic dipole interaction is the dominant trap-loss mechanism for NH–NH at low collision energies and small magnetic fields, while at higher energies and fields the intramolecular couplings become increasingly important. Here we will address only the intermolecular coupling term and provide a careful analysis of its contribution to the total inelastic cross section.

As explained in Chapter 4, the contribution from $V_{\mathrm{magn.dip}}$ is most easily understood by considering the adiabatic potential curves. We will repeat part of this discussion here for the sake of clarity. Asymptotically, the adiabatic curves correspond to the molecular eigenstates $\bar{\gamma}_A$ and $\bar{\gamma}_B$, and at finite R each curve also contains a centrifugal barrier (see Fig. 4.1). Thus, at long range, the adiabats can be labeled by $|\bar{\gamma}_A, \bar{\gamma}_B\rangle$ and L, and therefore also correlate to scattering channels. It has already been noted in Chapter 4 and Ref. [66] that several adiabatic curves are narrowly avoided due to the intermolecular magnetic dipole interaction, and that the spin-flip induced by $V_{\rm magn.dip}$ takes place at the corresponding crossing. If we neglect the weak intramolecular spin-spin and spin-rotation couplings so that Eq. (5.9) holds, we can define the avoided-crossing points R_c as

$$g_S \mu_{\rm B} B \Delta M_S = \frac{\hbar^2 \left[L_b(L_b+1) - L_a(L_a+1)\right]}{2\mu R_c^2}, \qquad (5.24)$$

where L_a and L_b denote the values of L for the adiabats correlating to the incoming and outgoing channels, respectively. The energies at which the crossings occur are given by

$$E_c = \frac{\hbar^2 L_a(L_a+1)}{2\mu R_c^2}, \qquad (5.25)$$

defined relative to the threshold of the incident channel. We must point out that, since $V_{\rm magn.dip}$ contains a second-rank tensor in Ω_R and first-rank tensors in the monomer spin coordinates, the avoided crossings occur only if L_a and L_b differ at most by 2 and $M_{S_i}^{(a)}$ and $M_{S_i}^{(b)}$ $(i = A, B)$ each differ at most by 1. Thus, not all crossings are avoided.

It can be deduced from Eq. (5.24) that, for small to moderate field strengths, the crossing points R_c are located at very long range. Therefore, the spin-change due to $V_{\rm magn.dip}$ can occur without having to overcome the centrifugal barrier in the outgoing channel. More specifically, the $|M_{S_A} = M_{S_B} = 1, L_a = 0\rangle$ incident channel of NH–NH can couple with the $|M_{S_A} = 1, M_{S_B} = 0, L_b = 2\rangle$ and $|M_{S_A} = M_{S_B} = 0, L_b = 2\rangle$ outgoing channels even at zero collision energy. Hence, at low energies and relatively low magnetic fields, the intermolecular magnetic dipolar interaction is the main source of trap loss for NH–NH.

It also follows from Eqs. (5.24) and (5.25) that the curve crossings for higher partial waves, e.g. for the $|M_{S_A} = M_{S_B} = 1, L_a = 2\rangle \rightarrow |M_{S_A} = M_{S_B} = 0, L_b = 4\rangle$ transition, become *lower* in energy as the magnetic field *decreases*. This implies that, at a fixed collision energy, the $L_a = 2 \rightarrow L_b = 4$ channel transitions open up *below* a certain B-value. We will denote this critical magnetic field strength as B_c. Figures 5.1 and 5.2 show the state-to-state inelastic NH–NH cross sections for different $L_a \rightarrow L_b$ channel transitions as a function of B at collision energies of 10^{-6} K and 10^{-3} K, respectively. The B_c values for the $L_a = 2 \rightarrow L_b = 4$ and $L_a = 4 \rightarrow L_b = 6$ crossings are also indicated. For the $|M_{S_A} = M_{S_B} = 1\rangle \rightarrow |M_{S_A} = M_{S_B} = 0\rangle$ transitions, with $\Delta M_S = 2$, the numerical values are $B_c = 8.67 \times 10^{-3}$ G at 10^{-6} K and $B_c = 4.09 \times 10^{-3}$ G at 10^{-3} K for $L_a = 2 \rightarrow L_b = 4$, and $B_c = 8.67$ G at 10^{-6} K and $B_c = 4.09$ G at 10^{-3} K for $L_a = 4 \rightarrow L_b = 6$. The critical field strengths for the $|M_{S_A} = M_{S_B} = 1\rangle \rightarrow |M_{S_A} = 1, M_{S_B} = 0\rangle + |M_{S_A} = 0, M_{S_B} = 1\rangle$ transitions, with $\Delta M_S = 1$, are twice as large as those for $\Delta M_S = 2$. It can be seen that the inelastic cross sections for $L_a = 2 \rightarrow L_b = 4$ and $L_a = 4 \rightarrow L_b = 6$ indeed decrease as B exceeds the corresponding B_c value. This

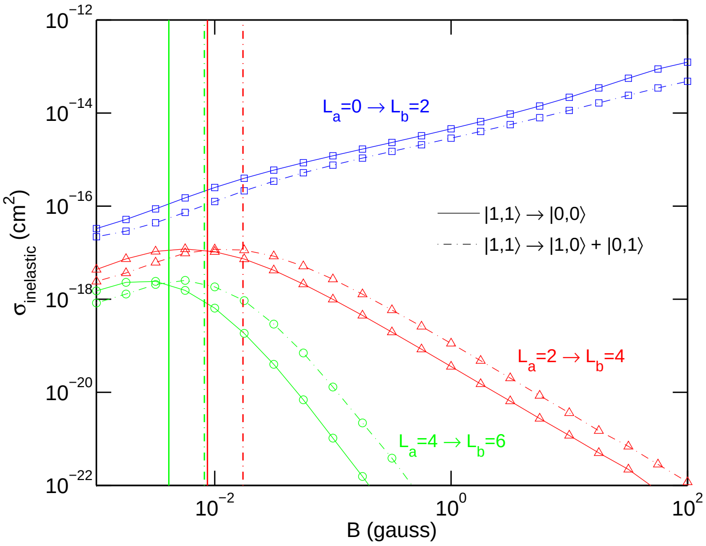

Figure 5.1: State-to-state collision cross sections for the $|M_{S_A} = 1, M_{S_B} = 1\rangle \to |M_{S_A} = 0, M_{S_B} = 0\rangle$ and $|M_{S_A} = 1, M_{S_B} = 1\rangle \to |M_{S_A} = 1, M_{S_B} = 0\rangle + |M_{S_A} = 0, M_{S_B} = 1\rangle$ transitions of NH + NH, obtained from coupled-channels calculations as a function of magnetic field at $E = 10^{-6}$ K. The (blue) lines marked with squares correspond to $L_a = 0 \to L_b = 2$ transitions, the (red) lines marked with triangles correspond to $L_a = 2 \to L_b = 4$, and the (green) lines marked with circles correspond to $L_a = 4 \to L_b = 6$. The vertical lines indicate the B_c values below which the crossings for $L_a = 2 \to L_b = 4$ and $L_a = 4 \to L_b = 6$ are energetically accessible.

B-dependence is remarkable, considering that higher partial waves typically contribute only if the exothermicity in the outgoing channel is large. Due to the long-range nature of the magnetic dipole interaction, however, a *decrease* in exothermicity will shift the crossings points R_c to a larger distance and consequently lead to *more* scattering of higher partial waves.

The influence of the kinetic energy on the inelastic cross section can also be understood in terms of the adiabatic curve crossings. For a given magnetic field strength, the avoided crossings for $L_a = 2 \to L_b = 4$ and $L_a = 4 \to L_b = 6$ are accessible only if the collision energy exceeds the E_c value of Eq. (5.25). It follows from Eqs. (5.24) and (5.25) that, if E_c increases, the critical field strength B_c increases as well, and higher partial waves can contribute over an increasingly wide range of fields. This is also reflected in Figs. 5.1 and 5.2. In the ultracold regime, at a collision energy of 10^{-6} K (Fig. 5.1), the B_c values for $L_a = 2 \to L_b = 4$ and $L_a = 4 \to L_b = 6$ are relatively small and the s-wave incident channel ($L_a = 0 \to L_b = 2$) is strongly dominant at all field strengths above $B \approx 10^{-2}$ G. At 10^{-3} K, however, the B_c values for the higher partial-wave channels are much larger, and we find that the $L_a = 2$ and 4 incoming channels play a significant role at all magnetic field strengths below $B \approx 10$ G. A more detailed discussion on the energy dependence of the spin-inelastic cross section, based on the Born approximation, will be given in the next section.

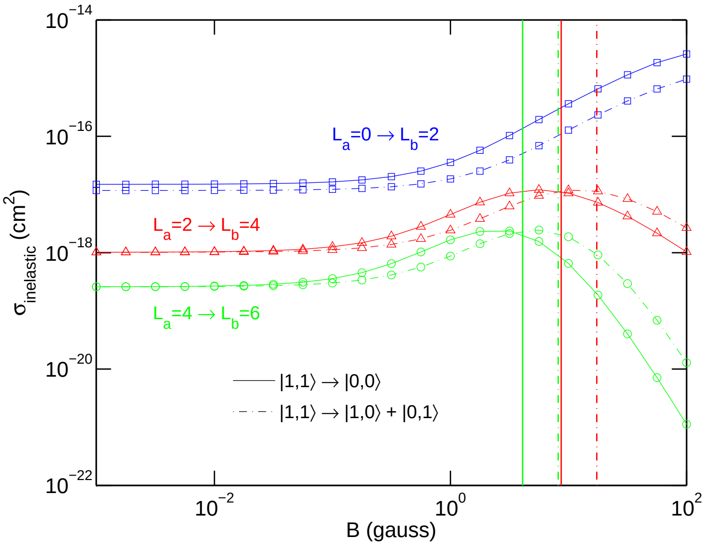

Figure 5.2: State-to-state collision cross sections for the $|M_{S_A} = 1, M_{S_B} = 1\rangle \to |M_{S_A} = 0, M_{S_B} = 0\rangle$ and $|M_{S_A} = 1, M_{S_B} = 1\rangle \to |M_{S_A} = 1, M_{S_B} = 0\rangle + |M_{S_A} = 0, M_{S_B} = 1\rangle$ transitions of NH + NH, obtained from coupled-channels calculations as a function of magnetic field at $E = 10^{-3}$ K. The (blue) lines marked with squares correspond to $L_a = 0 \to L_b = 2$ transitions, the (red) lines marked with triangles correspond to $L_a = 2 \to L_b = 4$, and the (green) lines marked with circles correspond to $L_a = 4 \to L_b = 6$. The vertical lines indicate the B_c values below which the crossings for $L_a = 2 \to L_b = 4$ and $L_a = 4 \to L_b = 6$ are energetically accessible.

5.3.2 Comparison with BA and DWBA

Before comparing our numerical results with the analytical BA and DWBA expressions, we must first point out that Eqs. (5.16) and (5.23) apply only to collisions in which M_{S_A} and M_{S_B} each change at most by 1 and L changes at most by 2. Furthermore, the integral of Eq. (5.22) is defined only if $L_b > L_a + 1$, and the DWBA cross section of Eq. (5.23) is therefore valid only for $L_a \to L_a + 2$ transitions. Figure 5.3 shows the $|M_{S_A}^{(a)} = 1, M_{S_B}^{(a)} = 1, L_a\rangle \to |M_{S_A}^{(b)}, M_{S_B}^{(b)}, L_a + 2\rangle$ cross sections as a function of B at a collision energy of 10^{-6} K. The cross sections are summed over all final states with $|M_{S_A}^{(b)} - M_{S_A}^{(a)}| \leq 1$ and $|M_{S_B}^{(b)} - M_{S_B}^{(a)}| \leq 1$. Figure 5.4 shows the results as a function of collision energy at a magnetic field strength of 1 G. It can be seen that the BA results are in very good agreement with the cross sections obtained from full coupled-channels calculations, in particular at low magnetic fields and low collision energies. At high fields and energies, the numerical cross sections exhibit several resonance features that arise mainly from the *intramolecular* spin-spin coupling term. Note that this coupling term is not included in the (DW)BA. Previous work has shown that the intramolecular spin-spin coupling becomes increasingly important as the kinetic energy in the outgoing channel increases, and, for $B > 10^2$ G and $E > 10^{-2}$ K, causes almost the same amount of spin relaxation as the intermolecular magnetic dipolar interaction (see Figs. 4.4 and

4.5). Hence, the BA result of Eq. (5.16) deviates from the coupled-channels result at high energies and field strengths.

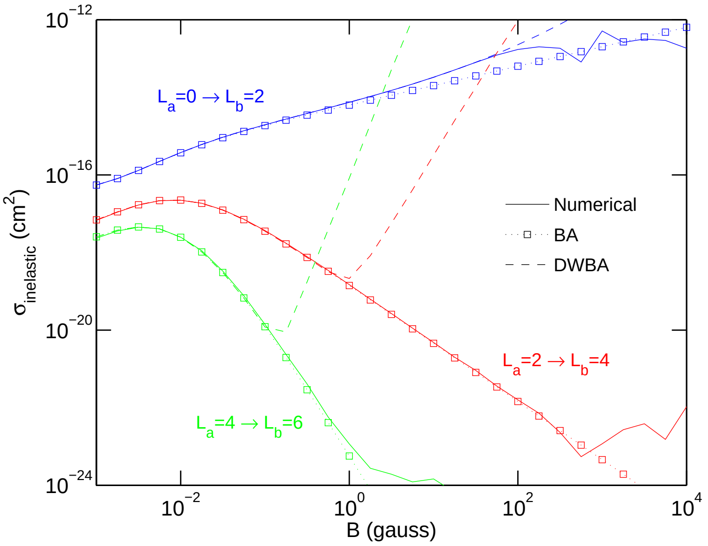

Figure 5.3: Total spin-inelastic collision cross sections for the $|M_{S_A}=1, M_{S_B}=1\rangle \rightarrow |M_{S_A}=0, M_{S_B}=0\rangle$ and $|M_{S_A}=1, M_{S_B}=1\rangle \rightarrow |M_{S_A}=1, M_{S_B}=0\rangle + |M_{S_A}=0, M_{S_B}=1\rangle$ transitions of NH + NH, calculated as a function of magnetic field at 10^{-6} K. Different colors correspond to different $L_a \rightarrow L_b$ channel transitions.

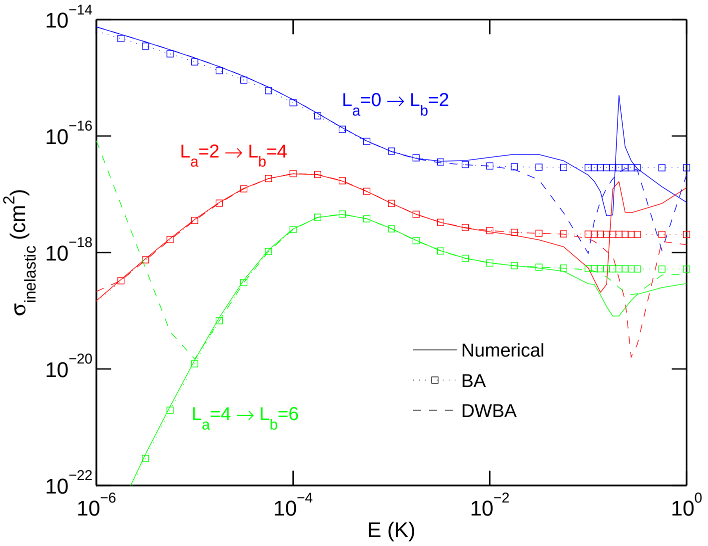

Figure 5.4: Total spin-inelastic collision cross sections for the $|M_{S_A}=1, M_{S_B}=1\rangle \rightarrow |M_{S_A}=0, M_{S_B}=0\rangle$ and $|M_{S_A}=1, M_{S_B}=1\rangle \rightarrow |M_{S_A}=1, M_{S_B}=0\rangle + |M_{S_A}=0, M_{S_B}=1\rangle$ transitions of NH + NH, calculated as a function of collision energy at a magnetic field strength of 1 G. Different colors correspond to different $L_a \rightarrow L_b$ channel transitions.

It can also be seen in Figs. 5.3 and 5.4 that the analytical distorted-wave BA cross section, which contains an extra term due to the phase shift in the incoming channel, is in slightly better agreement with the numerical $L_a = 0 \to L_b = 2$ cross section than the BA result. In particular, Fig. 5.3 shows that the BA cross section for $L_a = 0 \to L_b = 2$ starts to deviate from the coupled-channels calculations around $B \approx 1$ G, while the DWBA is accurate up to $B \approx 100$ G. Thus, in the region between 1 and 100 G, the inelastic $L_a = 0 \to L_b = 2$ cross section can be completely attributed to the intermolecular magnetic dipole interaction and to the phase shift in the incident channel. For the higher partial-wave channels, however, the analytical DWBA cross section deviates significantly from the coupled-channels result at high fields and low energies. This is due to the $(k_b/k_a)^{L_a+1}$ term in the expression for $\sigma_{a\to b}^{\mathrm{DWBA}}$ [Eq. (5.23)], which tends to infinity if $k_a \ll k_b$. Even for very small phase shifts, this term will dominate the DWBA inelastic cross section for $L_a > 0$ if the collision energy is small and the exothermicity is large. More specifically, we estimate from Eq. (5.23) that the DWBA cross section diverges if $(k_a/k_b)^{2L_a+1} \approx T_{aa}^{(M_a)}$, and hence the effect is most pronounced for large L_a. We point out that the origin of the $(k_b/k_a)^{L_a+1}$ term lies in the irregular spherical Bessel function $y_{L_a}(k_a R)$ [Eq. (5.22)], which enters the asymptotic wave function if the phase shift is nonzero. At short range, the y_{L_a} function tends to infinity and ultimately leads to the unphysical behaviour observed in Figs. 5.3 and 5.4. A possible remedy for this problem is to evaluate the integral of Eq. (5.22) only for R-values larger than a certain cutoff radius. However, such an approach requires careful numerical analysis and falls out of the scope of the present study. Nevertheless, based on the results shown in Figs. 5.3 and 5.4, we conclude that the BA gives more meaningful results than the analytical DWBA at most of the energies and fields considered in this work. As a final point, we note that the numerical phase shifts for the higher partial-wave channels are orders of magnitude smaller than the s-wave scattering phase shift, and our DWBA results would not be substantially improved by including a phase shift in the outgoing channel.

As derived in Sec. 5.2.2, the threshold behaviour of the BA spin-inelastic cross section in the limit of $k_a \ll k_b$ is given by $\sigma_{a\to b} \sim B^{1/2-L_a}$ and $\sigma_{a\to b} \sim E^{L_a-1/2}$. Indeed, we find that the $L_a = 0 \to L_b = 2$, $L_a = 2 \to L_b = 4$, and $L_a = 4 \to L_b = 6$ inelastic cross sections at 10^{-6} K behave as $B^{1/2}$, $B^{-3/2}$, and $B^{-7/2}$, respectively, for field strengths above $B \approx 5 \times 10^{-2}$ G (see Fig. 5.3). Similarly, the cross sections at $B = 1$ G follow an $E^{-1/2}$, $E^{3/2}$, and $E^{7/2}$ dependence, respectively, at collision energies below $E \approx 10^{-4}$ K (see Fig. 5.4). The validity regions of these threshold laws can also be explained in terms of the $V_{\mathrm{magn.dip}}$-induced avoided crossings discussed in Sec. 5.3.1. The critical magnetic field strengths below which the $L_a = 2 \to L_b = 4$ and $L_a = 4 \to L_b = 6$ crossings are energetically accessible are on the order of $B_c \approx 10^{-2}$ G for a collision energy of 10^{-6} K (see Fig. 5.1). If the magnetic field strength exceeds B_c, the crossings for the higher partial-wave channels are inaccessible and the corresponding scattering process can proceed only by (non-classical) tunneling through the centrifugal barrier. Hence we find the quantum-mechanical threshold behaviour at fields *above*

$B \approx 10^{-2}$ G. For field strengths below B_c, the approximation of $k_a \ll k_b$ breaks down and the B-dependence follows from the explicit evaluation of Eq. (5.16). That is, the B-dependent threshold behaviour for $B < B_c$ is given by $(k_a/k_b)^{2L_a-1}$ multiplied by the hypergeometric function. If the magnetic field is so small that $k_a \approx k_b$, the field dependence becomes negligible and the cross section flattens off to a constant value. In order to explain the energy dependence, we apply Eqs. (5.24) and (5.25) to determine the lowest possible E_c values at which the avoided curve crossings can occur. At a magnetic field of 1 G, the corresponding values are $E_c = 5.8 \times 10^{-5}$ K for the $L_a = 2 \rightarrow L_b = 4$ transition and $E_c = 1.2 \times 10^{-4}$ K for $L_a = 4 \rightarrow L_b = 6$. Since the crossings for the higher partial-wave channels are inaccessible if $E < E_c$, we recover the quantum-mechanical threshold law at collision energies *below* $E \approx 10^{-4}$ K.

The results presented so far apply only to collisions where M_{S_A} and M_{S_B} decrease at most by 1 and L increases by 2. The *total* spin-inelastic cross section, however, contains contributions from all (symmetry-allowed) outgoing partial waves and all final states, i.e. also the states with $M_{S_A}^{(b)} = -1$ and $M_{S_B}^{(b)} = -1$. Let us now compare the BA and DWBA results with the numerical *total* spin-inelastic cross sections for magnetically trapped NH ($M_{S_A}^{(a)} = M_{S_B}^{(a)} = 1$), summed over all possible incoming partial waves and all outgoing channels. The total BA cross section is obtained by performing the sums over L_a and L_b in Eq. (5.16) for all possible (even) partial waves. To calculate the total DWBA cross section, we perform the sums over L_a and L_b in Eq. (5.23) for all possible (even) L_a values and $L_b = L_a + 2$. Since the numerical scattering calculations were carried out for $L_{\max} = 6$, we also took this maximum value for L_a and L_b in the (DW)BA expressions.

The total inelastic cross sections are presented in Figs. 5.5 and 5.6. It can be seen that the BA is generally in much better agreement with the coupled-channels result than the DWBA, except for a small region near 10 G at 10^{-3} K (Fig. 5.5) and near 10^{-3} K at 100 G (Fig. 5.6), where $k_a \approx k_b$. As noted previously, the deviation of the DWBA at high B and low E is due to the $(k_b/k_a)^{L_a+1}$ term in Eq. (5.23), which causes unphysical behaviour if $k_b \gg k_a$. At low magnetic fields and relatively high energies, in particular at $E = 10^{-3}$ K (see Fig. 5.5), we find that the DWBA cross section also deviates from the numerical result. In this region, the spin relaxation arises mainly from the $L_a = 2 \rightarrow L_b = 2$ transition, and, to a smaller extent, also from the $L_a = 0 \rightarrow L_b = 2$ and $L_a = 2 \rightarrow L_b = 0$ transitions. Since the total DWBA cross section is restricted such that $L_b = L_a + 2$, the most dominant inelastic transitions at low B are thus not included in the DWBA. Similarly, the total DWBA cross section as a function of energy (Fig. 5.6) shows a clear discrepancy with the numerical result at $B = 0.01$ G for nearly all energies considered, and at $B = 1$ G for $E > 10^{-3}$ K. This is also due primarily to the missing $L_a = 2 \rightarrow L_b = 2$ channel transition.

It can also be seen that the total BA cross section, which does include all possible $L_a \rightarrow L_b$ transitions, agrees over a much wider range of E and B, but deviates from the coupled-channels result at high fields and high collision energies. As already discussed in the first paragraph of this section, the deviation partly arises from the *intramolecular*

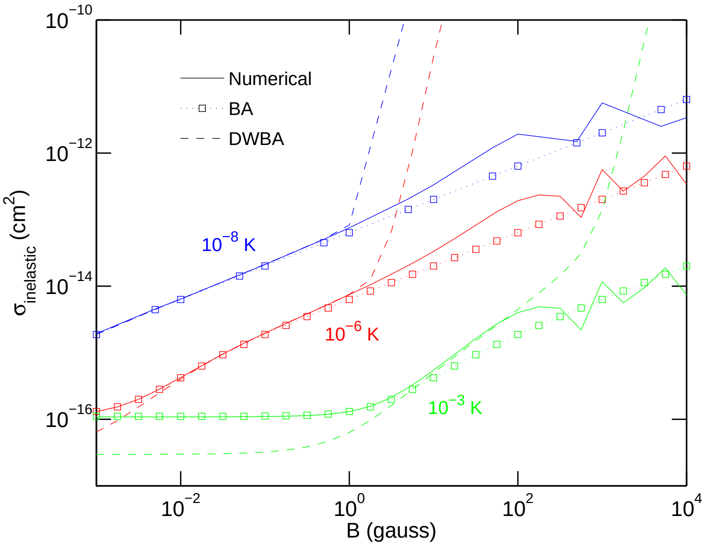

Figure 5.5: Total spin-inelastic collision cross sections for two magnetically trapped NH molecules, calculated as a function of magnetic field. Different colors correspond to different collision energies.

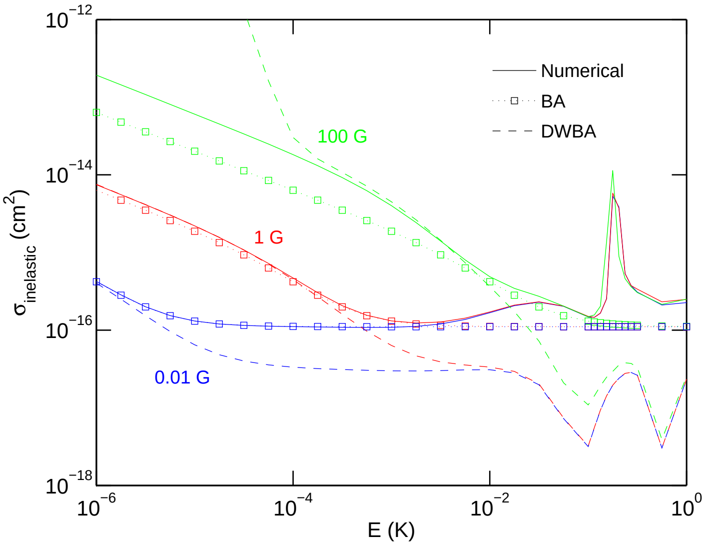

Figure 5.6: Total spin-inelastic collision cross sections for two magnetically trapped NH molecules, calculated as a function of collision energy. Different colors correspond to different magnetic field strengths.

spin-spin coupling term, which contributes significantly to the numerical cross section as the kinetic energy in the outgoing channel becomes large. Moreover, the BA only includes contributions from final states with $M_{S_A} = 0, 1$ and $M_{S_B} = 0, 1$, while the total numerical cross section also contains terms with $M_{S_A} = -1$ and $M_{S_B} = -1$. The results of Chapter 4 have shown that, as the intramolecular spin-spin coupling term becomes increasingly important, the state-to-state cross sections for $M_{S_A}^{(b)} = -1$ and/or $M_{S_B}^{(b)} = -1$ increase as well (see Fig. 4.6). Although the dominant mechanism for $M_{S_i}^{(a)} = 1 \rightarrow M_{S_i}^{(b)} = -1$ transitions is likely to be the intramolecular spin-spin term, which can decrease M_{S_i} by 2 directly in first order, the intermolecular magnetic dipolar coupling term may also induce such spin-changing collisions in second order. This effect is included only in the full coupled-channels calculation, and hence this may represent another source of discrepancy between the BA and the numerical result.

5.4 Conclusions

We have presented a detailed theoretical study on the role of the intermolecular magnetic dipole-dipole interaction in cold and ultracold collisions of magnetically trapped NH($X\,^3\Sigma^-$) molecules. The inelastic cross sections for Zeeman relaxation have been obtained from rigorous coupled-channels calculations and from analytical results based on the (distorted-wave) Born approximation. The derived expressions for the analytical cross sections are valid for any two paramagnetic species for which the electronic spin and its space-fixed projection are (approximately) good quantum numbers, but we have applied them only to the NH + NH system.

We have found that the scattering of different partial waves, induced by the magnetic dipolar coupling, is most easily understood by considering the adiabatic potential curves. The intermolecular dipolar coupling term induces avoided crossings between certain adiabats at long range, which in turn may lead to Zeeman relaxation. The cross-section behaviour as a function of energy and magnetic field is, to a large extent, determined by whether or not these avoided crossings are energetically accessible. Remarkably, the avoided crossings for higher partial waves become lower in energy as the magnetic field strength decreases, implying that the corresponding channels open up *below* a certain critical field strength. Indeed, it was found that the scattering of higher partial waves becomes increasingly important as the exothermicity *decreases*.

The validity regions of the analytical BA and DWBA have been determined by comparison with numerical close-coupling calculations. We have found that the BA is accurate over a wide range of collision energies and fields, but starts to deviate from the numerical cross sections at energies above $\approx 10^{-2}$ K and fields above $\approx 10^2$ G. This is mainly due to the effect of the *intramolecular* spin-spin coupling term, which is neglected in the BA but contributes significantly to the numerical cross section as the kinetic energy in the outgoing channel becomes large. The analytical distorted-wave Born approximation, which accounts for a phase shift in the incident channel and thus represents a correction to the BA, gives more accurate results than the BA in the case of s-wave scattering. For higher partial-wave scattering, however, and in particular at high magnetic fields and low energies, the DWBA cross section shows unphysical behaviour and diverges to infinity. Furthermore, the derived DWBA expression is valid only for collisions where the partial-wave angular momentum is increased by 2, while the total numerical cross section contains contributions from all possible outgoing partial waves. More specifically, at fields below ≈ 1 G and energies near 10^{-3} K, the dominant contribution to the inelastic cross section is the $L_a = 2 \rightarrow L_b = 2$ channel transition, which is not included in the DWBA. Hence we conclude that the BA, which contains all possible partial-wave contributions and does not show any unphysical behaviour, is generally in much better agreement with the coupled-channels result than the DWBA.

Although we have focused only on NH($^3\Sigma^-$) + NH($^3\Sigma^-$) collisions in this study, the theory and main conclusions should be general for any two (ultra)cold paramagnetic species.

Chapter 6

Quantum reactive scattering

This final chapter deals with the quantum reaction dynamics of magnetically trapped NH. We present a novel coupled-channels reactive scattering method in which only the reactant arrangement is explicitly taken into account. It is assumed that, once a reactive complex is formed at a sufficiently short intermolecular distance, the reaction proceeds irreversibly. We have applied our method to cold and ultracold NH + NH collisions, both in a field-free environment and in a magnetic field. It is found that most of the reactive collisions are governed by the intramolecular spin-spin coupling, and that the dynamics is non-universal. The reactive cross sections are virtually independent of magnetic field strength for fields below 100 G, consistent with the Wigner threshold law for exoergic processes. As a consequence, the reactivity can also be accurately predicted by field-free calculations. This result implies, however, that magnetic field control of NH + NH chemical reactions will be rather difficult. Furthermore, we find that reactive scattering processes can compete strongly with elastic collisions, making evaporative cooling of magnetically trapped NH more challenging than previously expected. Nevertheless, based on a sampling of the uncertainty range of the interaction potentials, we conclude that both cold controlled chemistry and evaporative cooling of NH remain feasible.

6.1 Introduction

The ability to produce and trap atomic and molecular species at sub-kelvin temperatures offers numerous exciting possibilities in the field of chemistry. Recent experiments have demonstrated that cold chemical reactions can be efficiently manipulated by applying an external electromagnetic field, either by tuning the electric dipole-dipole interaction in a polar molecular gas [36], by controlling the stereodynamics through a confining trapping potential [45], or by tuning the reaction from endo- to exoergic [132]. For an ultracold gas composed of a single species, the reactivity may also be controlled by changing the internal quantum state of one of the collision partners, thereby exploiting the quantum statistics of identical particles [44]. Furthermore, the pronounced quantum behaviour of ultracold matter may lead to novel phenomena such as "superchemistry", a process in which an atomic and molecular Bose-Einstein condensate are coherently coupled to stimulate the formation of molecules [133].

Up to the present, experimental studies on ultracold chemical reactions have focused only on (bi-)alkali-metal systems with a rather limited chemistry. Moreover, most of the ultracold reactive processes observed so far exhibit universal behaviour, i.e., the dynamics are completely governed by long-range interactions and the reaction proceeds with unit probability once the reactants are sufficiently close to each other [134]. Cold reactive collisions in the non-universal regime, as well as cold reactions involving non-alkali or paramagnetic molecules, are still largely unexplored. Knowledge of the degree of universality is useful to understand and interpret the (generally complex) full-dimensional reaction dynamics in terms of simple few-parameter models. In particular, one may separate the scattering problem into a short-range and long-range component, and capture the complicated physics at short range in a single 'universality' parameter. Such an approach can also prove useful for molecular systems for which coupled-channels calculations are intractable.

In this work, we consider the chemistry of (ultra)cold NH($X\,^3\Sigma^-$) radicals both in the presence and absence of a magnetic field. Reactive NH + NH collisions can yield as many as 8 different product arrangements (see Fig. 1.4), making it a versatile system for (ultra)cold chemistry experiments. Furthermore, chemical reactions between two magnetically trapped NH molecules can proceed only if the NH–NH collision complex – initially in the non-reactive quintet state – undergoes a spin-change to either the singlet or triplet dimer state. Thus, the NH + NH reaction dynamics may be non-universal. In order to study the reactivity of cold NH radicals, we have employed a single-arrangement quantum reactive scattering method in which only the reactant configuration is explicitly taken into account. The cross sections are obtained from rigorous coupled-channels calculations, but they are not resolved for the different reaction product states. It will be shown that the total reaction probability is indeed non-universal and is strongly dependent on the details of the (short-range) interaction potentials. This constitutes one of the first examples of a non-universal chemistry in the cold and ultracold regime.

This chapter is organized as follows. In Sec. 6.2, we first outline the basic idea of our quantum reactive scattering method and subsequently present a general derivation of the propagation algorithm (Sec. 6.2.1). Reactive scattering boundary conditions and the construction of the S-matrix are discussed in Sec. 6.2.2, followed by a summary of the computational details of the NH + NH cross section calculations (Sec. 6.2.3). Results and conclusions are given in Secs. 6.3 and 6.4, respectively. We end Sec. 6.4 with some general concluding remarks regarding this thesis.

6.2 Theory

Throughout this chapter, we focus on collisions between two magnetically trapped ^{15}NH($X\,^3\Sigma^-$) molecules and treat the monomers as rigid rotors. The coordinate system consists of the intermolecular vector $\boldsymbol{R}$, with length R, the polar angles θ_A and θ_B of the monomers, and the dihedral angle ϕ (see Fig. 2.1). Figure 6.1 shows a plot of the minima of the three NH–NH potentials as a function of R, obtained by scanning over the angles θ_A, θ_B, and ϕ for each value of R. It can be seen that the singlet and triplet potentials are strongly attractive at small intermolecular distances, which is due to their chemically reactive nature (see also Figs. 1.4 and 1.6). The minima of the singlet and triplet surfaces correspond to the covalently bound N_2H_2 configuration, with $\theta_A = \theta_B \approx 90°$.

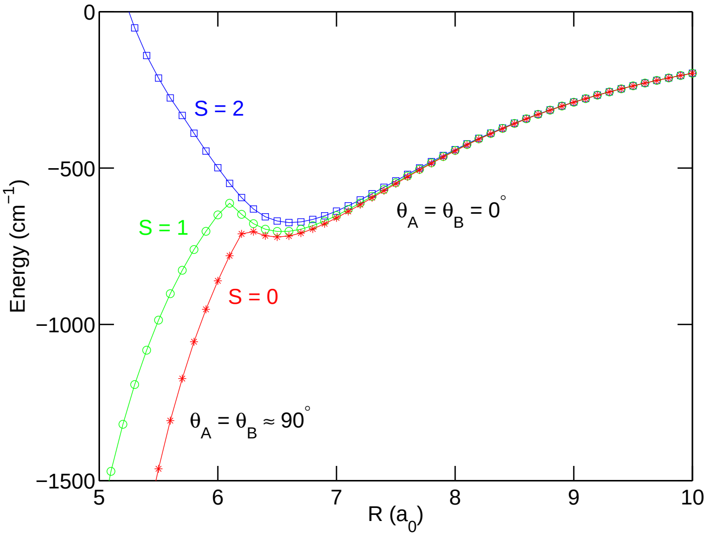

Figure 6.1: Minimum of the quintet ($S = 2$), triplet ($S = 1$), and singlet ($S = 0$) NH–NH potential energy surfaces as a function of R, obtained by scanning over the angles θ_A, θ_B, and ϕ for each value of R. The van der Waals minimum at $R = 6.6\ a_0$ corresponds to a linear geometry, with $\theta_A = \theta_B = 0°$, while the deep minima of the singlet and triplet states ($R < 6\ a_0$) correspond to $\theta_A = \theta_B \approx 90°$. The figure is adapted from Ref. [90].

In view of the deep potential energy wells for the singlet and triplet states, we may assume that, once a singlet or triplet NH–NH complex is formed, the system readily undergoes chemical rearrangement. For instance, NH + NH may react into the chemically stable N_2H_2 molecule (provided that a third body can dissipate the excess kinetic energy) or into a binary product configuration such as $N_2 + H_2$ (see Fig. 1.4). In order to calculate the total reaction probability, we consider only the NH + NH reactant arrangement and assume a “point of no return” on the reactive singlet and triplet potential energy surfaces. That is, at a certain value of the radial coordinate, R_0, we allow flux to disappear into reactive channels. Note that collisions occurring on the quintet potential are non-reactive. Our method differs from the well-established log-derivative approach (see also Sec. 1.4.2) as follows. In the case of single-arrangement reactive scattering, the log-derivative propagator is initialized by applying complex boundary conditions in the short range [78, 83], resulting in a non-unitary S-matrix. The deviation from unitarity is used to calculate the reactive scattering cross section for a given incoming channel. Here, we first calculate a complete set of (real-valued) regular and irregular solutions of the coupled-channels equations, and impose the desired boundary conditions *after* the propagation. Thus, once the propagation routine is completed, we may enforce *all* possible boundary conditions to construct all possible scattering wave functions for a given Hamiltonian. We have exploited this feature to test two types of reactive boundary conditions. In all cases, the S-matrix is manifestly unitary. Although not implemented, our method also allows for parallelization of the scattering code. This may be achieved by solving the coupled-channels equations for different intervals and matching the solutions afterwards. Our propagation algorithm, which is based on the renormalized Numerov method, is outlined in the following section. Section 6.2.2 describes how appropriate boundary conditions can be applied to extract the reactive scattering S-matrix.

6.2.1 Propagation

We start by defining an equidistant radial grid of points $R_i, i = 0, \ldots, n$, with a grid spacing of Δ. We consider a channel basis of dimension N and assume that all matrix elements of the coupling matrix $\boldsymbol{W}(R_i)$ are known for a given total energy E [see Eq. (1.7)]. Our aim is to find two linearly independent solutions per channel for the coupled-channels equations, $\boldsymbol{U}''(R) = \boldsymbol{W}(R)\boldsymbol{U}(R)$, by numerical propagation from R_0 to R_n (see Fig. 6.2). The two sets of solutions, referred to as regular and irregular solutions, will be denoted as $\boldsymbol{F}^{(n)}(R)$ and $\boldsymbol{G}^{(n)}(R)$, respectively. The superscript (n) refers to the interval $[R_0, R_n]$. The functions are defined by the following boundary conditions:

$$\boldsymbol{F}_0^{(n)} = \mathbf{0}, \qquad \boldsymbol{F}_n^{(n)} = \mathbf{1}, \tag{6.1}$$

$$\boldsymbol{G}_0^{(n)} = \mathbf{1}, \qquad \boldsymbol{G}_n^{(n)} = \mathbf{0}, \tag{6.2}$$

where we have written $\boldsymbol{F}_i^{(n)} \equiv \boldsymbol{F}^{(n)}(R_i)$ and $\boldsymbol{G}_i^{(n)} \equiv \boldsymbol{G}^{(n)}(R_i)$. The symbols $\mathbf{0}$ and $\mathbf{1}$ represent the null and identity matrix, respectively. To initialize the propagation, we write for $n = 1$

$$\boldsymbol{F}_0^{(1)} = \mathbf{0}, \qquad \boldsymbol{F}_1^{(1)} = \mathbf{1}, \tag{6.3}$$

$$\boldsymbol{G}_0^{(1)} = \mathbf{1}, \qquad \boldsymbol{G}_1^{(1)} = \mathbf{0}. \tag{6.4}$$

We will now outline the algorithm to propagate the solutions to larger R. In order to apply the scattering boundary conditions, we will only require the function values in points R_0, R_1, R_{n-1}, and R_n. For the sake of completeness, however, we will derive the general expressions for an arbitrary point R_i.

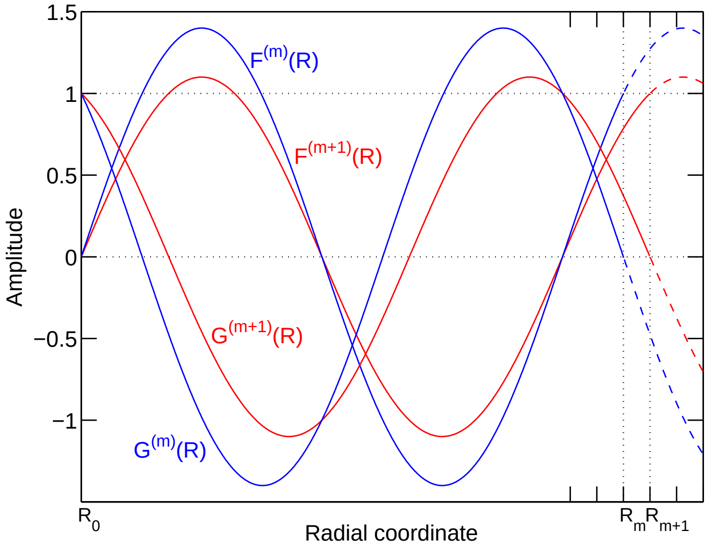

Figure 6.2: Example of two regular and irregular solutions on the intervals $[R_0, R_m]$ (blue lines) and $[R_0, R_{m+1}]$ (red lines).

Renormalized Numerov propagation [79] for $n \geq 2$ relies on the three-point recurrence formula

$$-\boldsymbol{C}_{i-1}\boldsymbol{U}_{i-1} + (12\,\boldsymbol{1} - 10\,\boldsymbol{C}_i)\boldsymbol{U}_i - \boldsymbol{C}_{i+1}\boldsymbol{U}_{i+1} = \boldsymbol{0}, \tag{6.5}$$

where $\boldsymbol{C}_i = \boldsymbol{1} - \frac{\Delta^2}{12}\boldsymbol{W}_i$ and $\boldsymbol{W}_i \equiv \boldsymbol{W}(R_i)$. We first consider the regular solutions $\boldsymbol{U}(R) = \boldsymbol{F}^{(n)}(R)$, for which the Numerov algorithm is relatively straightforward. If we express $\boldsymbol{F}_i^{(n)}$ in terms of $\boldsymbol{F}_{i+1}^{(n)}$,

$$\boldsymbol{F}_i^{(n)} = \boldsymbol{Q}_{i+1}\boldsymbol{F}_{i+1}^{(n)}, \tag{6.6}$$

we may derive a recurrence relation for the coefficient matrices $\boldsymbol{Q}$ by inserting Eq. (6.6) into Eq. (6.5). This yields

$$\boldsymbol{Q}_{i+1} = [12\,\boldsymbol{1} - 10\,\boldsymbol{C}_i - \boldsymbol{C}_{i-1}\boldsymbol{Q}_i]^{-1}\boldsymbol{C}_{i+1}, \tag{6.7}$$

which, subject to the boundary condition $\boldsymbol{F}_0^{(n)} = \boldsymbol{Q}_1 = \boldsymbol{0}$, provides the Q-matrices for all values of i. This is the well known renormalized Numerov scheme for standard inelastic scattering [79]. We note that the Q-matrices are independent of the length of the grid, and hence the superscript (n) has been omitted in our notation for $\boldsymbol{Q}_i$. Once the Q-matrices are known over a certain interval $[R_0, R_m]$, with $R_m \leq R_n$, the values for $\boldsymbol{F}_i^{(m)}$ readily follow from Eq. (6.6) and the requirement that $\boldsymbol{F}_m^{(m)} = \boldsymbol{1}$:

$$\begin{aligned}\boldsymbol{F}_i^{(m)} &= \boldsymbol{Q}_{i+1}\boldsymbol{Q}_{i+2}\ldots\boldsymbol{Q}_{m-1}\boldsymbol{Q}_m\boldsymbol{F}_m^{(m)} \\ &= \prod_{k=i+1}^{m}\boldsymbol{Q}_k.\end{aligned} \tag{6.8}$$

When propagating from R_m to R_{m+1} (with $\boldsymbol{F}_{m+1}^{(m+1)} = \mathbf{1}$), the function values can thus be updated through

$$\boldsymbol{F}_i^{(m+1)} = \boldsymbol{F}_i^{(m)} \boldsymbol{Q}_{m+1}. \tag{6.9}$$

As a special case, we note that $\boldsymbol{F}_{n-1}^{(n)}$ is identical to $\boldsymbol{Q}_n$ by virtue of Eq. (6.6).

The irregular solutions $\boldsymbol{G}^{(n)}(R)$ are equivalent to the *regular* functions obtained by propagating in the *reversed* direction, i.e. from R_n to R_0. It will be demonstrated, however, that the irregular solutions can also be obtained during the propagation from R_0 to R_n. That is, a single propagation run is sufficient to obtain the two sets of solutions. In order to calculate $\boldsymbol{G}^{(n)}(R)$, we first recognize that, for any interval $[R_0, R_m]$, the functions $\boldsymbol{F}^{(m)}(R)$ and $\boldsymbol{G}^{(m)}(R)$ are linearly independent. Hence, we may write

$$\boldsymbol{G}_i^{(m+1)} = \boldsymbol{G}_i^{(m)} \boldsymbol{X}_G^{(m)} + \boldsymbol{F}_i^{(m)} \boldsymbol{X}_F^{(m)}. \tag{6.10}$$

By using the boundary conditions of Eqs. (6.1) and (6.2) and taking $i = 0$, we find that $\boldsymbol{X}_G^{(m)} = \mathbf{1}$, while $i = m$ gives $\boldsymbol{X}_F^{(m)} = \boldsymbol{G}_m^{(m+1)}$. Thus, we have

$$\boldsymbol{G}_i^{(m+1)} = \boldsymbol{G}_i^{(m)} + \boldsymbol{F}_i^{(m)} \boldsymbol{G}_m^{(m+1)}. \tag{6.11}$$

For $i = m + 1$, we obtain after some manipulation

$$\boldsymbol{G}_m^{(m+1)} = -\boldsymbol{Q}_{m+1} \boldsymbol{G}_{m+1}^{(m)}, \tag{6.12}$$

where we have used that $\boldsymbol{F}_m^{(m)} \equiv \mathbf{1} = \boldsymbol{Q}_{m+1} \boldsymbol{F}_{m+1}^{(m)}$. The factor $\boldsymbol{G}_{m+1}^{(m)}$ can be found by evaluating Eq. (6.5) for $\boldsymbol{U} = \boldsymbol{G}^{(m)}$ and using the boundary condition that $\boldsymbol{G}_m^{(m)} = \mathbf{0}$. This gives

$$\boldsymbol{G}_{m+1}^{(m)} = -\boldsymbol{C}_{m+1}^{-1} \boldsymbol{C}_{m-1} \boldsymbol{G}_{m-1}^{(m)}. \tag{6.13}$$

Substitution of Eq. (6.13) into Eq. (6.12) yields

$$\boldsymbol{G}_m^{(m+1)} = \boldsymbol{Q}_{m+1} \boldsymbol{C}_{m+1}^{-1} \boldsymbol{C}_{m-1} \boldsymbol{G}_{m-1}^{(m)}, \tag{6.14}$$

which completes our set of equations. The propagation from point R_m to R_{m+1} may now proceed as follows. First, the matrix $\boldsymbol{Q}_{m+1}$ is computed from Eq. (6.7), followed by an update of the regular functions $F^{(m+1)}(R)$ [Eq. (6.9)]. The irregular solutions can be updated using Eq. (6.11),

$$\boldsymbol{G}_i^{(m+1)} = \boldsymbol{G}_i^{(m)} + \boldsymbol{F}_i^{(m)} \boldsymbol{Q}_{m+1} \boldsymbol{C}_{m+1}^{-1} \boldsymbol{C}_{m-1} \boldsymbol{G}_{m-1}^{(m)}. \tag{6.15}$$

This procedure is repeated until the final grid point R_n is reached.

In order to speed up the calculation, the propagation may also be performed with a variable step size. This is particularly useful for scattering calculations at very low collision energies, for which the de Broglie wavelength can become very large. A relatively simple variable-step-size approach is to double the step size whenever the smallest local de Broglie wavelength increases by a factor of two, thus ensuring that the number of grid points per minimum wavelength is approximately constant. The algorithm needed for such propagation requires a small modification of the fixed-step-size routine described above. We will outline this modified procedure using the notation shown in Fig. 6.3. The points labeled with a prime refer to the doubly-spaced grid, with increments of $\Delta' = 2\Delta$, while labels without a prime correspond to the singly-spaced grid.

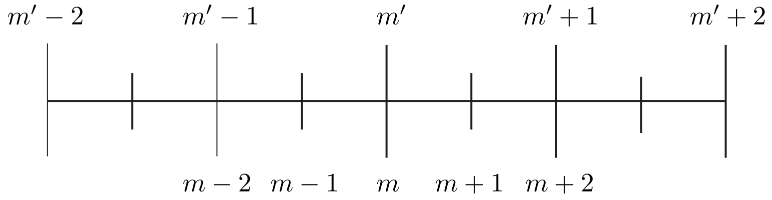

Figure 6.3: Radial grids used for renormalized Numerov propagation. Points labeled by m correspond to an equidistant grid with spacing Δ, and points labeled by m' correspond to a doubly-spaced grid with spacing $\Delta' = 2\Delta$.

We consider the case where the step size changes from Δ to Δ' at the point $R_m = R_{m'}$. It is assumed that all Q-matrices and function values are known over the complete interval $[R_0, R_m]$. The Q-matrix can be propagated from $R_{m'}$ to $R_{m'+1}$ using the relation

$$\boldsymbol{Q}_{m'+1} = [(12\,\mathbf{1} - 10\,\boldsymbol{C}_{m'}) - \boldsymbol{C}_{m'-1}\boldsymbol{Q}_{m'}]^{-1}\boldsymbol{C}_{m'+1}, \tag{6.16}$$

with $\boldsymbol{C}_{m'} = \mathbf{1} - \frac{(\Delta')^2}{12}\boldsymbol{W}_{m'}$ and $\boldsymbol{Q}_{m'} = \boldsymbol{Q}_{m-1}\boldsymbol{Q}_m$. Thus, the propagation to $R_{m'+1}$ evolves *as if* the grid has a constant spacing of Δ'. The regular functions are now given by

$$\boldsymbol{F}_i^{(m'+1)} = \boldsymbol{F}_i^{(m')}\boldsymbol{Q}_{m'+1}, \tag{6.17}$$

with $\boldsymbol{F}_i^{(m')} = \boldsymbol{F}_i^{(m)}$. For the irregular solutions we obtain [see also Eq. (6.11)]

$$\boldsymbol{G}_i^{(m'+1)} = \boldsymbol{G}_i^{(m')} + \boldsymbol{F}_i^{(m')}\boldsymbol{G}_{m'}^{(m'+1)}, \tag{6.18}$$

with $\boldsymbol{G}_i^{(m')} = \boldsymbol{G}_i^{(m)}$. The matrix $\boldsymbol{G}_{m'}^{(m'+1)}$ can be calculated in analogy to Eq. (6.14),

$$\boldsymbol{G}_{m'}^{(m'+1)} = \boldsymbol{Q}_{m'+1}\boldsymbol{C}_{m'+1}^{-1}\boldsymbol{C}_{m'-1}\boldsymbol{G}_{m'-1}^{(m')}. \tag{6.19}$$

The only remaining task is to find an expression for $\boldsymbol{G}_{m'-1}^{(m')}$. This function corresponds exactly to $\boldsymbol{G}_{m-2}^{(m)}$ on the singly-spaced grid, and hence we may write

$$\boldsymbol{G}_{m'-1}^{(m')} = \boldsymbol{G}_{m-2}^{(m-1)} + \boldsymbol{F}_{m-2}^{(m-1)}\boldsymbol{G}_{m-1}^{(m)}, \tag{6.20}$$

with $\boldsymbol{F}_{m-2}^{(m-1)} = \boldsymbol{Q}_{m-1}$. Since all of these terms are known from previous propagation steps, we can readily evaluate $G^{(m'+1)}(R)$ from Eq. (6.18). This completes the full propagation from $R_{m'}$ to $R_{m'+1}$.

In order to propagate from $R_{m'+1}$ to $R_{m'+2}$, we return to the standard fixed-step-size algorithm and employ a step size of Δ'. The process of step-size-doubling may be repeated as long as the number of points per de Broglie wavelength remains sufficiently large.

6.2.2 Boundary conditions and S-matrix

Once the $\boldsymbol{F}^{(n)}(R)$ and $\boldsymbol{G}^{(n)}(R)$ functions are known in the points R_0, R_1, R_{n-1}, and R_n, we may extract the scattering S-matrix by enforcing reactive scattering boundary conditions. Let us first consider the general scattering case depicted in Fig. 6.4. We allow flux to enter and exit in both the asymptotic NH + NH channels and the reactive NHNH channels, requiring only that the total flux is conserved. We distinguish two sets of final solutions, $\overleftarrow{\boldsymbol{\Psi}}(R)$ and $\overrightarrow{\boldsymbol{\Psi}}(R)$, with the overhead arrows indicating the direction of the incident flux. The matrices with flux-normalized incoming and outgoing waves are denoted as $\boldsymbol{I}_i$ and $\boldsymbol{O}_i$, respectively, with $\boldsymbol{I}_i \equiv \boldsymbol{I}(R_i)$ and $\boldsymbol{O}_i \equiv \boldsymbol{O}(R_i)$. Note that the directions of "incoming" and "outgoing" waves are different for R_0 and R_n. We will be interested only in the solutions $\overleftarrow{\boldsymbol{\Psi}}(R)$, with unit incoming flux at $R = R_n$, but we include $\overrightarrow{\boldsymbol{\Psi}}(R)$ for the sake of completeness.

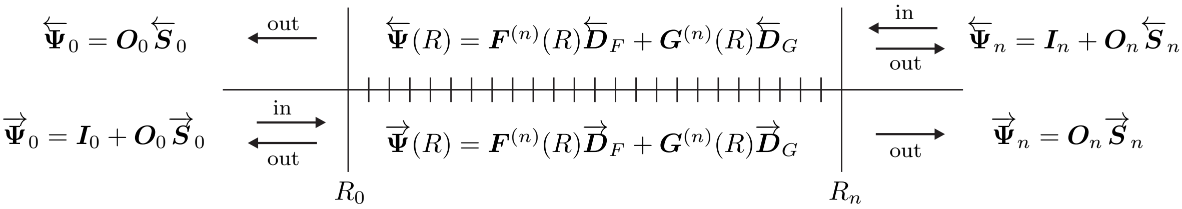

Figure 6.4: Schematic view of the reactive scattering wave functions obtained through renormalized Numerov propagation. The overhead arrows for the different wave functions indicate the direction of the incoming flux. See text for details.

The wave functions can be written as linear combinations of $\boldsymbol{F}^{(n)}(R)$ and $\boldsymbol{G}^{(n)}(R)$,

$$\overleftarrow{\boldsymbol{\Psi}}(R) = \boldsymbol{F}^{(n)}(R)\overleftarrow{\boldsymbol{D}}_F + \boldsymbol{G}^{(n)}(R)\overleftarrow{\boldsymbol{D}}_G, \tag{6.21}$$

$$\overrightarrow{\boldsymbol{\Psi}}(R) = \boldsymbol{F}^{(n)}(R)\overrightarrow{\boldsymbol{D}}_F + \boldsymbol{G}^{(n)}(R)\overrightarrow{\boldsymbol{D}}_G, \tag{6.22}$$

with the D-matrices representing R-independent coefficients. We now require that $\overleftarrow{\boldsymbol{\Psi}}(R)$ and $\overrightarrow{\boldsymbol{\Psi}}(R)$ obey the boundary conditions illustrated in Fig. 6.4. More specifically, for a given incident-flux direction, we define two $(N \times N)$ S-matrices, $\boldsymbol{S}_0$ and $\boldsymbol{S}_n$, which contain the probability amplitudes for transitions to reactive and non-reactive channels, respectively. These S-matrices are such that the total flux is rigorously conserved. In matrix notation, we obtain

$$\begin{aligned}
\begin{pmatrix} \overleftarrow{\boldsymbol{\Psi}}_n & \overrightarrow{\boldsymbol{\Psi}}_n \\ \overleftarrow{\boldsymbol{\Psi}}_0 & \overrightarrow{\boldsymbol{\Psi}}_0 \end{pmatrix} &= \begin{pmatrix} \boldsymbol{F}_n^{(n)} & \boldsymbol{G}_n^{(n)} \\ \boldsymbol{F}_0^{(n)} & \boldsymbol{G}_0^{(n)} \end{pmatrix} \begin{pmatrix} \overleftarrow{\boldsymbol{D}}_F & \overrightarrow{\boldsymbol{D}}_F \\ \overleftarrow{\boldsymbol{D}}_G & \overrightarrow{\boldsymbol{D}}_G \end{pmatrix} \\
&= \begin{pmatrix} \boldsymbol{I}_n & \boldsymbol{0} \\ \boldsymbol{0} & \boldsymbol{I}_0 \end{pmatrix} + \begin{pmatrix} \boldsymbol{O}_n & \boldsymbol{0} \\ \boldsymbol{0} & \boldsymbol{O}_0 \end{pmatrix} \begin{pmatrix} \overleftarrow{\boldsymbol{S}}_n & \overrightarrow{\boldsymbol{S}}_n \\ \overleftarrow{\boldsymbol{S}}_0 & \overrightarrow{\boldsymbol{S}}_0 \end{pmatrix},
\end{aligned} \tag{6.23}$$

where we have defined $\boldsymbol{\Psi}_i \equiv \boldsymbol{\Psi}(R_i)$. Note that the dimension of the matrices is $2N \times 2N$.

A similar expression may be written for the functions in points R_1 and R_{n-1}:

$$\begin{aligned}
\begin{pmatrix} \overleftarrow{\boldsymbol{\Psi}}_{n-1} & \overrightarrow{\boldsymbol{\Psi}}_{n-1} \\ \overleftarrow{\boldsymbol{\Psi}}_{1} & \overrightarrow{\boldsymbol{\Psi}}_{1} \end{pmatrix} &= \begin{pmatrix} \boldsymbol{F}^{(n)}_{n-1} & \boldsymbol{G}^{(n)}_{n-1} \\ \boldsymbol{F}^{(n)}_{1} & \boldsymbol{G}^{(n)}_{1} \end{pmatrix} \begin{pmatrix} \overleftarrow{\boldsymbol{D}}_F & \overrightarrow{\boldsymbol{D}}_F \\ \overleftarrow{\boldsymbol{D}}_G & \overrightarrow{\boldsymbol{D}}_G \end{pmatrix} \\
&= \begin{pmatrix} \boldsymbol{I}_{n-1} & \boldsymbol{0} \\ \boldsymbol{0} & \boldsymbol{I}_1 \end{pmatrix} + \begin{pmatrix} \boldsymbol{O}_{n-1} & \boldsymbol{0} \\ \boldsymbol{0} & \boldsymbol{O}_1 \end{pmatrix} \begin{pmatrix} \overleftarrow{\boldsymbol{S}}_n & \overrightarrow{\boldsymbol{S}}_n \\ \overleftarrow{\boldsymbol{S}}_0 & \overrightarrow{\boldsymbol{S}}_0 \end{pmatrix}. \qquad (6.24)
\end{aligned}$$

The $(2N \times 2N)$ matrix containing the $\boldsymbol{S}_n$ and $\boldsymbol{S}_0$ blocks will be referred to as the full S-matrix $\boldsymbol{S}$. It can be shown that this matrix is unitary provided that the $\boldsymbol{I}_i$ and $\boldsymbol{O}_i$ functions have the same flux normalization. By combining Eqs. (6.23) and (6.24), and using the definitions of Eqs. (6.1) and (6.2) for $\boldsymbol{F}^{(n)}_i$ and $\boldsymbol{G}^{(n)}_i$, we may write

$$\begin{aligned}
\begin{pmatrix} \overleftarrow{\boldsymbol{S}}_n & \overrightarrow{\boldsymbol{S}}_n \\ \overleftarrow{\boldsymbol{S}}_0 & \overrightarrow{\boldsymbol{S}}_0 \end{pmatrix} &= -\left[\begin{pmatrix} \boldsymbol{F}^{(n)}_{n-1} & \boldsymbol{G}^{(n)}_{n-1} \\ \boldsymbol{F}^{(n)}_{1} & \boldsymbol{G}^{(n)}_{1} \end{pmatrix} \begin{pmatrix} \boldsymbol{O}_n & \boldsymbol{0} \\ \boldsymbol{0} & \boldsymbol{O}_0 \end{pmatrix} - \begin{pmatrix} \boldsymbol{O}_{n-1} & \boldsymbol{0} \\ \boldsymbol{0} & \boldsymbol{O}_1 \end{pmatrix} \right]^{-1} \\
&\quad \times \left[\begin{pmatrix} \boldsymbol{F}^{(n)}_{n-1} & \boldsymbol{G}^{(n)}_{n-1} \\ \boldsymbol{F}^{(n)}_{1} & \boldsymbol{G}^{(n)}_{1} \end{pmatrix} \begin{pmatrix} \boldsymbol{I}_n & \boldsymbol{0} \\ \boldsymbol{0} & \boldsymbol{I}_0 \end{pmatrix} - \begin{pmatrix} \boldsymbol{I}_{n-1} & \boldsymbol{0} \\ \boldsymbol{0} & \boldsymbol{I}_1 \end{pmatrix} \right]. \qquad (6.25)
\end{aligned}$$

Let us now consider the S-matrix blocks that correspond to NH + NH collisions, i.e. with unit incident flux in the asymptotic channels. Employing the general expression for the inverse of a block matrix,

$$\begin{pmatrix} \boldsymbol{a} & \boldsymbol{b} \\ \boldsymbol{c} & \boldsymbol{d} \end{pmatrix}^{-1} = \begin{pmatrix} (\boldsymbol{a} - \boldsymbol{b}\boldsymbol{d}^{-1}\boldsymbol{c})^{-1} & -(\boldsymbol{a} - \boldsymbol{b}\boldsymbol{d}^{-1}\boldsymbol{c})^{-1}\boldsymbol{b}\boldsymbol{d}^{-1} \\ -\boldsymbol{d}^{-1}\boldsymbol{c}(\boldsymbol{a} - \boldsymbol{b}\boldsymbol{d}^{-1}\boldsymbol{c})^{-1} & \boldsymbol{d}^{-1} + \boldsymbol{d}^{-1}\boldsymbol{c}(\boldsymbol{a} - \boldsymbol{b}\boldsymbol{d}^{-1}\boldsymbol{c})^{-1}\boldsymbol{b}\boldsymbol{d}^{-1} \end{pmatrix}, \qquad (6.26)$$

we obtain for the non-reactive scattering block $\overleftarrow{\boldsymbol{S}}_n$,

$$\begin{aligned}
\overleftarrow{\boldsymbol{S}}_n &= -\left[(\boldsymbol{F}^{(n)}_{n-1}\boldsymbol{O}_n - \boldsymbol{O}_{n-1}) - \boldsymbol{G}^{(n)}_{n-1}\boldsymbol{O}_0(\boldsymbol{G}^{(n)}_1\boldsymbol{O}_0 - \boldsymbol{O}_1)^{-1}\boldsymbol{F}^{(n)}_1\boldsymbol{O}_n \right]^{-1} \\
&\quad \times \left[(\boldsymbol{F}^{(n)}_{n-1}\boldsymbol{I}_n - \boldsymbol{I}_{n-1}) - \boldsymbol{G}^{(n)}_{n-1}\boldsymbol{O}_0(\boldsymbol{G}^{(n)}_1\boldsymbol{O}_0 - \boldsymbol{O}_1)^{-1}\boldsymbol{F}^{(n)}_1\boldsymbol{I}_n \right], \qquad (6.27)
\end{aligned}$$

and for the reactive block $\overleftarrow{\boldsymbol{S}}_0$ we find

$$\overleftarrow{\boldsymbol{S}}_0 = -(\boldsymbol{G}^{(n)}_1\boldsymbol{O}_0 - \boldsymbol{O}_1)^{-1}\boldsymbol{F}^{(n)}_1(\boldsymbol{I}_n + \boldsymbol{O}_n\overleftarrow{\boldsymbol{S}}_n). \qquad (6.28)$$

Note that this equation is expressed in terms of $\overleftarrow{\boldsymbol{S}}_n$. In order to evaluate Eqs. (6.27) and (6.28), we also require explicit forms for the different incoming and outgoing waves. Asymptotically open channels, with channel energy $\epsilon^{(n)}_p < E$ and wavenumber $k^{(n)}_p$, are flux-normalized to [see also Eqs. (1.23) – (1.26)]

$$\begin{aligned}
\boldsymbol{I}_i &= \tilde{\boldsymbol{U}}_n\tilde{\boldsymbol{I}}_i, \\
(\tilde{\boldsymbol{I}}_i)_{p,q} &= \sqrt{\frac{\mu k^{(n)}_p}{\hbar}} R_i h^{(2)}_{l_p}(k^{(n)}_p R_i)\delta_{p,q}, \qquad (6.29) \\
\boldsymbol{O}_i &= \tilde{\boldsymbol{U}}_n\tilde{\boldsymbol{O}}_i, \\
(\tilde{\boldsymbol{O}}_i)_{p,q} &= \sqrt{\frac{\mu k^{(n)}_p}{\hbar}} R_i h^{(1)}_{l_p}(k^{(n)}_p R_i)\delta_{p,q}, \qquad (6.30)
\end{aligned}$$

with $\tilde{\boldsymbol{U}}_n$ representing the orthogonal matrix of asymptotic channel eigenfunctions, μ is the reduced mass, and $h_{l_p}^{(1)}$ and $h_{l_p}^{(2)}$ are spherical Hankel functions of the first and second kind, respectively, for partial wave l_p. We match the asymptotically closed channels, with $\epsilon_p^{(n)} > E$, to functions with zero flux,

$$(\tilde{\boldsymbol{O}}_i)_{p,q} \;=\; R_i k_{l_p}(k_p^{(n)} R_i)\delta_{p,q}, \tag{6.31}$$

with k_{l_p} denoting the modified spherical Bessel function of the second kind. Incoming waves for closed channels are not considered here. We note that by discarding the incident flux in asymptotically closed channels, the $\overleftarrow{\boldsymbol{S}}_n$ and $\overleftarrow{\boldsymbol{S}}_0$ matrices become rectangular rather than square. The columns of the full S-matrix remain orthonormal, however, and hence the relation $\boldsymbol{S}^\dagger \boldsymbol{S} = \boldsymbol{1}$ is preserved.

In the short range, we take the adiabatic eigenvalues $\epsilon_p^{(0)}$ at $R = R_0$ as local channel energies and assume that these vary linearly with R [135]. The slope α_p of the adiabats between R_0 and R_1 is used to distinguish between open and closed reactive channels. We assume that adiabats with $\alpha_p > 0$ will become energetically accessible at some small R ($R \leq R_0$), and hence we define the corresponding channels as “open”. For these channels, the flux-normalized outgoing waves are given by

$$\begin{aligned}
\boldsymbol{O}_i &= \tilde{\boldsymbol{U}}_0 \tilde{\boldsymbol{O}}_i, \\
(\tilde{\boldsymbol{O}}_i)_{p,q} &= \sqrt{\frac{\mu\pi}{x}} \left\{ \mathrm{Ai}([R_i - R_0]x + [\epsilon_p^{(0)} - E]x/\alpha_p) \right. \\
&\quad \left. + j\,\mathrm{Bi}([R_i - R_0]x + [\epsilon_p^{(0)} - E]x/\alpha_p) \right\} \delta_{p,q},
\end{aligned} \tag{6.32}$$

where $\tilde{\boldsymbol{U}}_0$ represents the matrix of adiabatic eigenfunctions at the point $R = R_0$, $x = (2\mu\alpha_p/\hbar^2)^{1/3}$, Ai and Bi are Airy functions [131], and $j = \sqrt{-1}$. Channels with $\alpha_p < 0$ are considered locally closed, since the corresponding adiabats will eventually become repulsive at $R \leq R_0$. These channels are matched with real-valued, exponentially decaying functions,

$$(\tilde{\boldsymbol{O}}_i)_{p,q} = \mathrm{Ai}([R_i - R_0]x + [\epsilon_p^{(0)} - E]x/\alpha_p)\delta_{p,q}, \tag{6.33}$$

where x is the real cube root of $2\mu\alpha_p/\hbar^2$, i.e. $x = \mathrm{sgn}(\alpha_p)(2\mu|\alpha_p|/\hbar^2)^{1/3}$. Incoming waves at small R are not considered in our calculations. Thus, once the reaction proceeds, the products cannot be converted back into a reactant configuration.

Instead of assuming that the adiabats vary linearly with R in the short range, we may also assume that they are constant when $R \approx R_0$. In that case, we should match with functions of the form $(\mu/\hbar k_p^{(0)})^{-1/2} \exp(-j k_p^{(0} R_i)$ rather than Airy functions. Locally closed channels, now defined by $(k_q^{(0)})^2 < 0$, can be matched as $\sim \exp(|k_q^{(0)}| R_i)$. We have verified that both conventions give approximately the same results, with differences on the order of 1 percent. The results presented here are obtained using the Airy function convention.

By using Eqs. (6.29) to (6.31) for points $i = n$ and $i = n - 1$, and Eqs. (6.32) and (6.33) for $i = 0$ and $i = 1$, we may evaluate Eqs. (6.27) and (6.28) to obtain the relevant

S-matrices. The elastic and inelastic cross sections can be calculated in the usual way [see e.g. Eq. (1.30)] using the transmission T-matrix $\overleftarrow{\boldsymbol{T}}_n = \mathbf{1} - \overleftarrow{\boldsymbol{S}}_n$. In order to extract the total reactive cross sections, we must first point out that the reactive channels at R_0 lack a well-defined partial-wave quantum number l and corresponding space-fixed projection m_l. Hence, for a given initial state $|q_A, q_B\rangle$, we calculate the reactive cross section as

$$\sigma^{\text{reactive}}_{q_A,q_B} = \frac{\pi}{k_q^2}\sum_{l,m_l}\sum_{q_{AB}}\left|\left(\overleftarrow{\boldsymbol{T}}_0\right)_{q_{AB};q_A,q_B,l,m_l}\right|^2, \tag{6.34}$$

where k_q^2 denotes the squared wavenumber for the incident channel, q_{AB} labels the reactive channels, and the T-matrix is defined by $\overleftarrow{\boldsymbol{T}}_0 = \mathbf{0} - \overleftarrow{\boldsymbol{S}}_0$. As in the non-reactive case, the cross sections must be multiplied by a factor of 2 if the molecules are identical particles in the same initial states.

6.2.3 Computational details

We have performed reactive scattering calculations for $^{15}\mathrm{NH}(X\,^3\Sigma^-)$ + $^{15}\mathrm{NH}(X\,^3\Sigma^-)$ both in the presence and absence of an external magnetic field. The field-free calculations were carried out using a total angular momentum ($\mathcal{J}$) representation, as described in Chapter 3. The scattering calculations in a magnetic field were performed for fixed values of the space-fixed total angular momentum projection $\mathcal{M}$ (see Chapter 4). The Hamiltonian and channel basis set for the field-free calculations are given by Eqs. (3.1) – (3.3) and (3.8), respectively, and for scattering in a magnetic field we used Eqs. (4.1) – (4.3) and (4.13). The Hamiltonian contained the potential energy surfaces for all three spin states of the NH–NH complex ($S = 0, 1$, and 2). We have found that the quintet ($S = 2$) interaction energies calculated at the CASPT2 level of theory are in slightly better agreement with the RCCSD(T) results than the CASPT3 data, and hence we have used the CASPT2 data for the singlet ($S = 0$) and triplet ($S = 1$) potentials [see Eq. (2.1)]. The asymptotic monomer eigenfunctions were obtained by separately diagonalizing the monomer Hamiltonians $\hat{H}_A$ and $\hat{H}_B$. The collision cross sections for two magnetically trapped NH molecules were calculated using Eq. (3.17) (see Secs. 3.2 and 4.2 for more details). All calculations were carried out in Matlab [118].

The channel basis sets were truncated at a certain value of the monomer rotational angular momentum, $N_{\max}$, and at a certain maximum of the partial-wave angular momentum, $l_{\max}$ (denoted as $L_{\max}$ in Chapters 3 and 4). The field-free calculations were performed for $N_{\max} = 6$ and $l_{\max} = 6$, and for the calculations in a magnetic field we used $N_{\max} = 2$ and $l_{\max} = 6$. We considered only channel functions with even permutation symmetry and even parity. As outlined on p. 45 and 63, this symmetry type allows for s-wave ($l = 0$) collisions between identical bosonic molecules in the same initial quantum state. The angular expansions of the potentials [Eq. (3.4)] were truncated at $L_A = L_B = 8$. The radial propagation was carried out using the renormalized Numerov algorithm described above. The minimum number of grid points per smallest de Broglie wavelength was set to 10, and the propagation step size was doubled whenever the smallest wavelength increased by a factor of 2. The radial grid ranged from $R_0 = 4.5$ to $R_n = 500\ a_0$ for the field-free calculations, and from $R_0 = 4.5$ to $R_n = 1500\ a_0$ for scattering in a magnetic field. The cross sections were calculated for collision energies ranging from 10^{-6} to 1 K, and for magnetic field strengths ranging from 10^{-1} to 10^4 G.

As a final point, we note that the Bi functions appearing in Eq. (6.32) tend to infinity if $\alpha_p \to 0$. For numerical reasons, we have set an upper bound of 10^{10} on these function values. We have verified that this has a negligible effect on the cross sections.

6.3 Results and discussion

6.3.1 Energy dependence

We begin by discussing the collision cross sections for magnetically trapped ^{15}NH in the presence of an external field. Figure 6.5 shows the elastic, spin-inelastic, and reactive cross sections as a function of the collision energy E for a total angular momentum projection of $\mathcal{M} = 2$ and a magnetic field of $B = 1$ G. Note that $\mathcal{M} = 2$ corresponds to s-wave collisions in the entrance channel, i.e. the channel with monomer spin-projection quantum numbers $M_{S_A} = M_{S_B} = 1$. We find that the elastic cross section at small E becomes constant as a function of energy, consistent with Wigner's threshold law for elastic s-wave scattering [see Eq. (3.18)]. Both the inelastic and reactive cross sections exhibit $E^{-1/2}$ threshold behaviour, as expected from the $E^{l-1/2}$ law for exoergic processes with $l = 0$ [119]. In order to compare our results with the non-reactive case, we have also plotted the cross sections obtained from scattering calculations on the non-reactive quintet potential. We have verified that, when including only the $S = 2$ surface, our renormalized Numerov reactive scattering code gives the same results as the modified MOLSCAT code [116, 117] used in previous chapters. As can be seen in Fig. 6.5, the inclusion of chemically reactive ($S = 0$ and 1) potentials has an almost negligible effect on the elastic and spin-inelastic cross sections. This confirms our expectations described in Chapter 3 (see p. 53). We thus conclude that most of the non-reactive, inelastic trap loss occurs on the quintet surface, and that collisions on the $S = 0$ and 1 potentials are almost 100% reactive.

Figure 6.5 also indicates that reactive collisions can compete quite strongly with elastic ones, and hence we must reconsider the prospects for molecular evaporative cooling. The fact that (for $B = 1$ G) the elastic-to-reactive cross section ratio is much smaller than the elastic-to-inelastic ratio suggests that evaporative cooling of magnetically trapped NH might be more difficult than previously expected. We will return to this topic later, when discussing the effect of uncertainties in the potentials.

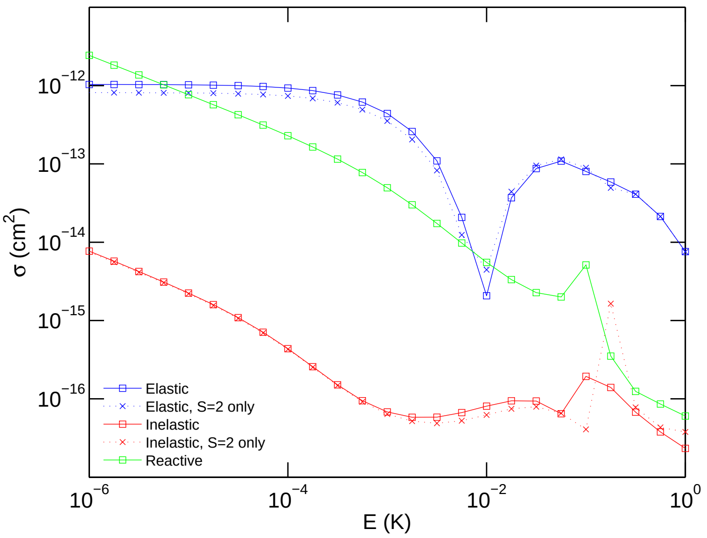

Figure 6.5: Cross sections for magnetically trapped ^{15}NH + ^{15}NH as a function of collision energy, calculated for $\mathcal{M} = 2$ at a magnetic field strength of 1 G. The solid lines were obtained by including all three NH + NH potential energy surfaces in the scattering calculations, while the dotted lines were obtained using only the non-reactive quintet potential.

6.3.2 Magnetic-field dependence

In Fig. 6.6, we present the collision cross sections for $\mathcal{M} = 2$ as a function of magnetic field, calculated at a collision energy of 10^{-6} K. We have already established in Chapters 4 and 5 that the intermolecular magnetic dipolar term is the dominant source of inelastic trap loss at ultralow energies. Indeed, when discarding the intermolecular magnetic dipole-dipole coupling ($V_{\text{magn.dip}}$) in our reactive scattering calculations, the spin-inelastic cross section decreases by several orders of magnitude. As discussed on p. 80, the threshold behaviour of the inelastic cross section is $\sigma \sim B^{1/2-l_{\text{in}}}$ when the magnetic dipole-dipole coupling is switched on, and $\sigma \sim B^{1/2+l_{\text{out}}}$ otherwise. The quantum numbers l_{in} and l_{out} represent the partial waves for the incoming and outgoing channels, respectively. The $B^{1/2+l_{\text{out}}}$ result holds when the *intramolecular* couplings are dominant.

Let us now consider the *reactive* cross sections as a function of magnetic field. We have found that the intermolecular spin-spin term induces virtually no reactivity, while the intramolecular spin-spin coupling ($V_{\text{intra}-\text{SS}}$) has a very large effect on the reactive cross section. As can be seen in Fig. 6.6, the reactive cross sections become much smaller when the intramolecular coupling is switched off. This can also be understood by considering that the intermolecular spin-spin interaction is long-ranged, while a chemical reaction can only proceed when the reactants approach each other to a very short distance. Hence, the intramolecular spin-spin coupling, which acts through the potential anisotropy at short range [86, 57], plays the most important role in the reaction process. The reactive cross sections reveal, however, different threshold behaviour

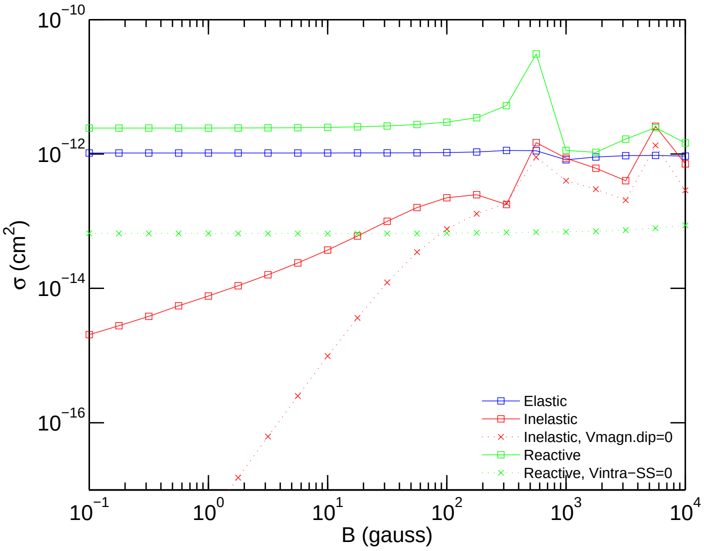

Figure 6.6: Cross sections for magnetically trapped ^{15}NH + ^{15}NH as a function of magnetic field, calculated for $\mathcal{M} = 2$ at a collision energy of 10^{-6} K. The spin-inelastic cross sections obtained with the intermolecular magnetic dipole term switched off, and the reactive cross sections obtained with the intramolecular spin-spin coupling switched off, are also plotted.

than the inelastic cross sections due to $V_{\text{intra}-\text{SS}}$. Since the reaction can proceed without having to overcome any centrifugal barrier in the outgoing channel, the reactive cross section behaves as B^0 rather than $B^{1/2+l_{\text{out}}}$. This B^0 result is essentially a consequence of the $E^{l_{\text{in}}-1/2}$ Wigner law for exothermic collisions. If the scattering process is strongly exothermic, as is the case for the NH + NH reactions considered in this work, the threshold behaviour is determined only by the centrifugal barrier in the entrance channel. That is, the energy of the outgoing (reactive) channel has no effect on the collision cross section.

If the exoergodicity of reaction is still sufficiently large at $B = 0$, we may expect the B^0 threshold regime to extend down to zero field. Figure 6.7 compares the scattering results for different magnetic field strengths, including $B = 0$, as a function of collision energy. All calculations were performed with the same channel basis set ($N_{\text{max}} = 2$, $l_{\text{max}} = 6$, $\mathcal{M} = 2$). We find that the reactive cross sections obtained from field-free calculations are in excellent agreement with the results for $B = 0.1, 1$, and 100 G, and deviate only at a relatively high field of $B = 1000$ G. Thus, the B^0 regime holds from $B = 0$ to $B \approx 100$ G for virtually all collision energies considered. It can also be seen that the *inelastic* cross sections are different for all B values, and they also show different threshold behaviour as a function of energy. When the magnetic field is decreased from $B \neq 0$ to $B = 0$, the spin-changing collisions become isoergic rather than exoergic, and the threshold behaviour changes from $E^{l_{\text{in}}-1/2}$ to $E^{l_{\text{in}}+l_{\text{out}}}$ [Eq. (3.18)]. A more detailed analysis on these inelastic threshold regimes is given in Secs. 3.3, 4.3, and 5.3.

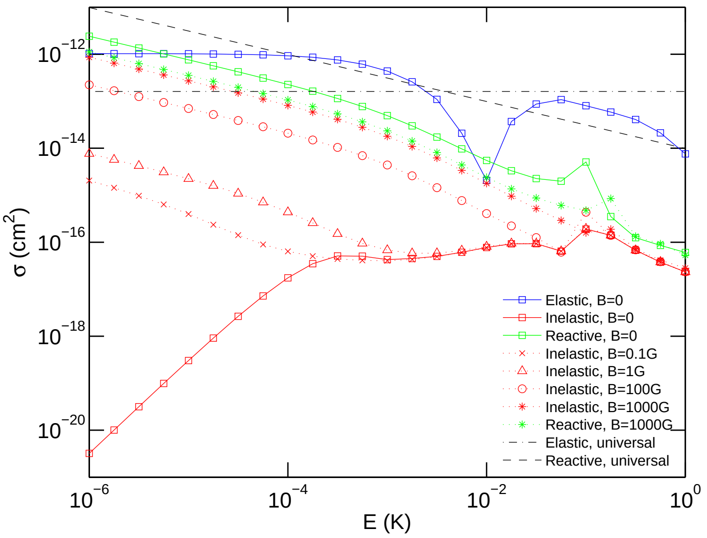

Figure 6.7: Cross sections for magnetically trapped ^{15}NH + ^{15}NH as a function of collision energy, calculated for $\mathcal{M} = 2$ at various magnetic field strengths. The elastic cross sections are the same for all magnetic fields considered, and the reactive cross sections are the same for $B = 0, 0.1, 1,$ and 100 G. The results of the universal quantum-defect model [Eqs. (6.35) and (6.36)] are also shown for comparison.

6.3.3 Scattering in the universal limit

We now turn to the topic of universality. In order to establish whether the ultracold chemistry of NH + NH is universal, we compare our scattering results with the single-channel quantum-defect model of Idziaszek and Julienne [134]. This model parametrizes the collision dynamics in terms of two dimensionless parameters, s and y, which represent a reduced scattering length and short-range reaction probability, respectively. In the universal limit, y is unity and all scattering flux that reaches the short range disappears into (exoergic) reactive channels. The role of the long-range potential is to determine how much of the entrance-channel wave is transmitted to short range to experience such reactive "loss" dynamics. For a single isotropic potential, the universal elastic and reactive cross sections for s-wave collisions are given by [134]

$$\sigma_{\text{elastic}}(k) \quad = \quad 4g\bar{a}^2, \tag{6.35}$$

$$\sigma_{\text{reactive}}(k) \quad = \quad 2g\frac{\bar{a}}{k}, \tag{6.36}$$

where k is the wavenumber for the entrance channel. The symmetry factor g takes the value of 1 except when both particles are identical species in identical internal states, in which case $g = 2$. The parameter $\bar{a}$ denotes the mean scattering length; it is related to the van der Waals radius $R_6 = \frac{1}{2}(2\mu C_6/\hbar^2)^{1/4}$ as $\bar{a} = 4\pi R_6/\Gamma(1/4)^2$, with Γ being the Gamma function (see also Ref. [136]).

For the isotropic C_6 coefficient of NH + NH, we take the fitted electronic second-order (dispersion/induction) coefficient calculated in Chapter 2, $C_6^{\text{elec}} = 47.27$ a.u., plus a term arising from the mixing of rotational states due to the electric dipole-dipole interaction ($C_6^{\text{dip-dip}}$). The latter contribution can be understood as follows. The dipole-dipole interaction, which decays asymptotically as R^{-3}, averages out to zero when one of the molecules is freely rotating, but it gives a nonzero contribution in second-order perturbation theory. More specifically, the dipolar interaction mixes a rotational state N with $N \pm 1$, leading to an effective R^{-6} isotropic interaction. For two linear molecules that are initially in their rotational ground states, $N_i = 0$ $(i = 1, 2)$, the corresponding long-range coefficient is $C_6^{\text{dip-dip}} = \frac{1}{3}\mu_1^2\mu_2^2/(B_1 + B_2)$. Here, μ_1 and μ_2 are the permanent electric dipole moments of molecule 1 and 2, respectively, and B_1 and B_2 are the molecular rotational constants. For ^{15}NH + ^{15}NH, we have $\mu_1 = \mu_2 = 1.52$ D and $B_1 = B_2 = 16.27034$ cm^{-1}, so that $C_6^{\text{dip-dip}} = 291.18$ a.u. Note that this term is about six times larger than the electronic contribution. With a total C_6 coefficient of $C_6^{\text{elec}} + C_6^{\text{dip-dip}} = 338.45$ a.u., we thus obtain, for the mean scattering length, $\bar{a} = 26.80\ a_0$. The universal elastic and reactive cross sections for two magnetically trapped ^{15}NH molecules follow directly from Eqs. (6.35) and (6.36).

Figure 6.7 compares the results of the universal quantum-defect model with those of the numerical coupled-channels calculations. In the s-wave regime ($E < 10^{-3}$ K), the universal elastic cross sections differ by a factor of ~ 6 from the numerical values, while the universal reactive cross sections are about 4 times larger than the (field-free) numerical data. These differences suggest that the NH + NH reaction dynamics is non-universal, and that a significant fraction of the incident flux is reflected by the repulsive wall of the quintet potential. It should be noted, however, that the quantum-defect results apply to single-channel scattering on a single isotropic potential, while the numerical data have been obtained from multi-channel calculations on three coupled anisotropic potential energy surfaces. Nevertheless, the collision dynamics in the ultracold regime is s-wave dominated, and the isotropic C_6 term gives the largest contribution to the effective long-range potential. Thus, the quantum-defect model should provide a reasonable estimate of the universal NH + NH reaction probability.

6.3.4 Sensitivity to potentials and basis-set size

A more direct way to establish the degree of universality is to test the effect of small modifications in the (short-range) potentials. If the scattering is universal, the cross sections are completely determined by the long-range features of the interaction potentials. For instance, a scaling of the C_6 coefficient by a factor of λ (or, equivalently, a scaling of the reduced mass by λ) should change the universal elastic cross section by $\lambda^{1/2}$ [Eq. (6.36)]. Figure 6.8 shows the universal quantum-defect results as a function of the scaling parameter λ ($0.9 \leq \lambda \leq 1.1$) for a collision energy of 10^{-6} K. The corresponding numerical elastic, inelastic, and reactive cross sections, obtained by reduced-mass scaling, are also shown for $\mathcal{M} = 2$ and $B = 1$ and 100 G. It is evident that the numerical results are highly sensitive to the details of the potentials, and that the universal model is inaccurate for all values of λ. In fact, the resonance features in the numerical cross sections are signatures of non-universal behaviour [137] and high-light the importance of short-range physics in the dynamics. We thus conclude that the scattering properties of magnetically trapped NH cannot be captured in a universal model.

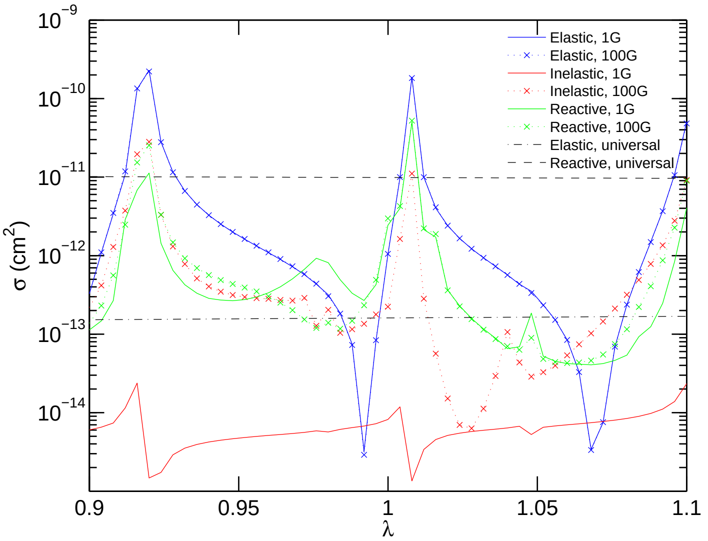

Figure 6.8: Cross sections for magnetically trapped ^{15}NH + ^{15}NH ($\mathcal{M} = 2$) as a function of the scaling factor λ, calculated for two magnetic field strengths ($B = 1$ and 100 G) at a collision energy of 10^{-6} K. The results of the universal quantum-defect model [Eqs. (6.35) and (6.36)] are also shown.

As discussed extensively in Chapters 3 and 4, the λ-scaling approach also provides a means to sample the effects of uncertainties in the interaction potentials. Since the exact NH–NH potential energy surfaces (and thus the 'exact' λ value) are unknown, the calculated numerical cross sections are subject to an inherent degree of uncertainty. This also carries implications for the prospects for molecular evaporative cooling. More specifically, one should evaluate the elastic-to-reactive cross section ratio for all relevant λ values to obtain a realistic estimate of the cooling efficiency. In the case of $\lambda = 1$, we find that reactive NH + NH collisions are more probable than elastic ones (cf. Figs. 6.6 and 6.7), while for $\lambda \approx 0.95$ and $\lambda \approx 1.03$ the elastic cross sections are about one order of magnitude larger than the reactive ones. These results suggest that evaporative cooling of magnetically trapped NH is still feasible, but the probability of success is significantly smaller than estimated earlier from non-reactive scattering calculations.

It can also be seen in Fig. 6.8 that the inelastic cross sections change rather dramatically from $B = 1$ to 100 G, while the reactive cross sections show only a weak dependence on magnetic field. Nevertheless, for certain values of λ, the reactivity can increase by almost one order of magnitude as the magnetic field strength is changed. Thus, it may be possible to control the NH + NH reaction rate by means of an external field. For most λ values, however, the reactive cross sections show B^0 behaviour and magnetic field control will not be possible. We note that the final product-state distribution might be more sensitive to the magnetic field strength than the *total* reaction

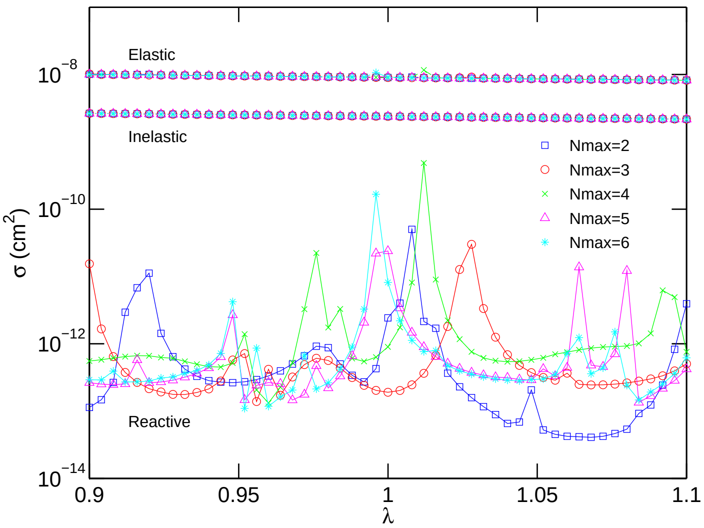

Figure 6.9: Collision cross sections for magnetically trappable ^{15}NH in the absence of a magnetic field, calculated for $\mathcal{J} = 2$ and $E = 10^{-6}$ K as a function of the scaling factor λ. Different symbols correspond to different rotational basis sets.

probability, but our scattering method does not allow the calculation of product-state-resolved reaction cross sections.

As a final point, we consider the convergence of the channel basis set. The reactive scattering results discussed so far have been obtained with $N_{\rm max} = 2$, while a fully converged calculation requires as least $N_{\rm max} = 6$ (see Sec. 3.3.3). It is infeasible at present to use such a large basis set in the decoupled channel representation [Eq. (4.13)] for scattering in a magnetic field. For field-free calculations, however, in which a total angular momentum representation is used, it might be possible to obtain full convergence. In Fig. 6.9, we present the results for $\mathcal{J} = 2$ as a function of λ at a collision energy of 10^{-6} K. We have verified that, for $N_{\rm max} = 2$, this $\mathcal{J}$ value gives the largest contribution to the reactive cross sections. Calculations for other $\mathcal{J}$ values ($N_{\rm max} > 2$) are currently ongoing. It can be seen that the elastic and inelastic cross sections for $\mathcal{J} = 2$ are virtually independent of λ, while the reactive cross sections exhibit a rich resonance structure. This can also be understood by considering that reactive collisions are governed mainly by the intramolecular spin-spin coupling, which relies on the mixing of different rotational states. Increasing the rotational basis set may thus have a relatively strong effect on the reactivity. We also find that the cross sections for $\mathcal{J} = 2$ are nearly converged for $N_{\rm max} = 6$, suggesting that a fully converged scattering calculation for NH($X\,^3\Sigma^-$) + NH($X\,^3\Sigma^-$) is feasible. Finally, we note that the reactive cross sections for different basis sets all vary around approximately the same background value, and the number of resonances is fairly constant. This is consistent with our findings of the previous chapters. Since we expect to find a similar convergence pattern for reactive scattering in a magnetic field, we argue that the prospects for magnetically controlled NH + NH chemistry can be reasonably assessed based on our $N_{\rm max} = 2$ data. That is, external field control of NH + NH reactions might be possible, but the efficiency of the process will probably be fairly low.

6.4 Concluding remarks

In this chapter, we have presented a novel single-arrangement quantum reactive scattering method based on the renormalized Numerov propagation technique. An important feature of the method is that it provides a *complete* set of linearly independent solutions of the coupled-channels equations. Thus, once the propagation is completed, we can impose any desired scattering boundary conditions to obtain the scattering S-matrix. We have applied our algorithm to the case of cold and ultracold NH($X\,^3\Sigma^-$) + NH($X\,^3\Sigma^-$) reactive scattering, both in the presence and absence of an external magnetic field. We have found that most of the non-reactive collisions for magnetically trapped NH take place on the quintet potential energy surface, while collisions on the singlet and triplet interaction potentials are almost fully reactive. Chemical reactivity is induced mainly by the intramolecular spin-spin coupling, which acts through the anisotropy of the different potentials. Our results also show that the reactive cross section generally behaves as B^0 for fields below $B \approx 100$ G, and that the dynamics is far from universal. The fact that the reaction rate is only weakly dependent on field strength makes external field control of cold NH + NH reactions rather difficult. Taking into account the uncertainty in the potentials, however, we argue that cold controlled chemistry of NH radicals may still be possible. Furthermore, we have re-evaluated the prospects for evaporative cooling of magnetically trapped NH. Our results indicate that reactive scattering processes can compete strongly with elastic NH + NH collisions, making evaporative cooling more difficult than previously anticipated. Nevertheless, based on a sampling of the uncertainty range of the interaction potentials, we conclude that efficient evaporative cooling of NH might remain feasible. Finally, we note that the reactive scattering results discussed so far have been performed with an incompletely converged channel basis set. Although we expect our qualitative findings to be fairly independent of the size of the basis, we are currently undertaking scattering calculations for larger basis sets to obtain a more reliable assessment of the prospects for cold controlled NH + NH chemistry and evaporative cooling.

With this chapter, we conclude our study of the NH + NH collision dynamics in the (ultra)cold regime. The four-dimensional *ab initio* potentials for the NH($X\,^3\Sigma^-$) + NH($X\,^3\Sigma^-$) system have been used in non-reactive and reactive quantum scattering calculations, both in a field-free environment and in the presence of a magnetic field. We have identified and analyzed the main mechanisms that govern the various NH + NH collision processes, and have provided a general analytical model for spin-inelastic collisions due to the intermolecular magnetic dipolar interaction. Our results show that NH is a potentially suitable candidate for molecular evaporative cooling, but the probability of success is limited by the presence of chemically reactive channels. Furthermore, it was found that the reactivity can be controlled by means of an applied magnetic field, although the efficiency is expected to be rather low. A more detailed study of the chemical reaction dynamics will require full six-dimensional potential energy surfaces for the different spin states of the NH–NH complex. In particular, such potentials could allow for the calculation of product-state distributions of cold NH + NH reactions. A six-dimensional quantum treatment of the NH + NH system on the coupled singlet, triplet, and quintet potential energy surfaces is, however, infeasible at present, both in terms of methodology and computational costs.

Throughout this thesis, we have also addressed two more general points concerning quantum scattering calculations, namely the effect of inaccuracies in the *ab initio* potentials and the size of the channel basis set. At low and ultralow collision energies, the calculated cross sections are highly sensitive to the details of the potential energy surfaces, which is due to the presence of (quasi-)bound-state resonances. Since the *exact* potentials are generally unknown, the predicted cross sections for a given energy and magnetic field are subject to an inherent degree of uncertainty. Thus, in order to give a reliable picture of the scattering behaviour at (ultra)low energies, we must take into account the inaccuracies of the interaction potentials. As a consequence, we can only predict the *likelihood* that evaporative cooling and magnetically controlled chemistry experiments will succeed, rather than providing an exact number for the collision cross sections. In view of this uncertainty, one may also reconsider the need to use a fully converged channel basis set in the scattering calculations. We have found that our qualitative results and conclusions are fairly independent of the size of the basis set, and that even an incompletely converged basis can provide a reliable estimate of, e.g., the probability for successful evaporative cooling. These findings are particularly useful for open-shell systems such as NH + NH, for which full basis set convergence is extremely difficult to achieve.

Bibliography

[1] G. Amontons, Histoire de l'Académie Royale des Sciences avec les Mémoires de Mathématique et de Physique, 50 (1703).

[2] *Library of useful knowledge: Natural philosophy*, Society for the Diffusion of Useful Knowledge, Great Britian, Chapter VIII, 39 (1829).

[3] W. Thomson, Cambridge Philosophical Society Proceedings, 66 (1848).

[4] Resolution 3, Comptes Rendus de la 10e Conférence Générale des Poids et Mesures (1954).

[5] Annals of Philosophy, Article XI: Proceedings of Philosophical Societies, 304 (1823).

[6] R. Pictet, Comptes Rendus Hebdomadaires des Séances de l'Académie des Sciences **85**, 1214 (1877).

[7] L. Cailletet, Comptes Rendus Hebdomadaires des Séances de l'Académie des Sciences **85**, 1213 (1877).

[8] S. Wróblewski and K. Olszewski, Annal. Phys. Chem. **20**, 243 (1883).

[9] J. Dewar, Proc. R. Soc. London **63**, 256 (1898).

[10] H. Kamerlingh Onnes, KNAW Proceedings **11**, 168 (1908).

[11] H. Kamerlingh Onnes, KNAW Proceedings **14**, 113 (1911).

[12] P. Kapitza, Nature **141**, 74 (1938).

[13] J. Allen and A. Misener, Nature **141**, 75 (1938).

[14] F. London, Nature **141**, 643 (1938).

[15] S. N. Bose, Z. Phys. **26**, 178 (1924).

[16] A. Einstein, Sitzber. Kgl. Preuss. Akad. Wiss. 261 (1924); Sitzber. Kgl. Preuss. Akad. Wiss. 3 (1925).

[17] M. H. Anderson, J. R. Ensher, M. R. Matthews, C. E. Wieman, and E. A. Cornell, Science **269**, 198 (1995).

[18] K. B. Davis, M.-O. Mewes, M. R. Andrews, N. J. van Druten, D. S. Durfee, D. M. Kurn, and W. Ketterle, Phys. Rev. Lett. **75**, 3969 (1995).

[19] I. Bloch, J. Dalibard, and W. Zwerger, Rev. Mod. Phys. **80**, 885 (2008).

[20] M. Greiner, C. A. Regal, and D. S. Jin, Nature **426**, 537 (2003).

[21] S. Jochim, M. Bartenstein, A. Altmeyer, G. Hendl, S. Riedl, C. Chin, J. H. Denschlag, and R. Grimm, Science **302**, 2101 (2003).

[22] W. Hofstetter, J. I. Cirac, P. Zoller, E. Demler, and M. D. Lukin, Phys. Rev. Lett. **89**, 220407 (2002).

[23] S. S. Kondov, W. R. McGehee, J. J. Zirbel, and B. DeMarco, Science **334**, 66 (2011).

[24] M. Greiner, O. Mandel, T. Esslinger, T. W. Hänsch, and I. Bloch, Nature **415**, 39 (2002).

[25] T. Kraemer *et al.*, Nature **440**, 315 (2006).

[26] R. J. Rafac, B. C. Young, J. A. Beall, W. M. Itano, D. J. Wineland, and J. C. Bergquist, Phys. Rev. Lett. **85**, 24622465 (2000).

[27] J. Ye, H. J. Kimble, and H. Katori, Science **320**, 1734 (2008).

[28] G. Lamporesi, A. Bertoldi, L. Cacciapuoti, M. Prevedelli, and G. M. Tino, Phys. Rev. Lett. **100**, 050801 (2008).

[29] A. Gorshkov, A. M. Rey, A. J. Daley, M. M. Boyd, J. Ye, P. Zoller, and M. D. Lukin, Phys. Rev. Lett. **102**, 110503 (2009).

[30] D. DeMille, Phys. Rev. Lett. **88**, 067901 (2002).

[31] A. Micheli, G. K. Brennen, and P. Zoller, Nat. Phys. **2**, 341 (2006).

[32] L. D. Carr, D. DeMille, R. V. Krems, and J. Ye, New J. Phys. **11**, 055049 (2009).

[33] T. Zelevinsky, S. Kotochigova, and J. Ye, Phys. Rev. Lett. **100**, 043201 (2008).

[34] C. Chin, V. V. Flambaum, and M. G. Kozlov, New J. Phys. **11**, 055048 (2009).

[35] J. J. Hudson, D. M. Kara, I. J. Smallman, B. E. Sauer, M. R. Tarbutt, and E. A. Hinds, Nature **473**, 493 (2011).

[36] K.-K. Ni, S. Ospelkaus, D. Wang, G. Quéméner, B. Neyenhuis, M. H. G. de Miranda, J. L. Bohn, J. Ye, and D. S. Jin, Nature **464**, 13241328 (2010).

[37] R. V. Krems, Phys. Chem. Chem. Phys. **10**, 4079 (2008).

[38] E. L. Raab, M. Prentiss, A. Cable, S. Chu, and D. E. Pritchard, Phys. Rev. Lett. **59**, 26312634 (1987).

[39] E. S. Shuman, J. F. Barry, and D. DeMille, Nature **467**, 820 (2010).

[40] K. M. Jones, E. Tiesinga, P. D. Lett, and P. S. Julienne, Rev. Mod. Phys. **78**, 483 (2006).

[41] T. Köhler, K. Góral, and P. S. Julienne, Rev. Mod. Phys. **78**, 1311 (2006).

[42] K. Bergmann, H. Theuer, and B. W. Shore, Rev. Mod. Phys. **70**, 10031025 (1998).

[43] M. Viteau, A. Chotia, M. Allegrini, N. Bouloufa, O. Dulieu, D. Comparat, and P. Pillet, Science **321**, 232 (2008).

[44] S. Ospelkaus, K. K. Ni, D. Wang, M. H. G. de Miranda, B. Neyenhuis, G. Quéméner, P. S. Julienne, J. L. Bohn, D. S. Jin, and J. Ye, Science **327**, 853 (2010).

[45] M. H. G. de Miranda, A. Chotia, B. Neyenhuis, D. Wang, G. Quéméner, S. Ospelkaus, J. L. Bohn, J. Ye, and D. S. Jin, Nat. Phys. **7**, 502 (2011).

[46] H. L. Bethlem and W. Ubachs, Faraday Discuss. **142**, 25 (2009).

---

[47] J. D. Weinstein, R. deCarvalho, T. Guillet, B. Friedrich, and J. M. Doyle, Nature **395**, 148 (1998).

[48] S. C. Doret, C. B. Connolly, W. Ketterle, and J. M. Doyle, Phys. Rev. Lett. **103**, 103005 (2009).

[49] E. Narevicius, A. Libson, C. G. Parthey, I. Chavez, J. Narevicius, U. Even, and M. G. Raizen, Phys. Rev. A **77**, 051401 (2008).

[50] H. L. Bethlem and G. Meijer, Int. Rev. Phys. Chem. **22**, 73 (2003).

[51] M. S. Elioff, J. J. Valentini, and D. W. Chandler, Science **302**, 1940 (2003).

[52] T. Rieger, T. Junglen, S. A. Rangwala, P. W. H. Pinkse, and G. Rempe, Phys. Rev. Lett. **95**, 173002 (2005).

[53] W. Ketterle and N. J. van Druten, Adv. Atom. Mol. Opt. Phys. **37**, 181 (1996).

[54] C. R. Monroe, E. A. Cornell, C. A. Sackett, C. J. Myatt, and C. E. Wieman, Phys. Rev. Lett. **70**, 414 (1993).

[55] L. A. Poveda, M. Biczysko, and A. J. C. Varandas, J. Chem. Phys. **131**, 044309 (2009).

[56] C.-H. Lai, M.-D. Su, and S.-Y. Chu, J. Phys. Chem. A **107**, 2700 (2003).

[57] R. V. Krems, H. R. Sadeghpour, A. Dalgarno, D. Zgid, J. Kłos, and G. Chałasiński, Phys. Rev. A **68**, 051401 (2003).

[58] W. C. Campbell, E. Tsikata, H.-I. Lu, L. D. van Buuren, and J. M. Doyle, Phys. Rev. Lett. **98**, 213001 (2007).

[59] M. T. Hummon, W. C. Campbell, H.-I. Lu, E. Tsikata, Y. Wang, and J. M. Doyle, Phys. Rev. A **78**, 050702 (2008).

[60] W. C. Campbell, G. C. Groenenboom, H.-I. Lu, E. Tsikata, and J. M. Doyle, Phys. Rev. Lett. **100**, 083003 (2008).

[61] M. T. Hummon, T. V. Tscherbul, J. Kłos, H.-I. Lu, E. Tsikata, W. C. Campbell, A. Dalgarno, and J. M. Doyle, Phys. Rev. Lett. **106**, 053201 (2011).

[62] S. Hoekstra, M. Metsälä, P. C. Zieger, L. Scharfenberg, J. J. Gilijamse, G. Meijer, and S. Y. T. van de Meerakker, Phys. Rev. A **76**, 063408 (2007).

[63] S. Y. T. van de Meerakker, R. T. Jongma, H. L. Bethlem, and G. Meijer, Phys. Rev. A **64**, 041401 (2001).

[64] J. Riedel, S. Hoekstra, W. Jäger, J. J. Gilijamse, S. Y. T. van De Meerakker, and G. Meijer, Eur. Phys. J. D (2011).

[65] P. S. Żuchowski and J. M. Hutson, Phys. Chem. Chem. Phys. **13**, 3669 (2011).

[66] A. O. G. Wallis, E. J. J. Longdon, P. S. Żuchowski, and J. M. Hutson, Eur. Phys. J. D (2011).

[67] A. O. G. Wallis and J. M. Hutson, Phys. Rev. Lett. **103**, 183201 (2009).

[68] T. Helgaker, P. Jørgensen, and J. Olsen, *Molecular Electronic Structure Theory*, Wiley, Chichester, 2000.

[69] P. J. Knowles, C. Hampel, and H.-J. Werner, J. Chem. Phys. **99**, 5219 (1993).

[70] J. D. Watts, J. Gauss, and R. J. Bartlett, J. Chem. Phys. **98**, 8718 (1993).

[71] M. Heckert, O. Heun, J. Gauss, and P. G. Szalay, J. Chem. Phys. **124**, 124105 (2006).

[72] H.-J. Werner and P. J. Knowles, J. Chem. Phys. **82**, 5053 (1985).

[73] P. J. Knowles and H.-J. Werner, Chem. Phys. Lett. **115**, 259 (1985).

[74] H.-J. Werner and P. J. Knowles, J. Chem. Phys. **89**, 5803 (1988).

[75] P. J. Knowles and H.-J. Werner, Chem. Phys. Lett. **145**, 514 (1988).

[76] H.-J. Werner, Mol. Phys. **89**, 645 (1996).

[77] A. M. Arthurs and A. Dalgarno, Proc. R. Soc. London, Ser. A **256**, 540 (1960).

[78] G. C. Groenenboom and L. M. C. Janssen, Cold and ultracold collisions, in *Tutorials in molecular reaction dynamics*, edited by M. Brouard and C. Vallance, pages 392–441, RSC, Cambridge, 2010.

[79] B. R. Johnson, NRCC Proceedings **5**, 86 (1979).

[80] M. H. Alexander and D. E. Manolopoulos, J. Chem. Phys. **86**, 2044 (1987).

[81] F. Mrugała and D. Secrest, J. Chem. Phys. **78**, 5954 (1983).

[82] B. R. Johnson, J. Comput. Phys. **13**, 445 (1973).

[83] E. J. Rackham, T. Gonzalez-Lezana, and D. E. Manolopoulos, J. Chem. Phys. **119**, 12895 (2003).

[84] D. E. Manolopoulos, J. Chem. Phys. **85**, 6425 (1986).

[85] S. Gasiorowicz, *Quantum Physics*, Wiley, New York, 1974.

[86] R. V. Krems and A. Dalgarno, J. Chem. Phys. **120**, 2296 (2004).

[87] T. V. Tscherbul, Y. V. Suleimanov, V. Aquilanti, and R. V. Krems, New J. Phys. **11**, 055021 (2009).

[88] D. E. Manolopoulos, State-to-state reactive scattering, in *The Encyclopedia of Computational Chemistry*, edited by P. v. R. Schleyer, pages 2699–2708, Wiley, Chichester, 1998.

[89] M. Kajita, Phys. Rev. A **74**, 032710 (2006).

[90] G. S. F. Dhont, J. H. van Lenthe, G. C. Groenenboom, and A. van der Avoird, J. Chem. Phys. **123**, 184302 (2005).

[91] P. J. Knowles, C. Hampel, and H.-J. Werner, J. Chem. Phys. **112**, E3106 (2000).

[92] S. F. Boys and F. Bernardi, Mol. Phys. **19**, 553 (1970).

[93] T. H. Dunning, J. Chem. Phys. **90**, 1007 (1989).

[94] J. Stoer and R. Bulirsch, *Introduction to Numerical Analysis*, Springer-Verlag, New York, 1980.

[95] K. P. Huber and G. Herzberg, *Molecular Spectra and Molecular Structure. IV. Constants of Diatomic Molecules*, Van Nostrand Reinhold, New York, 1979.

[96] Molpro is a package of *ab initio* programs written by H.-J. Werner and P. J. Knowles, with contributions from R. D. Amos, A. Berning, D. L.Cooper, M. J. O. Deegan, A. J. Dobbyn, F. Eckert, C. Hampel, T. Leininger, R. Lindh, A. W. Lloyd, W. Meyer, M. E. Mura, A. Nicklaß, P.Palmieri, K. Peterson, R. Pitzer, P. Pulay, G. Rauhut, M. Schütz, H. Stoll, A. J. Stone and T. Thorsteinsson.

[97] A. J. Stone, *The Theory of Intermolecular Forces*, Oxford University Press, Oxford, 1996.

[98] C. Adamo and V. Barone, J. Chem. Phys. **110**, 6158 (1999).

[99] Dalton*, a molecular electronic structure program, Release 2.0*, 2005, http://www.kjemi.uio.no/software/dalton/dalton.html.

[100] D. J. Tozer and N. C. Handy, J. Chem. Phys. **109**, 10180 (1998).

[101] P. S. Żuchowski, R. Podeszwa, R. Moszyński, B. Jeziorski, and K. Szalewicz, J. Chem. Phys. **129**, 084101 (2008).

[102] A. J. Misquitta, R. Podeszwa, B. Jeziorski, and K. Szalewicz, J. Chem. Phys. **123**, 214103 (2005).

[103] P. S. Żuchowski, Chem. Phys. Lett. **450**, 203 (2008).

[104] R. Bukowski *et al.*, *SAPT2008: An Ab Initio Program for Many-Body Symmetry-Adapted Perturbation Theory Calculations of Intermolecular Interaction Energies*, University of Delaware and University of Warsaw, 2008.

[105] P. E. S. Wormer and H. Hettema, POLCOR package, Nijmegen, 1992.

[106] This g_4 option is, to our knowledge, not documented. The MOLPRO manual states that "*g_4 makes CASPT2 calculations size extensive for cases in which a molecule dissociates to high-spin open-shell (RHF) atoms*".

[107] A. van der Avoird, P. E. S. Wormer, F. Mulder, and R. M. Berns, Top. Curr. Chem. **93**, 1 (1980).

[108] A. N. Tikhonov and V. Y. Arsenin, *Solutions of Ill-Posed Problems*, Wiley, New York, 1977.

[109] T.-S. Ho and H. Rabitz, J. Chem. Phys. **104**, 2584 (1996).

[110] T.-S. Ho and H. Rabitz, J. Chem. Phys. **113**, 3960 (2000).

[111] A. V. Avdeenkov and J. L. Bohn, Phys. Rev. A **64**, 052703 (2001).

[112] J. Pérez-Ríos, M. Bartolomei, J. Campos-Martínez, M. I. Hernández, and R. Hernández-Lamoneda, J. Phys. Chem. A **113**, 14952 (2009).

[113] R. S. Ram and P. F. Bernath, J. Mol. Spectrosc. **260**, 115 (2010).

[114] M. Mizushima, *The Theory of Rotating Diatomic Molecules*, Wiley, New York, 1975.

[115] S. Green, J. Chem. Phys. **62**, 2271 (1975).

[116] J. M. Hutson and S. Green, MOLSCAT computer code, version 14 (1994), distributed by Collaborative Computational Project No. 6 of the Engineering and Physical Sciences Research Council (UK).

[117] M. L. González-Martínez and J. M. Hutson, Phys. Rev. A **75**, 022702 (2007).

[118] MATLAB, The MathWorks, Inc., http://www.mathworks.com.

[119] E. P. Wigner, Phys. Rev. **73**, 1002 (1948).

[120] R. V. Krems and A. Dalgarno, Phys. Rev. A **67**, 050704 (2003).

[121] J. M. Hutson, E. Tiesinga, and P. S. Julienne, Phys. Rev. A **78**, 052703 (2008).

[122] H. Cybulski, R. V. Krems, H. R. Sadeghpour, A. Dalgarno, J. Kłos, G. C. Groenenboom, A. van der Avoird, D. Zgid, and G. Chałasiński, J. Chem. Phys. **122**, 094307 (2005).

[123] A. Volpi and J. L. Bohn, Phys. Rev. A **65**, 052712 (2002).

[124] J. M. Gerton, C. A. Sackett, B. J. Frew, and R. G. Hulet, Phys. Rev. A **59**, 1514 (1999).

[125] T. V. Tscherbul, J. Kłos, A. Dalgarno, B. Zygelman, Z. Pavlovic, M. T. Hummon, H.-I. Lu, E. Tsikata, and J. M. Doyle, Phys. Rev. A **82**, 042718 (2010).

[126] S. Hensler, J. Werner, A. Griesmaier, P. O. Schmidt, A. Görlitz, T. Pfau, S. Giovanazzi, and K. Rzążewski, Appl. Phys. B **77**, 765 (2003).

[127] A. J. Moerdijk and B. J. Verhaar, Phys. Rev. A **53**, R19 (1996).
[128] A. V. Avdeenkov and J. L. Bohn, Phys. Rev. A **71**, 022706 (2005).
[129] B. Zygelman, Phys. Rev. A **81**, 032506 (2010).
[130] A. Messiah, *Quantum Mechanics*, North Holland, Amsterdam, 1969.
[131] M. Abramowitz and I. A. Stegun, *Handbook of Mathematical Functions*, National Bureau of Standards, Washington, D.C., 1964.
[132] S. Knoop, F. Ferlaino, M. Berninger, M. Mark, H.-C. Nägerl, R. Grimm, J. P. D'Incao, and B. D. Esry, Phys. Rev. Lett. **104**, 053201 (2010).
[133] D. J. Heinzen, R. Wynar, P. D. Drummond, and K. Kheruntsyan, Phys. Rev. Lett. **84**, 5029 (2000).
[134] Z. Idziaszek and P. S. Julienne, Phys. Rev. Lett. **104**, 113202 (2010).
[135] M. H. Alexander, E. J. Rackham, and D. E. Manolopoulos, J. Chem. Phys. **121**, 5221 (2004).
[136] G. F. Gribakin and V. V. Flambaum, Phys. Rev. A **48**, 546 (1993).
[137] Z. Idziaszek, G. Quéméner, J. L. Bohn, and P. S. Julienne, Phys. Rev. A **82**, 020703 (2010).

Summary

The theory of quantum mechanics states that atoms and molecules can behave both as particles and as waves. This wave-particle duality is usually observed only at very small length scales, on the order of a millionth of a millimeter, but certain quantum-mechanical effects also become apparent at the macroscopic level. Examples of the latter include superfluidity and superconductivity, phenomena whereby the viscosity of a fluid and the electrical resistance of a metal drop to zero, respectively. Another exotic quantum effect is Bose-Einstein condensation – the creation of a giant single matter-wave composed of many identical particles. Such macroscopic quantum phases typically only manifest themselves at extremely low temperatures. Superfluidity is associated with temperatures of a few degrees above absolute zero (0 K = −273.15 °C), while the formation of a Bose-Einstein condensate requires temperatures of even less than a microkelvin (0.000001 K). This makes Bose-Einstein condensates the coldest objects in the entire known universe.

When cooled to sub-kelvin temperatures, atoms and molecules also become very sensitive to (weak) electromagnetic radiation. This opens up the possibility to control and manipulate the behaviour of matter by means of external fields. For instance, one may tune the effective interparticle interaction, the dimensionality, and the amount of disorder in a system. Ultracold gases can therefore be used as "quantum simulators" of materials that are difficult to model theoretically. Other potential applications of ultracold systems include ultrahigh-precision atomic clocks and quantum information processing devices. Furthermore, at temperatures close to absolute zero, one may gain full control over chemical reactions – one of the holy grails in chemistry.

It is now well established that *atoms* can be efficiently cooled into the ultracold, sub-microkelvin regime by means of evaporative cooling. This process is essentially the same as that by which a cup of coffee cools down: the hottest particles evaporate into the air, leaving behind a slightly colder sample. In the case of cold and ultracold quantum gases, the role of the coffee cup is played by an external trapping potential, e.g. an electric or magnetic field. For *molecular* systems, which are expected to find even more applications than ultracold atoms, evaporative cooling is yet to be demonstrated experimentally. The success of this technique is critically dependent on the rate of thermalizing (elastic) collisions between the molecules in the trap. Non-elastic collisions will cause heating of the gas and trap loss, and are therefore unfavorable for the cooling process. In order to assess the feasibility of molecular evaporative cooling, theoretical knowledge of the cold and ultracold collision dynamics is required. Such information is also needed to evaluate the prospects for cold controlled chemistry and to describe the quantum many-body physics of, e.g., a molecular Bose-Einstein condensate.

In this thesis, we focus on the imidogen radical (NH), one of the most attractive candidates for cold-molecule experiments. NH has already been cooled and trapped in a magnetic field at a temperature of 0.5 K, and is expected to exhibit a rich chemistry even at ultralow temperatures. Our aim is to provide detailed theoretical insight into the collisional properties of NH + NH and to explore the possibilities for molecular evaporative cooling and magnetic field control of cold NH + NH reactions.

The quantum-mechanical concept of *spin* plays a crucial role in the cold and ultracold NH + NH dynamics. Spin is a magnetic property that is classically interpreted as the rotation of a particle around its own axis. The spin *direction* determines whether a molecule is attracted to or repelled from a magnet. Consequently, cold NH radicals can only be trapped if their spins are oriented in the right direction. This makes evaporative cooling of magnetically trapped NH a rather delicate task: the molecules must undergo many thermalizing collisions whilst maintaining their original spin orientation. Inelastic NH + NH collisions will change the spin state of at least one of the molecules, allowing particles to escape from the trap and hampering the cooling process. The same spin-state-changing processes can, however, also initiate a chemical reaction.

In order to study the above-mentioned NH + NH collision processes, we first require accurate potential energy surfaces. These can be thought of as “energy landscapes” on which the colliding molecules approach each other. Chapter 2 of this thesis is concerned with the calculation of the relevant potential energy surfaces for NH–NH, and the remaining chapters address the NH + NH collision dynamics on these potentials. All of the dynamics calculations have been performed using state-of-the-art quantum-mechanical scattering methods. The results of this work indicate that evaporative cooling of magnetically trapped NH is feasible, and that most of the thermalization is achieved through “head-on” elastic collisions. The main source of inelastic trap loss is a spin-dependent interaction that acts at long range, i.e., when the colliding molecules are still very far apart. More precisely, a magnetically trapped NH radical can change another molecule’s spin direction from a distance of a thousand times the particle size. This long-ranged collision process has been further investigated using an analytical scattering model, the results of which are in good agreement with numerical calculations. Our model is not only applicable to cold and ultracold NH radicals, but to any magnetically trapped species. Moreover, we have explored the cold chemical reaction dynamics of NH + NH by means of a novel quantum reactive scattering algorithm. We find that the spin-state-changing processes responsible for chemical reaction arise from an interaction that mainly acts at *short* range. Thus, reactive collisions between magnetically trapped NH molecules can occur only if the reactants approach each other to a very small distance. Such (ultra)cold reactions can proceed quite rapidly, however, which limits the efficiency of the thermalization process. The reaction probability is found to be only weakly dependent on the magnetic field strength, implying that external field control of cold NH + NH reactions will be rather difficult.

A more technical aspect of our work concerns the accuracy of the calculations. We find that the NH + NH collision cross sections – a measure for the probability of specific processes that may happen during the collision – are highly sensitive to the details of the potential energy surfaces. This is due to the presence of scattering resonances. Hence, in order to provide a realistic view of the dynamics, we must take into account the effects of (small) uncertainties in the NH–NH surfaces. By doing so, we can estimate the *likelihood* that e.g. molecular evaporative cooling will succeed, rather than providing an exact number for the collision cross sections. Closely related to this is the issue of basis set convergence. The numerical dynamics calculations have been performed in a scattering basis set whose size should be sufficiently large to ensure convergence of the cross sections. However, the *qualitative* results and conclusions of this thesis, which hold within the uncertainty limits of the potentials, are reasonably independent of basis set size. This implies that even an incompletely converged basis can provide meaningful insight into the dynamics. The latter finding is particularly relevant for molecular systems such as NH + NH, for which full basis set convergence is difficult to achieve.

The work described in this thesis constitutes one of the first quantum scattering studies on ultracold, magnetically trapped molecules. The results presented here may stimulate other theoretical efforts in the field of ultracold matter and encourage the development of novel experimental studies in the sub-(micro)kelvin regime.

Samenvatting

De quantummechanica is een natuurkundige theorie die stelt dat atomen en moleculen zich als deeltjes *en* als golven kunnen gedragen. Dit deeltjes-golf karakter wordt normaal gesproken pas zichtbaar op moleculair niveau, bij afstanden van minder dan een miljoenste millimeter, maar sommige quantummechanische effecten manifesteren zich ook op macroscopische schaal. Voorbeelden hiervan zijn supervloeibaarheid en supergeleiding, fenomenen waarbij de viscositeit van een vloeistof en de elektrische weerstand van een metaal compleet verdwijnen. Hierdoor kan een vloeistof of een elektrische stroom in principe eeuwig blijven doorstromen. Een ander exotisch quantumeffect is Bose-Einstein condensatie, een proces waarbij vele identieke deeltjes samen één gigantische materie-golf vormen. Dergelijke macroscopische quantumverschijnselen doen zich meestal pas voor bij extreem lage temperaturen. Supervloeibaarheid treedt op bij temperaturen van een paar graden boven het absolute nulpunt (0 K $= -273.15$ °C), en voor Bose-Einstein condensatie moet de temperatuur zelfs lager dan een microkelvin (0.000001 K) zijn. Dit maakt Bose-Einstein condensaten, voor zover bekend, de koudste objecten in het gehele universum.

Bij temperaturen rond het absolute nulpunt zijn atomen en moleculen ook bijzonder gevoelig voor (zwakke) elektromagnetische straling. Hierdoor wordt het mogelijk om het gedrag van deeltjes te controleren en te manipuleren met behulp van externe velden. Zo kan bijvoorbeeld de effectieve twee-deeltjes interactie, de periodiciteit, en de hoeveelheid wanorde in een systeem nauwkeurig worden getuned. Ultrakoude gassen worden daarom ook wel beschouwd als ideale “quantum-simulatoren”: processen die theoretisch moeilijk te modelleren zijn kunnen met ultrakoude deeltjes exact worden nagebootst en bestudeerd. Andere mogelijke toepassingen van ultrakoude gassen zijn ultra-nauwkeurige atoomklokken en quantumcomputers. Daarnaast kan men bij sub-(micro)kelvin temperaturen ultieme controle krijgen over chemische reacties – een van de heilige gralen van de chemie.

Om *atomen* af te koelen naar temperaturen van minder dan een microkelvin wordt vrijwel altijd gebruik gemaakt van verdamping. Dit koelproces heeft veel weg van de manier waarop een kopje koffie afkoelt: de warmste deeltjes verdampen in de lucht, waardoor er een koudere vloeistof achterblijft. In het geval van ultrakoude quantumgassen wordt de rol van het koffiekopje vervuld door een externe elektromagnetische val, bijvoorbeeld een elektrisch of magnetisch veld. Voor *moleculaire* gassen, die nog veel meer potentiële toepassingen hebben dan ultrakoude atomen, is afkoeling tot submicrokelvin temperaturen nog niet gerealiseerd. Of de verdampingsmethode hiervoor geschikt is hangt af van het botsingsgedrag van de moleculen. Efficiënte koeling is namelijk alleen mogelijk als de deeltjes in de val voldoende elastische (thermaliserende) botsingen ondergaan. Niet-elastische botsingen daarentegen zorgen voor opwarming van het gas en verlies van moleculen. Om meer grip te krijgen op het koelproces is het dus belangrijk om de botsingsdynamica van moleculaire gassen in kaart te brengen. Dergelijke kennis is ook nodig om bijvoorbeeld het gedrag van een moleculair Bose-Einstein condensaat te begrijpen, en om de mogelijkheden voor extern gecontroleerde (ultra)koude chemie te onderzoeken.

Dit proefschrift is gewijd aan NH, een moleculair radicaal dat inmiddels kan worden afgekoeld en opgesloten in een magnetische val bij een temperatuur van 0.5 K. Van alle moleculen die momenteel in aanmerking komen voor de verdampingsmethode is het een van de weinige systemen die ook tot interessante koude chemie kunnen leiden. Het doel van dit onderzoek is om theoretisch inzicht te verschaffen in het botsingsgedrag van (ultra)koude NH moleculen, en om vast te stellen of NH verder afgekoeld kan worden via moleculaire verdamping. Daarnaast willen we onderzoeken in hoeverre koude NH + NH reacties gecontroleerd kunnen worden met behulp van een magneetveld.

Het quantummechanische begrip “spin” speelt een belangrijke rol in de NH + NH botsingsdynamica. Spin is een magnetisch verschijnsel dat klassiek geïnterpreteerd wordt als de draaiing van een deeltje om zijn eigen as. De *richting* van de spin bepaalt of een molecuul aangetrokken of juist afgestoten wordt door een magneet. Om koude NH radicalen op te kunnen sluiten in een magnetische val is het dus noodzakelijk dat de moleculaire spins in de juiste richting wijzen. Dit maakt het verdampingsproces ook vrij gecompliceerd: de gevangen moleculen moeten veel elastische botsingen ondergaan om thermisch evenwicht te bereiken zonder dat daarbij hun spin-oriëntatie verandert. Door inelastische NH + NH botsingen kunnen de moleculen echter in een andere spintoestand terechtkomen en de val verlaten. Dergelijke spin-afhankelijke botsingen, die het koelproces bemoeilijken, kunnen ook tot chemische reacties leiden.

Een theoretische beschrijving van elastische, inelastische en reactieve botsingsprocessen vereist allereerst nauwkeurige potentiaaloppervlakken. Deze kunnen worden beschouwd als “energielandschappen” waarop de moleculen zich voortbewegen tijdens de botsing. In hoofdstuk 2 van dit proefschrift worden de relevante potentiaaloppervlakken voor NH–NH besproken, en in de overige hoofdstukken beschouwen we de NH + NH botsingsdynamica op deze potentialen. Alle berekeningen zijn uitgevoerd met state-of-the-art quantummechanische technieken. Uit de resultaten blijkt dat het in principe mogelijk is om NH verder af te koelen door middel van verdamping, en dat thermisch evenwicht het snelst wordt bereikt als de moleculen elkaar vol raken. De meeste inelastische processen worden veroorzaakt door een spin-afhankelijke interactie die vooral op grote afstand werkt, d.w.z. als de botsingspartners ver van elkaar verwijderd zijn. Hierdoor kan een magnetisch gevangen NH radicaal de spintoestand van een ander molecuul veranderen op een afstand die duizend keer zo groot is als de afmeting van een individueel molecuul. Dit mechanisme is verder onderzocht met een analytisch botsingsmodel waarvan de resultaten in goede overeenstemming zijn met numerieke berekeningen. Het model geldt niet alleen voor NH + NH, maar ook voor andere magnetisch gevangen deeltjes. Verder is de reactiedynamica van koude NH radicalen bestudeerd met behulp van een nieuw quantum-gebaseerd algoritme. Het blijkt dat chemische NH + NH reacties voornamelijk worden geïnduceerd door een spin-afhankelijke interactie die op korte afstand actief is. Dit betekent dat de reactanten elkaar eerst dicht moeten naderen om te kunnen reageren. Dergelijke chemische reacties kunnen het thermalisatieproces echter wel bemoeilijken. Verder is gevonden dat de reactiviteit van NH niet sterk afhangt van het magneetveld, wat de mogelijkheden voor extern gecontroleerde chemie beperkt.

Een meer technisch aspect van dit onderzoek betreft de nauwkeurigheid van de berekende resultaten. De NH + NH botsingsdoorsnedes – een maat voor de waarschijnlijkheid dat bepaalde processen optreden tijdens de botsing – blijken extreem gevoelig te zijn voor kleine verschillen in de potentiaaloppervlakken. Dit komt door de aanwezigheid van botsingsresonanties. Om een realistisch beeld te krijgen van de dynamica is het dus nodig om de (kleine) onzekerheid in de NH–NH potentialen in beschouwing te nemen. Het gevolg hiervan is dat we de exacte uitkomst van een experiment niet precies kunnen voorspellen, maar alleen de *kans* op een bepaald resultaat. Een gerelateerd onderwerp betreft de convergentie van de “kanaalbasis” die gebruikt is voor de dynamicaberekeningen. De dimensie van deze basis moet in principe groot genoeg zijn om tot nauwkeurige (geconvergeerde) botsingsdoorsnedes te komen. Het blijkt echter dat de *kwalitatieve* resultaten en conclusies, die gelden binnen de onzekerheidsmarge van de potentialen, vrijwel onafhankelijk zijn van de grootte van de basis. Dit impliceert dat ook een niet-volledig geconvergeerde basis gebruikt kan worden om meer inzicht te krijgen in de dynamica. Dit resultaat is met name relevant voor moleculaire systemen zoals NH + NH, waarvoor volledige convergentie moeilijk te realiseren is.

Het werk beschreven in dit proefschrift is een van de eerste quantummechanische onderzoeken naar het botsingsgedrag van ultrakoude, magnetisch gevangen moleculen. De verkregen resultaten kunnen helpen bij de analyse van andere theoretische studies en bij de ontwikkeling van nieuwe experimenten in het sub-(micro)kelvin regime.

Dankwoord

Op deze plaats wil ik een aantal mensen bedanken die op een of andere wijze betrokken zijn geweest bij de totstandkoming van dit proefschrift. Allereerst een groot woord van dank aan mijn promotor, Ad van der Avoird, en copromotor, Gerrit Groenenboom. Ad en Gerrit, ik heb de afgelopen jaren ontzettend veel van jullie geleerd en met veel plezier met jullie samengewerkt. Bedankt voor de geweldige begeleiding en de vrijheid die ik heb gekregen bij het uitvoeren van het onderzoek. Verder dank ik alle (oud-)medewerkers en studenten van de afdeling Theoretische Chemie voor de fijne werksfeer en samenwerking. In het bijzonder wil ik Koos Gubbels noemen, die met zijn enorme enthousiasme en kennis van de fysica een zeer prettige kamergenoot is gebleken. Koos, bedankt voor de vele interessante gesprekken en wetenschappelijke discussies.

I am very grateful to Prof. Jeremy Hutson for giving me the opportunity to work in his group at Durham University – an experience that proved to be pivotal in my PhD. Jeremy, I greatly enjoyed our scientific collaboration and I feel privileged to have worked with you and learned from you. Your vast expertise and keen eye for detail, as well as your kind hospitality, have made my stays in Durham fruitful and enjoyable. I also thank all other members of the Durham group for the pleasant atmosphere and interesting discussions. A special word of gratitude to Piotr Żuchowski, who has been a wonderful collaborator and friend for the past few years. Piotr, thank you for all your help and contributions to this thesis, as well as your hospitality during my visit to Toruń. I hope we will continue working together in the future.

I would like to thank Prof. Robert Moszyński for many stimulating conversations on both scientific and non-scientific matters, and for his generous hospitality during my stay in Warsaw. Also many thanks to the other members of the Warsaw group, in particular Wojciech Skomorowski and Michał Tomza, for making me feel so welcome. I am grateful to Hossein Sadeghpour, Timur Tscherbul, and all other scientists at ITAMP for their kind hospitality whenever I stayed in the US.

De afdeling C&CZ heeft een onmisbare bijdrage geleverd aan dit proefschrift door ieder computer-gerelateerd probleem, groot of klein, vrijwel onmiddellijk op te lossen. Heel veel dank aan Ben, Caspar, Ron, Wim, Peter en Bram voor hun inzet en altijd vriendelijke hulp. De experimentatoren van het Molecuulfysica lab, in het bijzonder

Wim van der Zande, Dave Parker en Bas van de Meerakker, dank ik voor hun betrokkenheid en interesse in mijn promotiewerk. Dave, ook hartelijk bedankt voor de laatste correcties van het manuscript.

Tijdens mijn promotietijd heb ik altijd kunnen rekenen op de nodige steun van vrienden, vriendinnen en familie. Ik bedank iedereen voor de fijne gesprekken, gezellige etentjes, feestjes, vakanties, en andere memorabele momenten die het promoveren een stuk aangenamer hebben gemaakt. My gratitude also extends to my non-Dutch-speaking friends, with whom I have shared many great times in Nijmegen and at international conferences and schools. Een speciaal woord van dank aan mijn ouders, die altijd voor me klaar staan en me onvoorwaardelijk steunen in alles.

Lieve Wim, zonder jou was dit proefschrift nooit geworden wat het nu is. Bedankt voor al je steun en vertrouwen, je vermogen me op te vrolijken als het tegenzit, je geduld en bovenal je liefde. Ik heb ontzettend veel zin in onze toekomst samen.

Publications

1. L. M. C. Janssen, A. van der Avoird, and G. C. Groenenboom, *Cold reactive scattering of NH radicals*, in preparation.

2. L. M. C. Janssen, A. van der Avoird, and G. C. Groenenboom, *On the role of the magnetic dipolar interaction in cold and ultracold collisions: Numerical and analytical results for NH($^3\Sigma^-$) + NH($^3\Sigma^-$)*, Eur. Phys. J. D **65**, 177 (2011).

3. L. M. C. Janssen, P. S. Żuchowski, A. van der Avoird, G. C. Groenenboom, and J. M. Hutson, *Cold and ultracold NH-NH collisions in magnetic fields*, Phys. Rev. A **83**, 022713 (2011).

4. L. M. C. Janssen, P. S. Żuchowski, A. van der Avoird, J. M. Hutson, and G. C. Groenenboom, *Cold and ultracold NH-NH collisions: The field-free case*, J. Chem. Phys. **134**, 124309 (2011).

5. G. C. Groenenboom and L. M. C. Janssen, *Cold and ultracold collisions*, in Tutorials in Molecular Reaction Dynamics, edited by M. Brouard and C. Vallance, p. 392-441 (RSC, Cambridge, 2010).

6. L. M. C. Janssen, G. C. Groenenboom, A. van der Avoird, P. S. Żuchowski, and R. Podeszwa, *Ab initio potential energy surfaces for NH($^3\Sigma^-$) – NH($^3\Sigma^-$) with analytical long range*, J. Chem. Phys. **131**, 224314 (2009).

7. A. V. Baklanov, L. M. C. Janssen, D. H. Parker, L. Poisson, B. Soep, J.-M. Mestdagh, and O. Gobert, *Direct mapping of recoil in the ion-pair dissociation of molecular oxygen by a femtosecond depletion method*, J. Chem. Phys. **129**, 214306 (2008).

8. D. Č. Radenović, A. J. A. van Roij, S.-M. Wu, J. J. ter Meulen, D. H. Parker, M. P. J. van der Loo, L. M. C. Janssen, and G. C. Groenenboom, *Photodissociation of vibrationally excited OH/OD radicals*, Mol. Phys. **106**, 557 (2008).

9. L. M. C. Janssen, M. P. J. van der Loo, G. C. Groenenboom, S.-M. Wu, D. Č. Radenović, A. J. A. van Roij, I. Anton Garcia, and D. H. Parker, *Photodissociation of vibrationally excited SH and SD radicals at 288 and 291 nm: The* $S(^1D_2)$ *channel*, J. Chem. Phys. **126**, 094304 (2007).

Curriculum Vitae

Name	Liesbeth Maria Catharina Janssen
Date of birth	December 28, 1983
Place of birth	Meijel, The Netherlands

2008 – 2012	PhD in Theoretical Chemistry, Institute for Molecules and Materials, Radboud University Nijmegen – Visiting student in the group of Prof. Jeremy M. Hutson, Durham University, UK
2005 – 2008	MSc in Chemistry, Radboud University Nijmegen (*summa cum laude*) – Major in Theoretical Chemistry (group of Prof. Ad van der Avoird and Dr. Gerrit C. Groenenboom), minor in Molecular and Laser Physics (group of Prof. David H. Parker) – Research topic: Photodissociation of diatomic radicals – Winner of the Unilever Research Prize 2007
2007	Six-month research project in the group of Prof. David C. Clary, University of Oxford, UK – Research topic: Reduced-dimensionality quantum dynamics of $OH + CH_4 \rightarrow H_2O + CH_3$ – Financially supported by a “HSP Talentenbeurs” of the Huygens Scholarship Programme
2002 – 2005	BSc in Chemistry, Radboud University Nijmegen (*cum laude*)